

INFORMATION TO USERS

This material was produced from a microfilm copy of the original document. While the most advanced technological means to photograph and reproduce this document have been used, the quality is heavily dependent upon the quality of the original submitted.

The following explanation of techniques is provided to help you understand markings or patterns which may appear on this reproduction.

1. The sign or "target" for pages apparently lacking from the document photographed is "Missing Page(s)". If it was possible to obtain the missing page(s) or section, they are spliced into the film along with adjacent pages. This may have necessitated cutting thru an image and duplicating adjacent pages to insure you complete continuity.
2. When an image on the film is obliterated with a large round black mark, it is an indication that the photographer suspected that the copy may have moved during exposure and thus cause a blurred image. You will find a good image of the page in the adjacent frame.
3. When a map, drawing or chart, etc., was part of the material being photographed the photographer followed a definite method in "sectioning" the material. It is customary to begin photoing at the upper left hand corner of a large sheet and to continue photoing from left to right in equal sections with a small overlap. If necessary, sectioning is continued again — beginning below the first row and continuing on until complete.
4. The majority of users indicate that the textual content is of greatest value, however, a somewhat higher quality reproduction could be made from "photographs" if essential to the understanding of the dissertation. Silver prints of "photographs" may be ordered at additional charge by writing the Order Department, giving the catalog number, title, author and specific pages you wish reproduced.
5. PLEASE NOTE: Some pages may have indistinct print. Filmed as received.

University Microfilms International

300 North Zeeb Road
Ann Arbor, Michigan 48106 USA
St. John's Road, Tyler's Green
High Wycombe, Bucks, England HP10 8HR

7818617

ALLEN, RICHARD GEORGE
AN INFRARED INVESTIGATION OF THE TEMPERATURE
STRUCTURE OF THE SOLAR ATMOSPHERE.

THE UNIVERSITY OF ARIZONA, PH.D., 1978

University
Microfilms
International

300 N. ZEEB ROAD, ANN ARBOR, MI 48106

AN INFRARED INVESTIGATION OF THE TEMPERATURE
STRUCTURE OF THE SOLAR ATMOSPHERE

by
Richard George Allen

A Dissertation Submitted to the Faculty of the
DEPARTMENT OF ASTRONOMY
In Partial Fulfillment of the Requirements
For the Degree of
DOCTOR OF PHILOSOPHY
In the Graduate College
THE UNIVERSITY OF ARIZONA

1 9 7 8

THE UNIVERSITY OF ARIZONA

GRADUATE COLLEGE

I hereby recommend that this dissertation prepared under my
direction by Richard George Allen
entitled AN INFRARED INVESTIGATION OF THE TEMPERATURE
STRUCTURE OF THE SOLAR ATMOSPHERE
be accepted as fulfilling the dissertation requirement for the
degree of Doctor of Philosophy

Rodger L. Thompson
Dissertation Director

May 19, 1978
Date

As members of the Final Examination Committee, we certify
that we have read this dissertation and agree that it may be
presented for final defense.

William F. Hoffmann
Roger Stahl
Norman F. Cybor
T. D. Swihart

May 19, 1978
May 19, 1978
19 May 78
May 25, 1978

Final approval and acceptance of this dissertation is contingent
on the candidate's adequate performance and defense thereof at the
final oral examination.

STATEMENT BY AUTHOR

This dissertation has been submitted in partial fulfillment of requirements for an advanced degree at The University of Arizona and is deposited in the University Library to be made available to borrowers under rules of the Library.

Brief quotations from this dissertation are allowable without special permission, provided that accurate acknowledgment of source is made. Requests for permission for extended quotation from or reproduction of this manuscript in whole or in part may be granted by the head of the major department or the Dean of the Graduate College when in his judgment the proposed use of the material is in the interests of scholarship. In all other instances, however, permission must be obtained from the author.

SIGNED: _____

Richard L. Allen

ACKNOWLEDGMENTS

I would like to thank the members of my committee for their encouragement and help in this endeavor. In particular, I would like to thank Don Hall for his advice and guidance during the observational phase of this research. I would also expecially like to thank Duane Carbon for the use of his model atmosphere program and for his encouragement in developing the solar models. I am also grateful to Barbara Fell and Larry Testerman for their help and assistance in processing the data.

TABLE OF CONTENTS

	Page
LIST OF TABLES	vi
LIST OF ILLUSTRATIONS	x
ABSTRACT	xii
 CHAPTER	
1. THE INTRODUCTION	1
2. THE OBSERVATIONS	6
2.1 Observational Wavelengths	7
2.2 Instrumental Techniques	9
2.3 Observing Days	14
3. THE DATA REDUCTIONS	18
3.1 Principles of the Data Reductions	19
3.2 Limb Darkening Reductions in REDUCER	22
3.3 Limb Darkening Reductions in DRIFT1	27
3.4 Limb Darkening Reductions in DRIFT2	31
3.5 Scattered Light Reductions	33
4. THE STATISTICAL TEST RESULTS	36
4.1 Statistical Results from DRIFT1	36
4.2 Statistical Results from DRIFT2	56
5. THE FINAL RESULTS OF THE OBSERVATIONS	63
5.1 Final Results of the Limb Darkening Observations	63
5.2 Corrections for Variations in the Solar Declination	83
5.3 Corrections for Computational Errors in Log μ	87
5.4 Corrections for Instrumental and Atmospheric Effects	94
5.5 Corrections for Nonlinearities in the Instrumentation	122

TABLE OF CONTENTS--Continued

	Page
6. THE SOLAR ABSOLUTE INTENSITY OBSERVATIONS . . .	126
6.1 Principles of the Solar Absolute Intensity Observations	126
6.2 Absolute Intensity Observations of Labs and Neckel	129
6.3 Absolute Intensity Observations of Saiedy and Goody	136
6.4 Absolute Intensity Observations of Houtgast	138
7. THE SOLAR MODELS	142
7.1 Description of the Model Atmosphere Computations	143
7.2 Limb Darkening Observations of Pierce and Slaughter	148
7.3 Procedure for Testing the Solar Models . .	149
7.4 One-Component Models of the Solar Atmosphere	152
7.5 Two-Component Models of the Solar Atmosphere	172
7.6 Conclusions	198
REFERENCES	201

LIST OF TABLES

Table		Page
2.1	The observational wavelengths	8
2.2	The observing days	15
3.1	Reducer commands	24
4.1	Statistical test results from DRIFT1: sign of DELTA for limb darkening measures . .	39
4.2	Statistical test results from DRIFT1: sign of DELTA for scattered light measures	48
4.3	Statistical test results from DRIFT2: sign of DELTAP for limb darkening measures	57
5.1	Limb darkening results for 10840.10 Å	64
5.2	Limb darkening results for 10854.00 Å	65
5.3	Limb darkening results for 10865.00 Å	66
5.4	Limb darkening results for 12466.63 Å	67
5.5	Limb darkening results for 12505.51 Å	68
5.6	Limb darkening results for 16222.00 Å	69
5.7	Limb darkening results for 16513.18 Å	70
5.8	Limb darkening results for 21855.59 Å	71
5.9	Limb darkening results for 21907.47 Å	72
5.10	Limb darkening results for 23121.03 Å	73
5.11	Limb darkening results for 23127.19 Å	74
5.12	Limb darkening results for 23132.73 Å	75
5.13	Limb darkening results for 38839.36 Å	76

LIST OF TABLES--Continued

Table		Page
5.14	Limb darkening results for 38862.02 Å	77
5.15	Limb darkening results for 45908.50 Å	78
5.16	Limb darkening results for 46142.57 Å	79
5.17	Limb darkening results for 85636.32 Å	80
5.18	Limb darkening results for 104007.55 Å	81
5.19	Coefficients for the least-squares quadratic fits to the limb darkening measures	84
5.20	True values of log μ for a drift scan through disk center (RSOLAR = 1599.5)	91
5.21	True values of log μ for a drift scan with an offset of 2.5 mm (RSOLAR = 1599.5)	93
5.22	Theoretical limb darkening errors for a 2" seeing disk	98
5.23	Scattered light results for 10840.10 Å	100
5.24	Scattered light results for 10854.00 Å	101
5.25	Scattered light results for 10865.00 Å	102
5.26	Scattered light results for 12466.63 Å	103
5.27	Scattered light results for 12505.51 Å	104
5.28	Scattered light results for 16222.00 Å	105
5.29	Scattered light results for 16513.18 Å	106
5.30	Scattered light results for 21855.59 Å	107
5.31	Scattered light results for 21907.47 Å	108
5.32	Scattered light results for 23121.03 Å	109
5.33	Scattered light results for 23127.19 Å	110

LIST OF TABLES--Continued

Table		Page
5.34	Scattered light results for 23132.73 Å	111
5.35	Scattered light results for 38839.36 Å	112
5.36	Scattered light results for 38862.02 Å	113
5.37	Scattered light results for 45908.50 Å	114
5.38	Scattered light results for 46142.57 Å	115
5.39	Scattered light results for 85636.32 Å	116
5.40	Scattered light results for 104007.55 Å	117
5.41	Fitted limb darkening minus observed limb darkening at $\log \mu = -0.95$ and the scattered light 6" from the limb	120
5.42	Results of the detector linearity test	124
6.1	Physical constants for the absolute intensity measures of Labs and Neckel	132
6.2	Absolute solar intensities for the passbands used by Labs and Neckel	134
6.3	Absolute intensity measures of Saiedy and Goody	138
7.1	Elemental abundances by number in the model atmosphere program	145
7.2	References for the opacity representations in the model atmosphere program	146
7.3	Physical parameters of the HSRA	153
7.4	Residuals for the HSRA	155
7.5	Physical parameters of Model 1	158
7.6	Residuals for Model 1	161
7.7	Physical parameters of Model 1a	164
7.8	Residuals for Model 1a	166

LIST OF TABLES--Continued

Table		Page
7.9	Ratios of the predicted absolute intensity at disk center to the observed absolute intensity at disk center for the one- component solar models	167
7.10	Monochromatic optical depths for Model 1 . . .	168
7.11	Physical parameters of the hot component of Model 2	176
7.12	Physical parameters of the cool component of Model 2	178
7.13	Residuals for Model 2	181
7.14	Physical parameters of the hot component of Model 2a	184
7.15	Physical parameters of the cool component of Model 2a	186
7.16	Residuals for Model 2a	188
7.17	Ratios of the predicted absolute intensity at disk center to the observed absolute intensity at disk center for the two- component solar models	189
7.18	Normalized physical depths for the hot and cool components of Model 2	196

LIST OF ILLUSTRATIONS

Figure		Page
2.1	Diagram of the West Auxiliary and the Infrared Spectrometer	10
4.1	Values of DELTA for limb darkening measures at 16513.18 Å on February 25, 1974	44
4.2	Values of DELTA for limb darkening measures at 45908.50 Å on May 21, 1974 . . .	45
4.3	Values of DELTA for limb darkening measures at 45908.50 Å on May 25, 1974 . . .	46
4.4	Values of DELTA for limb darkening measures at 85636.32 Å on May 25, 1974 . . .	47
4.5	Values of DELTA for scattered light measures at 10840.10 Å on February 1, 1974	51
4.6	Values of DELTA for scattered light measures at 10854.00 Å on February 1, 1974	52
4.7	Values of DELTA for scattered light measures at 10854.00 Å on February 2, 1974	53
4.8	Values of DELTA for scattered light measures at 23127.73 Å on April 29, 1974 . .	54
4.9	Values of DELTA for scattered light measures at 38839.36 Å on May 14, 1974 . . .	55
4.10	Values of DELTAP for limb darkening measures at 16513.18 Å on April 20, 1974 . .	61
4.11	Values of DELTAP for limb darkening measures at 85636.32 Å on May 25, 1974 . . .	62
5.1	Diagram of the coordinate systems used in computing the effect of the solar declination on the path of a drift scan across the sun	85

LIST OF ILLUSTRATIONS--Continued

Figure		Page
5.2	Diagram of the geometry used in calculating the limb darkening measures in OPTION	88
5.3	Diagram of the geometry used in calculating the true value of $\log \mu$ for each value of XLOGMU	90
5.4	Observed measures of the scattered light 20" from the limb	121
5.5	Per cent deviation from the average response for the InSb dectector	125
7.1	Solar models: (a) Model 1, —; (b) HSRA, ---	157
7.2	Solar models: (a) Model 1, —; (b) Model 1a, ---; (c) HSRA, -.-	163
7.3	Solar models: (a) Model 2, —; (b) Model 1, ---	175
7.4	Solar models: (a) Model 2, —; (b) Model 2a, ---	183
7.5	Solar models: (a) Model 2, —; (b) Margrave and Swihart (1969), ---; (c) Ulrich (1970), -.-; (d) Nordlund (1976), -.-	195

ABSTRACT

Narrow-band continuum limb darkening observations of the sun were taken with the Infrared Spectrometer and the West Auxiliary of the McMath Solar Telescope during the first half of 1974. These observations were made at eighteen wavelengths between 10840.10 and 104007.55 Å. A daily set of observations at any one of the observational wavelengths consisted of twelve drift scans across the solar disk. These drift scans were taken by stopping the heliostat of the West Auxiliary and allowing the image of the sun to drift across the entrance aperture of the Infrared Spectrometer. Limb darkening measures from the individual drift scans in each set of observations were averaged together during the data reductions in order to reduce the effects of local variations in the solar atmosphere on the day of observation. Longer-term changes in the limb darkening were averaged out by taking observations on several different days at each wavelength. Statistical tests in the data reductions checked the agreement between the west and east limbs of the sun and the significance of day-to-day variations in the limb darkening. Systematic errors due to scattered light, instrumental diffraction, and the finite size of the entrance aperture of the spectrometer were found to be negligible between disk center and

$\log \mu = -0.70$. The high spectral resolution of the Infrared Spectrometer made it unnecessary to compensate for unresolved spectral lines. The effects of scattered light were reduced by observing in the infrared.

The infrared limb darkening measures were used with a few absolute intensity and limb darkening measures of other investigators to develop a series of empirical solar models. Several of the absolute intensity measures were corrected for line blanketing or for changes in the absolute temperature scale before they were used in calibrating the models. The temperatures in most of the solar models were adjusted until the predictions of the model atmosphere program matched the observational measures as well as possible. Limb darkening residuals were calculated by subtracting the observational measures of the limb darkening from the limb darkening measures that were computed from the program. Each positive residual indicated that the model limb darkening was too high; while each negative residual indicated that the model limb darkening was too low. Experiments with several models indicated that a steep temperature gradient was needed to fit the observations at short wavelengths while a rather low temperature gradient was needed at long wavelengths. Non-LTE effects and errors in the H^- opacity were ruled out as possible sources of this discrepancy.

An excellent fit to the observations was ultimately achieved with a two-component LTE solar model. The hot component of this model represents the half of the solar surface that is above the median temperature at each depth; while the cool component represents the half of the solar surface that is below the median temperature. Most of the observations are fitted to within the expected errors by this model. Discrepancies below 4500 \AA are probably due to line blanketing. The splitting between the hot and cool components of the model is consistent with current estimates of the rms intensity fluctuations in the solar atmosphere. The model also resembles several theoretical two-component models that have recently appeared in the literature.

CHAPTER 1

THE INTRODUCTION

The establishment of a well-defined and accurate model of the temperature structure of the solar atmosphere is of great importance in solar physics because nearly all observable phenomena are dependent on the physical conditions in the outermost layers of the sun. In recent years it has become clear that a generally accepted model of the solar photosphere would be of great value in the reduction and interpretation of diverse types of solar and stellar data. An early attempt at such a model was the Utrecht Reference Model of the Photosphere and Low Chromosphere (URP) by Heintze, Hubenet, and de Jager (1964). The Bilderberg Conference in 1967 then recommended the general adoption of a model which became known as the Bilderberg Continuum Atmosphere (BCA). This model was later replaced by the Harvard-Smithsonian Reference Atmosphere (HSRA) by Gingerich et al. (1971). All of these models were based on observational measures of the solar limb darkening and the absolute solar intensity at disk center. None of them is entirely satisfactory over anything but a very limited range of wavelengths.

In order to determine the run of temperature versus optical depth from a solar model, one has to be able to observe the emergent radiation from many levels of the solar atmosphere. In principle, this can be accomplished by measuring disk-center absolute intensities over an extended range of wavelengths. Variations in the solar opacity then allow one to look to different physical depths in the atmosphere. Measures of the center-to-limb variation of the absolute intensity can also be used to probe the solar atmosphere. This technique takes advantage of the fact that one sees to different effective depths by looking at various angles to the surface. Absolute intensities are difficult to calibrate, however, and systematic errors in a number of spectral regions are almost unavoidable. For this reason, it is often more convenient to use solar limb darkening measures to define the temperatures in the atmosphere. Limb darkening observations can be made accurately and easily because the solar intensity at each point on the disk is normalized to the intensity at disk center rather than to an absolute standard. A model that is based on a large number of limb darkening measures can be calibrated with only a few measures of the absolute intensity.

Solar limb darkening measures were used to study the temperature structure of the solar atmosphere in this research. In the past, many models of the solar atmosphere were based on the limb darkening measures of Pierce (1954)

or on the corrected measures of David and Elste (1962). Corrections for scattered light and for the frequency response of the detector limited the accuracy of these limb darkening measures to $\pm 1\%$. Modern photoelectric techniques have made it possible to reduce this uncertainty. Improvements in infrared detectors have also made it possible to extend the observations farther into the infrared.

The West Auxiliary of the McMath Solar Telescope and the Infrared Spectrometer at Kitt Peak were used to obtain narrow-band continuum drift scans at selected wavelengths between 10840.10 and 104007.55 Å in this research. These drift scans were taken by stopping the heliostat of the West Auxiliary and allowing the rotation of the earth to move the image of the sun across the entrance aperture of the Infrared Spectrometer while the output of a detector at the exit slit was sampled by a computer. Because the atmospheric and instrumental paths remained constant, each scan was taken in a highly uniform manner.

The infrared limb darkening observations were taken over as large a wavelength range as possible on either side of the H^- opacity minimum at 16400 Å. High resolution spectra were used to identify specific wavelengths that were particularly free of solar and telluric absorption lines. At some wavelengths, however, a small amount of terrestrial absorption was unavoidable. Opacity sources in the visible vary slowly as a function of wavelength and provide little

leverage in probing the atmosphere. The situation is better in the infrared where the opacity sources in the atmosphere increase rapidly on both sides of the minimum at 16400 \AA .

In nearly all limb darkening investigations there are corrections which have to be made in order to properly interpret the data. When the entrance aperture of the spectrometer is large compared to the scale over which the intensity changes near the limb, for example, the instrumental limb darkening will only approximately give the true intensity distribution across the solar disk. Similar effects can also be caused by scattered light, poor seeing conditions, and the frequency response of the detector. The need for such corrections has been minimized in the present research by the large image scale of the West Auxiliary and the use of improved detectors. The high spectral resolution that was available with the Infrared Spectrometer also eliminated the necessity of compensating for unresolved spectral lines in the instrumental bandpass. The deleterious effects of scattered light were significantly reduced by observing in the infrared.

The infrared limb darkening measures were used with the absolute intensity and limb darkening measures of several other investigators to develop a series of empirical solar models. The absolute intensity measures defined the temperatures at only a few depths in each model. The temperatures at other levels in the models were deduced

from the measures of the solar limb darkening. Solar models with one and two temperature components in the atmosphere were considered in this research. The best fit to the observations was obtained with a two-component LTE model. Standard one-component models were found to be less satisfactory.

The infrared limb darkening observations that were taken in this research are described in Chapter 2. The reduction of the raw data is then discussed in Chapter 3. Chapter 4 contains the results of the statistical tests that were performed on the data. The final limb darkening measures at each observational wavelength are presented in Chapter 5. This chapter also contains a discussion of the observational errors. Chapter 6 contains a discussion of the absolute intensity measures that were used in calibrating the solar models. The solar models are presented and discussed in Chapter 7. The basic conclusions that can be drawn from this research are also presented in this chapter.

CHAPTER 2

THE OBSERVATIONS

A series of narrow-band continuum limb darkening observations were taken with the Infrared Spectrometer and the West Auxiliary of the McMath Solar Telescope in this research. These observations were made at eighteen wavelengths between 10840.10 and 104007.55 Å in the infrared. A daily set of observations at any one of these wavelengths consisted of twelve parallel drift scans across the solar disk. These drift scans were taken by locking the heliostat of the telescope and allowing the rotation of the earth to drift the image of the sun across the entrance aperture of the spectrometer while the output of a detector at the exit slit was sampled by a computer. Limb darkening measures from the individual drift scans in each daily set were then averaged together during the data reductions in order to reduce the effects of local variations in the solar atmosphere on the day of observation. Longer-term changes in the limb darkening were averaged out by taking observations on several different days at each wavelength. Useful observations were obtained on twenty-four days between January 31, 1974, and May 26, 1974.

The observational wavelengths are presented and discussed in Section 2.1. The drift scans are described in Section 2.2. A discussion of the observing days is provided in Section 3.3.

2.1 Observational Wavelengths

Narrow-band continuum drift scans were taken at eighteen wavelengths in the infrared in this research. Two observational wavelengths were initially chosen to coincide with the H^- opacity minimum at 16400 \AA . Other observational wavelengths were then selected over as large a wavelength range as possible in order to take full advantage of the opacity variations on either side of the minimum. Two or more wavelengths were chosen fairly close together in each region of the spectrum. This procedure was followed so that the final limb darkening measures at each wavelength could be compared to others that were taken in the same region of the spectrum. Since the limb darkening measures from these observations were to be used in deriving continuum solar models, care was taken to see that all of the observational wavelengths were free of solar absorption lines.

Each observational wavelength was referenced to the position of a suitable absorption line in the solar spectrum. The continuum wavelength was therefore highly reproducible from day to day. The final observational wavelengths are

listed in Table 2.1. Positions for the reference lines are also included in this table.

Table 2.1. The observational wavelengths.

Observational position				Reference position	
λ (Å)	$\tilde{\nu}$ (cm ⁻¹)	Order	Bandpass (Å)	$\tilde{\nu}$ (cm ⁻¹)	Line
10840.10	9222.484	10	.35	9207.863	H ₂ O ⊕
10854.00	9210.670	10	.35	9207.863	H ₂ O ⊕
10865.00	9201.350	10	.35	9207.863	H ₂ O ⊕
12466.63	8019.220	9	.37	7983.700	K ⊙
12505.51	7994.288	9	.37	7983.700	K ⊙
16222.00	6162.785	7	.48	6165.180	Si ⊙
16513.18	6054.114	7	.47	6052.620	Fe ⊙
21855.59	4574.240	5	.69	4565.510	Ti ⊙
21907.47	4563.407	5	.69	4565.510	Ti ⊙
23121.03	4323.886	5	.66	4322.060	CO ⊙
23127.19	4322.735	5	.66	4322.060	CO ⊙
23132.73	4321.700	5	.65	4322.060	CO ⊙
38839.36	2574.005	3	1.08	2572.865	N ₂ O ⊕
38862.02	2572.505	3	1.08	2572.865	N ₂ O ⊕
45908.50	2177.652	2	2.60	2178.588	CO ?
46142.57	2166.617	2	2.59	2166.936	CO ?
85636.32	1167.410	1	17.20	1165.922	H ₂ O ⊕
104007.55	961.206	1	15.61	945.980	CO ₂ ⊕

2.2 Instrumental Techniques

The limb darkening observations in this research were taken with the Infrared Spectrometer and the West Auxiliary of the McMath Solar Telescope. The optical path through the telescope and spectrometer is diagrammed in Figure 2.1. The heliostat of the West Auxiliary directs light from the sun to a 91-cm parabolic primary mirror. The reflected light from the primary is then sent to the Infrared Spectrometer with two large optical flats. The beam of light that falls on the primary is restricted to 81.3 cm by a circular aperture stop in the mounting of the heliostat. The 35.4-m focal length of the primary provides an image scale of 5.824"/mm. The solar image is approximately 33 cm in diameter.

The Infrared Spectrometer is a horizontal Czerny-Turner. The camera and collimator mirrors of the spectrometer are both 40.6 cm in diameter and have a 20.5-m focal length. The angle of the grating is controlled by a stepper motor that is attached to the outside of the spectrometer. A single motor step rotates the grating through $1/216000$ radian. The spectrometer detector is mounted at the focus of the camera mirror. The output of the detector is amplified and sent through a 200-Hz low-pass filter. The filtered signal is then sampled by a 13-bit a/d converter that is operated by a Sigma II computer. During drift scans the detector output is repeatedly sampled at 1000 Hz for a

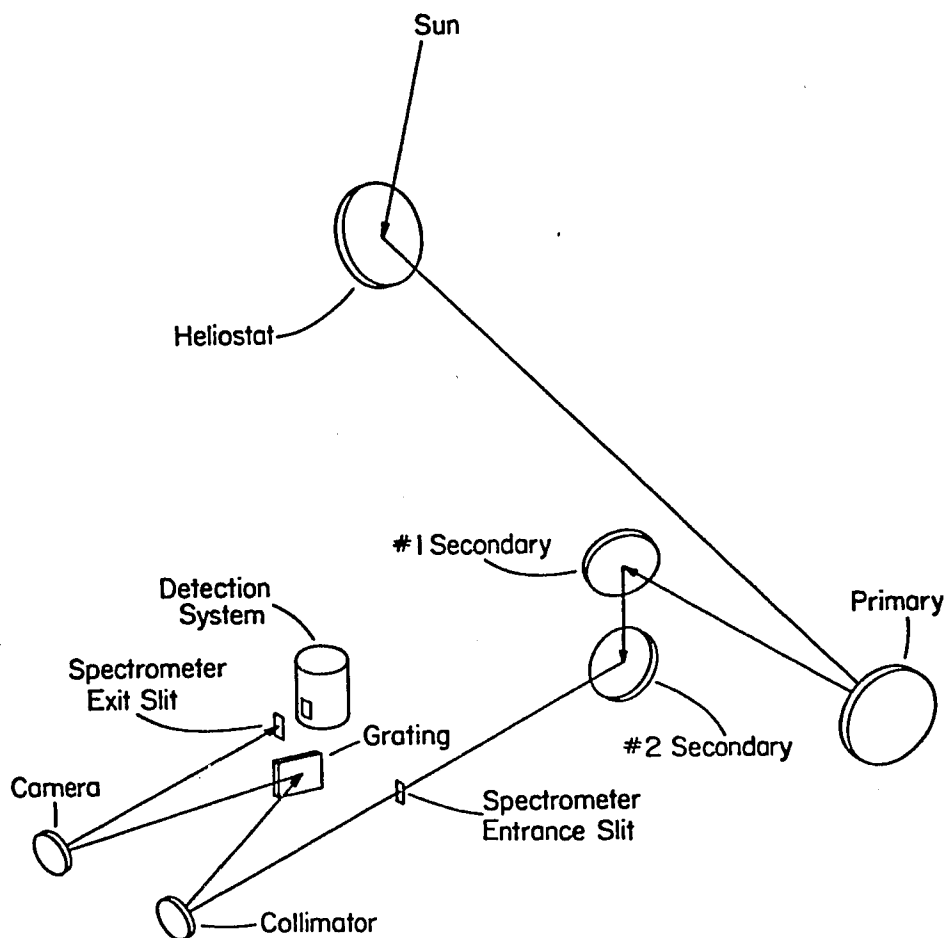


Figure 2.1. Diagram of the West Auxiliary and the Infrared Spectrometer.

time interval that has been selected by the operator. Average values of the detector output over the time intervals are recorded as individual data points in the computer. The sampling is continued until 4096 points have been recorded. A 40 ms time interval was used for all of the drift scans in this research.

A daily set of observations at any one of the observational wavelengths consisted of twelve drift scans across the sun. These drift scans were taken by locking the heliostat and allowing the rotation of the earth to move the image of the sun across the entrance aperture of the spectrometer. Since the image of the sun travelled along a line of constant declination during each drift scan, geocentric coordinates can be used to describe the observations.

The image of the sun was centered on the entrance aperture of the Infrared Spectrometer at the beginning of each set of observations. Limb guiders on a metal disk in front of the entrance aperture of the spectrometer were arranged so that one controlled the north-south position of the image while the other controlled the east-west position. The heliostat of the West Auxiliary was then slewed to the west with the guiders off before the first drift scan. The heliostat drive was stopped, and data sampling was initiated as the leading edge of the sun passed over a pre-selected point on the metal disk. A second scan was taken after the image of the sun was offset 0.5 mm to the south

with the micrometer mount of the north-south guider. This offsetting was repeated until a total of six drift scans was obtained from disk center to 2.5 mm north of disk center on the solar image. Six additional scans were then taken from disk center to 2.5 mm south of disk center. All of the drift scans passed within 15" of the center of the sun.

A 0.586 mm circular entrance aperture was used in the spectrometer at all wavelengths except 85636.32 and 104007.55 Å. A 2.515 mm entrance aperture was used at 85636.32 and 104007.55 Å. The 0.586 mm entrance aperture covered 3.4" on the sun; while the 2.515 mm entrance aperture covered 14.6" on the sun. A circular entrance aperture was used in the spectrometer so that the changing orientation of the drift direction throughout the day would have no effect on the profile of the sun.

A silicon diode detector was used with a prism postdisperser from 10840.10 to 10865.00 Å. The 0.560 mm entrance slit of the postdisperser served as the exit slit of the spectrometer; while a second slit in the mounting of the diode blocked any light from the postdisperser that was not in the desired grating order. Because the order separation of the postdisperser was marginal at such short wavelengths, an additional narrow-band filter was used with the silicon diode in order to completely eliminate overlapping spectral orders.

An InSb detector was used with the postdisperser from 12466.63 to 38862.02 Å. The InSb detector was cooled with liquid nitrogen. Filters inside the dewar also reduced the thermal background. The InSb detector was used with just a narrow-band filter inside the dewar at 45908.50 and 46142.57 Å. A 1.0 mm slit inside the dewar acted as the exit slit of the spectrometer.

The observations at 85636.32 and 104007.55 Å were made with an arsenic-doped silicon detector that was operated in a photoconductive mode. The detector was cooled with liquid helium, and a broad-band filter was used to reduce the background radiation that entered through the 2.5 mm circular entrance aperture of the dewar. The signal-to-noise ratio was further increased by using the detector with a lock-in amplifier and a 400-Hz chopper in front of the entrance aperture of the spectrometer. The output of the lock-in amplifier was filtered and sampled in the usual manner.

The infrared diffraction grating was used in single pass for all of the limb darkening observations. This grating is ruled at 121.5 l/mm and is blazed at 114000 Å in first order. The grating has a 35 x 45 cm ruled surface. The intrinsic resolution of the grating in 7th order is over 350000. The spectral bandpass at each wavelength in this research, however, depended primarily on the width of the entrance and exit apertures of the spectrometer. An upper

limit on the instrumental bandpass at each wavelength can be calculated from the formula

$$\Delta\lambda = \left[\frac{64.5}{m^2} - 2.38 \times 10^{-9} \cdot \lambda^2 \right]^{1/2} \cdot \bar{w}$$

in which λ is the wavelength in angstroms, m is the grating order, and \bar{w} is the average width in millimeters of the entrance and exit apertures of the spectrometer. Instrumental bandpasses based on this formula were included in Table 2.1.

2.3 Observing Days

The infrared limb darkening observations were taken on twenty-four days during the first half of 1974. A list of the observing days is provided in Table 2.2. The solar declinations that are listed in this table were computed from the American Ephemeris and Nautical Almanac. Values are for 12:00 noon Mountain Standard Time. The observational measures of the solar radius were calculated from the drift scans that were taken each day. Each measure is normalized to 1. A.U. The daily measures of the solar radius have an average value of 959.7" and a standard deviation of 0.6". Wittman (1977) has recently suggested a value of 960.00 ± 0.09 " for the angular radius of the sun. The observational measures in Table 2.2 are in good agreement with this value of the solar radius.

Table 2.2. The observing days.

Date	Solar declination	Observed solar radius
1/31/74	-17°19.5'	959.4"
2/01/74	-17°02.5'	959.3"
2/02/74	-16°45.3'	959.3"
2/15/74	-12°36.6'	959.3"
2/16/74	-12°15.8'	958.9"
2/24/74	-9°23.3'	959.3"
2/25/74	-9°01.0'	959.6"
2/26/74	-8°38.6'	959.1"
3/16/74	-1°40.0'	959.4"
3/17/74	-1°16.2'	959.5"
4/20/74	+11°35.0'	959.4"
4/21/74	+11°55.4'	959.3"
4/22/74	+12°15.7'	959.3"
4/28/74	+14°12.7'	959.7"
4/29/74	+14°31.4'	959.4"
4/30/74	+14°49.9'	959.2"
5/12/74	+18°10.9'	960.0"
5/14/74	+18°40.4'	960.1"
5/15/74	+18°54.7'	959.9"
5/20/74	+20°01.1'	960.9"
5/21/74	+20°13.4'	960.3"
5/24/74	+20°48.2'	960.2"
5/25/74	+20°59.0'	960.5"
5/26/74	+21°09.5'	961.2"

Cumulus clouds frequently developed late in the morning over the mountain. On several days useful observations were taken for a couple of hours before the sun was finally obscured by clouds. Cirrus clouds also occasionally caused the partial or complete loss of an observing day. As these clouds drifted over the mountain from the southwest, short periods of clear sky would alternate with longer periods of cloudiness on a time scale that was frequently somewhat less than the one hour that was required to complete a daily set of observations.

The existence of thin clouds of any type within 30° of the sun was considered to be serious enough to halt the observations. The particular set that was interrupted would then be restarted from the beginning unless the sky conditions improved within about ten minutes. The sky conditions were checked before and after every drift scan on days when clouds were likely to interfere with the observations. On better days the sky was checked only once or twice during each set of observations.

Winds of over 20 knots interfered with the observations on some days because the unshielded heliostat would vibrate whenever both it and the mirror cover doors attached to it were buffeted by strong winds. The effects of this wind shake were most noticeable in the drift scans whenever a gust of wind struck the heliostat just as the image of the limb was passing over the circular entrance aperture of the

spectrometer. The resulting image motion would then appear as a spike or other discontinuity in the profile of the sun at the extreme limb. Most of the scans with anomalous limb profiles were simply repeated during the course of the observations. A few scans with very small inflections at the limb were also picked up in the first stage of the data reductions.

The seeing conditions tended to be good in the morning and poor in the afternoon. The seeing conditions varied from 1 to 3" on a typical day. Although rather poor seeing washed out the spatial structure in each scan, it had virtually no systematic effect on the limb darkening except at the extreme edge of the solar disk. The spatial details of the individual drift scans were eventually eliminated, anyway, when the limb darkening measures from many different scans were averaged together in the data reductions.

CHAPTER 3

THE DATA REDUCTIONS

The limb darkening observations were processed on the CDC 6400 computer at the Kitt Peak National Observatory. The reductions were performed in several stages. In the first stage of the reductions each drift scan was processed with a spectroscopy program named REDUCER. This program was used with a special subroutine that calculated observational measures of the limb darkening at forty positions across the solar disk. The variable μ was defined as the cosine of the angle between the normal to the solar surface and the line of sight to the earth throughout the reductions. The limb darkening measures in each scan were computed at regular intervals in $\log \mu$ since there was almost a linear relationship between $\log \mu$ and the value of the limb darkening at most wavelengths.

The limb darkening measures from the separate scans in each daily set were averaged together in a program named DRIFT1. A Student's test in DRIFT1 checked the statistical agreement between the west and east limbs of the sun. The limb darkening measures from all of the daily sets at each wavelength were then averaged together in a program named DRIFT2. A Student's test in DRIFT2 checked the

statistical significance of day-to-day variations in the limb darkening measures. A reduction sequence that was very similar to this one was also used to compute a series of scattered light measures off the limb of the sun.

The general philosophy of the data reductions is discussed in Section 3.1. The specific reductions that were carried out with REDUCER are then presented in Section 3.2. The computations in DRIFT1 and DRIFT2 are discussed in Sections 3.3 and 3.4. A discussion of the scattered light reductions is given in Section 3.5.

3.1 Principles of the Data Reductions

The instrumental response at each point I in every drift scan can be expressed as

$$R(I) = gF(I) + Z(I)$$

where $F(I)$ is the radiant flux at the detector, g is the instrumental gain, and $Z(I)$ is an independent term that must be added to the flux-produced signal in order to account for residual offsets in the instrumental zero. The gain g includes factors such as the quantum efficiency of the detector, the electronic amplification of the detector signal, and the renormalization of the data that occurs in the conversion of the analog signal into its digital form on the raw data tapes written by the Sigma II. The radiant flux depends on the intrinsic intensity of the solar disk, the transmission properties of the atmosphere, the

efficiency of the telescope and spectrometer, and the thermal emissivity of the sky, mirrors, and other surfaces that are visible to the detector.

A portion of the radiant flux at the detector is always directly proportional to the solar intensity outside the atmosphere of the earth. The instrumental response can therefore be expressed as

$$R(I) = gS(I) + gB(I) + Z(I)$$

where $S(I)$ is the component of $F(I)$ that is directly proportional to the solar intensity outside the atmosphere and $B(I)$ is the residual radiation falling on the detector.

In order to determine the limb darkening at various points across the solar disk, one must be able to isolate the solar signal $gS(I)$ from the background signal $gB(I)$ and the instrumental zero $Z(I)$. Although the instrumental response $R(I)$ is a direct function of the point number I in each scan, it can be treated as a function of time through the relation

$$I = \frac{t}{\tau}$$

in which t is the elapsed time from the start of the scan and τ is the integration time between successive points in the data. The instrumental response may also be regarded as a function of position in the sky through the relation

$$I = \frac{\alpha}{\tau \cdot 15 \cos \delta}$$

in which α is the angular displacement of the sun with respect to the telescope in seconds of arc since the start of the scan and δ is the solar declination. Because of the functional interdependency of both time and position in the sky to the point number I , it is possible to express the background as a power series

$$B(I) = b_0 + b_1 I + b_2 I^2 + \dots$$

The instrumental zero can also be expressed as

$$Z(I) = z_0 + z_1 I + z_2 I^2 + \dots$$

By substituting these terms in the expression for the instrumental response, one finds that

$$R(I) = gS(I) + (gb_0 + z_0) + (gb_1 + z_1)I + (gb_2 + z_2)I^2 + \dots$$

This can be rewritten as

$$R(I) = gS(I) + C_0 + C_1 I + C_2 I^2 + \dots$$

The coefficients C_0 and C_1 can be computed from the instrumental response at any two points off the limb of the sun provided the nonlinear terms are close to zero. One then obtains a profile that is equal to $gS(I)$ by subtracting the quantity $C_0 + C_1 I$ from each point in the drift scan. When the scan is then normalized to unity at disk center, each point across the disk becomes a direct measure of the solar limb darkening.

3.2 Limb Darkening Reductions in REDUCER

The reduction program REDUCER is normally used to process spectroscopic data from the solar telescopes on Kitt Peak. The low-density magnetic tapes from the Sigma II were therefore rewritten in a high-density format that was suitable for use with REDUCER in the first step of the data reductions.

Observations on a high-density REDUCER tape are stored in pairs of logical records. The first record in each pair is a 100-word block of descriptive information; while the second record is a 2^N -word block of numerical data. Since REDUCER cannot accommodate data blocks that are larger than 4096 words, the integer power N is always less than or equal to twelve.

When a numerical data block is read by REDUCER, it is stored in the one-dimensional array $R(I)$ inside the program. A second array $TR(I)$ is also available in the program. It is used for storing the Fourier transform of the real data in $R(I)$ or for temporarily recording a block of data that has already been partially processed by the program. The data in both $R(I)$ and $TR(I)$ can be modified by calling for any one of a number of special operations that are provided in REDUCER. These operations are initiated by REDUCER commands that are listed on a set of data cards that is read by the program at the start of each run. The

requested commands are generally performed in the order in which they appear on the cards. A partial listing of the command library that is available in REDUCER is given in Table 3.1. The commands that are included in this table were employed throughout the data reductions and will be referred to by name whenever necessary.

The data points for each drift scan were initially stored in two successive 2048-word data blocks on the high-density REDUCER tapes. The following command sequence was therefore used to generate a 4096-word data block from each pair of 2048-word data blocks on the original input file:

```
READ, RESCALE, LENGTH(4096), SHIFT(2048), EXCHANGE  
READ, RESCALE, LENGTH(4096), COMBINE, REVERSE, WRITE
```

The reconstructed drift scans in each daily set were then processed with the following commands:

```
READ, RESCALE, OPTION, WRITE
```

The OPTION subroutine in this sequence of commands produced a normalized solar profile from each drift scan. It also calculated independent measures of the limb darkening at a number of positions across the solar disk.

A linear background function that was based on the first and last eleven points of the data block was subtracted out of each drift scan at the start of OPTION. The highest point in the data block was next located by comparing successive values of $R(I)$. The index I of this point

Table 3.1. Reducer commands.

Command	Explanation
COMBINE	Each element of $TR(I)$ is added to the corresponding element of $R(I)$.
EXCHANGE	The corresponding elements of $R(I)$ and $TR(I)$ are exchanged.
FOURTRAN	The Fourier transform of the real data in $R(I)$ is calculated and stored in $TR(I)$.
INVTRAN	Complex data in $TR(I)$ are inverse transformed into $R(I)$.
LENGTH(n)	$R(I)$ is lengthened or shortened to the number of elements specified by the integer constant n .
OPTION	The auxiliary OPTION subroutine that has been compiled and loaded with REDUCER is executed.
READ	The next pair of logical records on the input file is read into the program. The data block is normalized so that the largest element of $R(I)$ has a value of unity.
RESCALE	The elements of $R(I)$ are rescaled back to their original values on the input file.
REVERSE	The elements of $R(I)$ are rearranged in reverse order.
SHIFT(n)	The index I of each element in $R(I)$ is incremented by the integer constant n . Elements shifted off one end of the array return to the opposite end in a circular fashion.
WRITE	The contents of $R(I)$ are written on the output file in the standard REDUCER format.

was then assigned to the variable IMAX, and the drift scan was normalized to the average value of the data points from IMAX - 50 to IMAX + 50.

The values of $R(I)$ were checked again in the next step of OPTION. The index I of the first point in the block with a value greater than e^{-1} was assigned to the variable LIMBW; while the index I of the last point in the block with a value greater than e^{-1} was assigned to the variable LIMBE. The point positions

$$XLIMBW = LIMBW - 0.50$$

and

$$XLIMBE = LIMBE + 0.50$$

were then defined as the solar limbs. The exact value of e^{-1} was truncated to 0.367 as a matter of convenience in these calculations.

A linear background function that was based on the average instrumental response at the point positions

$$PLACEW = XLIMBW - OFFLIMB$$

and

$$PLACEE = XLIMBE + OFFLIMB$$

was subtracted from the drift scan in the next step of the subroutine. The variable OFFLIMB was 250.0 or 300.0 depending on the observational wavelength. The average instrumental response was computed from one hundred values of $R(I)$ near each position.

The point position of the center of the sun was calculated as

$$\text{CENTER} = \frac{(\text{XLIMBW} + \text{XLIMBE})}{2.0} ,$$

and the solar radius was computed as

$$\text{RSOLAR} = \frac{(\text{XLIMBE} - \text{XLIMBW})}{2.0} .$$

The drift scan was then normalized to the average value of the data points that lay in the range from $\log \mu = -0.01$ on the west side of disk center to $\log \mu = -0.01$ on the east side of disk center.

The limb positions XLIMBW and XLIMBE were located again, and a revised linear background function was subtracted from the scan. Since preliminary tests at several wavelengths indicated that the limb darkening measures would fall along gently curved lines when plotted as a function of $\log \mu$, the final center normalization of the drift scan was derived from a least-squares quadratic fit to $R(I)$ as a function of $\log \mu$. Data points from $\log \mu = -0.015$ on the west side of disk center to $\log \mu = -0.015$ on the east side of disk center were used to compute the coefficients of this quadratic fit. The drift scan was normalized to the instrumental response that was predicted at disk center.

Limb darkening measures were calculated next at a number of positions across the solar disk. The variable XLOGMU defined the $\log \mu$ position of each of these measures. The limb darkening was computed from a least-squares

quadratic fit to $R(I)$ as a function of $\log \mu$ at each position. Data points from

$$\log \mu = XLOGMU - 0.025$$

to

$$\log \mu = XLOGMU + 0.025$$

were used in computing each fit. Since $XLOGMU$ was decremented from -0.05 to -1.00 in successive steps of -0.05 on each side of disk center, each fit to the data was almost completely independent. The limb darkening measures were recorded as formatted output on magnetic tape.

3.3 Limb Darkening Reductions in DRIFT1

The reduction program DRIFT1 averaged the limb darkening measures in each of the daily sets on the output tapes from OPTION. The program also performed a number of statistical tests on the data.

The limb darkening measures for each daily set were read into two arrays in DRIFT1. The array $WEST(I,J)$ was used to store the limb darkening measures from the west limb of the sun; while the array $EAST(I,J)$ was used to store the limb darkening measures from the east limb of the sun. The integer variable J normally varied from 1 to 12 and was used to index the individual drift scans in the daily set. The integer variable I was used to index the limb positions in each scan and always ran from 1 to 20.

The limb darkening measures WEST(I,J) and EAST(I,J) were used to compute two additional measures of the limb darkening at each of the limb positions in every scan. Measures of the average limb darkening in each drift scan were calculated as

$$\text{PAIR}(I,J) = \frac{\text{WEST}(I,J) + \text{EAST}(I,J)}{2.0};$$

while measures of the difference between the west and east lines of the sun were calculated as

$$\text{DIFF}(I,J) = \text{WEST}(I,J) - \text{EAST}(I,J).$$

PAIR(I,J,) and DIFF(I,J) were then treated as independent measures of the solar limb darkening in the remaining stages of the data reductions.

Counts of WEST(I,J), EAST(I,J), PAIR(I,J), and DIFF(I,J) were taken at each of the limb positions in the daily set. The resulting scan counts were stored in the arrays NW(I), NE(I), NP(I), and ND(I). Average limb darkening measures for the daily set were then calculated as

$$\text{AWEST}(I) = \frac{\sum_{J=1}^{\text{NW}(I)} \text{WEST}(I,J)}{\text{NW}(I)},$$

$$\text{AEAST}(I) = \frac{\sum_{J=1}^{\text{NE}(I)} \text{EAST}(I,J)}{\text{NE}(I)},$$

$$\text{APAIR}(I) = \frac{\sum_{J=1}^{\text{NP}(I)} \text{PAIR}(I,J)}{\text{NP}(I)},$$

and

$$ADIFF(I) = \frac{\sum_{J=1}^{ND(I)} DIFF(I,J)}{ND(I)} .$$

Standard deviations for the daily set were also calculated as

$$SWEST(I) = \left[\frac{\sum_{J=1}^{NW(I)} (WEST(I,J) - AWEST(I))^2}{NW(I) - 1} \right]^{1/2},$$

$$SEAST(I) = \left[\frac{\sum_{J=1}^{NE(I)} (EAST(I,J) - AEAST(I))^2}{NE(I) - 1} \right]^{1/2},$$

$$SPAIR(I) = \left[\frac{\sum_{J=1}^{NP(I)} (PAIR(I,J) - APAIR(I))^2}{NP(I) - 1} \right]^{1/2}$$

$$SDIFF(I) = \left[\frac{\sum_{J=1}^{ND(I)} (DIFF(I,J) - ADIFF(I))^2}{ND(I) - 1} \right]^{1/2}.$$

A flag was set in the program each time an individual limb darkening measure deviated from the average by an amount that was greater than 1.96 times the standard deviation.

A Student's test in DRIFT1 checked the statistical hypothesis that the limb darkening was the same on opposite sides of the sun at each limb position. Brandt (1970) has described the general procedure that was followed in the reductions. The test assumed initially that WEST(I,J) and EAST(I,J,) were both drawn from identical populations of limb darkening measures. A composite standard deviation for

WEST(I,J,) and EAST(I,J) was therefore calculated at each limb position as

$$SMEAN = \left[\frac{(NW(I)-1) \cdot SWEST(I)^2 + (NE(I)-1) \cdot SEAST(I)^2}{NW(I) + NE(I) - 2} \right]^{1/2}.$$

The actual difference between the west and east limbs was then computed as

$$DELTA = AWEST(I) - AEAST(I);$$

while an estimator for the standard deviation of DELTA was calculated as

$$SDELTA = \left[\frac{SMEAN^2}{NW(I)} + \frac{SMEAN^2}{NE(I)} \right]^{1/2}.$$

The ratio of DELTA to SDELTA was next defined as the test parameter T. The probability of a given value of T at each limb position was expected to follow a Student's distribution with

$$NF = NW(I) + NE(I) - 2$$

degrees of freedom. Fractiles corresponding to a 5% level of significance in a two-tailed test of T were placed in a table TTEST(NF) inside the program. A flag was set each time the absolute value of an observed T exceeded the appropriate element of TTEST(NF). The difference between AWEST(I) and AEAST(I) was judged to be statistically significant whenever the flag was set.

The numerical results from DRIFT1 were punched onto cards at the end of the program. The data cards for all of

the daily sets at each wavelength were then collected together and processed in DRIFT2.

3.4 Limb Darkening Reductions in DRIFT2

The reduction program DRIFT2 calculated a set of final limb darkening measures at each of the observational wavelengths. Certain statistical tests were also performed on the data.

The numerical results from DRIFT1 were read into a series of arrays in DRIFT2. The average limb darkening measures for the daily sets at each wavelength were stored in the arrays $AWEST1(I,K)$, $A EAST1(I,K)$, $APAIR1(I,K)$, and $ADIFF1(I,K)$; while the standard deviations for the daily sets were stored in the arrays $SWEST1(I,K)$, $SEAST1(I,K)$, $SPAIR1(I,K)$, and $SDIFF1(I,K)$. The scan counts from DRIFT1 were stored in the arrays $NW1(I,K)$, $NE1(I,K)$, $NP1(I,K)$, and $ND1(I,K)$. The integer variable K was used to index the daily sets; while the integer variable I was again used to index the limb positions. The program skipped by the limb positions in each daily set that were affected by sunspots.

Counts of $AWEST1(I,K)$, $A EAST1(I,K)$, $APAIR1(I,K)$, and $ADIFF1(I,K)$ were taken at each limb position. The resulting set counts were stored in the arrays $NNW1(I)$, $NNE1(I)$, $NNP1(I)$, and $NND1(I)$. Final limb darkening measures for the daily sets were then calculated as

$$AWEST2(I) = \frac{\sum_{K=1}^{NNW1(I)} AWEST1(I,K) \cdot NW1(I,K)}{\sum_{K=1}^{NNW1(I)} NW1(I,K)},$$

$$AEAST2(I) = \frac{\sum_{K=1}^{NNE1(I)} AEAST1(I,K) \cdot NE1(I,K)}{\sum_{K=1}^{NNE1(I)} NE1(I,K)},$$

$$APAIR2(I) = \frac{\sum_{K=1}^{NNP1(I)} APAIR1(I,K) \cdot NP1(I,K)}{\sum_{K=1}^{NNP1(I)} NP1(I,K)},$$

and

$$ADIFF2(I) = \frac{\sum_{K=1}^{NND1(I)} ADIFF1(I,K) \cdot ND1(I,K)}{\sum_{K=1}^{NND1(I)} ND1(I,K)}.$$

Weighted standard deviations for the limb darkening measures in the daily sets were also calculated as

$$SWEST2(I) = \left[\frac{\sum_{K=1}^{NNW1(I)} (NW1(I,K) - 1) \cdot SWEST1(I,K)^2}{\sum_{K=1}^{NNW1(I)} (NW1(I,K) - 1)} \right]^{1/2},$$

$$SEAST2(I) = \left[\frac{\sum_{K=1}^{NNE1(I)} (NE1(I,K) - 1) \cdot SEAST1(I,K)^2}{\sum_{K=1}^{NNE1(I)} (NE1(I,K) - 1)} \right]^{1/2},$$

$$\text{SPAIR2}(I) = \left[\frac{\sum_{K=1}^{\text{NNP1}(I)} (\text{NP1}(I,K) - 1) \cdot \text{SPAIR1}(I,K)^2}{\sum_{K=1}^{\text{NNP1}(I)} (\text{NP1}(I,K) - 1)} \right]^{1/2},$$

and

$$\text{SDIFF2}(I) = \left[\frac{\sum_{K=1}^{\text{NND1}(I)} (\text{ND1}(I,K) - 1) \cdot \text{SDIFF1}(I,K)^2}{\sum_{K=1}^{\text{NND1}(I)} (\text{ND1}(I,K) - 1)} \right]^{1/2}.$$

The weighted standard deviations and the final limb darkening measures were printed out at each limb position. Final counts of the scans at each limb position were also compiled and printed out by the program.

3.5 Scattered Light Reductions

The background radiation near the limb of the sun was measured at each of the observational wavelengths from the normalized drift scans that had been used to determine the limb darkening across the disk. Although this background radiation actually resulted from a number of different physical processes and instrumental effects, it will be referred to collectively as scattered light.

Each normalized drift scan from the limb darkening reductions was initially processed with the following

REDUCER commands:

```
READ, RESCALE, OPTION, WRITE
EXCHANGE, REVERSE, WRITE.
```

The OPTION subroutine in this sequence of commands filled a shortened version of the array R(I) with those elements in each drift scan that ranged from LIMBW-OFFLIMB-50 to LIMBW. The subroutine also filled a shortened version of TR(I) with those elements in each scan that ranged from LIMBE TO LIMBE+OFFLIMB+50. The scans on the output tape thus alternated between the west and east limbs of the sun and were 301 and 351 points in length depending on the value of OFFLIMB.

The short scans of the background radiation were processed with the following commands:

```
READ, RESCALE, REVERSE, OPTION(arg1, arg2)
```

The OPTION subroutine in this series of commands calculated observational measures of the scattered light at a number of positions off the limb of the sun. The first argument of the OPTION command was a label for the east or west limb of the sun. The second argument was the cosine of the solar declination on the date of observation.

The point position

$$RZERO = (0.367 - R(I)) / (R(2) - R(I)) + 1.0$$

was defined as the solar limb in each background scan.

Point positions for the scattered light measures were then calculated as

$$POS = RSEC / (0.60 \cdot \text{COSDEC}) + RZERO.$$

The variable RSEC was incremented from 1.0 to 10.0 in steps of 1.0 and then from 15.0 to 60.0 in steps of 5.0. The

variable COSDEC was the cosine of the solar declination. Measures of the scattered light were therefore taken at twenty positions from 1 to 60" from the limb. The scattered light at the first ten positions off the limb was calculated by linearly interpolating between the data points on either side of the point position defined by POS. The instrumental response changed more gradually at the ten positions farther out, and the scattered light was calculated by averaging together five linearly interpolated points from POS-2.0 to POS+2.0. The scattered light measures from 1 to 10" from the limb thus have a lower statistical weight than those from 15 to 60" from the limb. The scattered light measures for each scan were recorded as formatted output on magnetic tape.

The scattered light measures from OPTION were processed in the reduction program DRIFT1. As in the previous limb darkening reductions, DRIFT1 averaged together the individual measures in each daily set and performed a number of statistical tests on the data. Final scattered light measures at each wavelength were computed in DRIFT2.

CHAPTER 4

THE STATISTICAL TEST RESULTS

A number of statistical tests were performed in DRIFT1 and DRIFT2. These tests were expected to provide direct evidence of any inconsistencies in the experimental results. Statistically significant deviations from the mean at each limb position were flagged in DRIFT1. A Student's test in DRIFT1 also checked the statistical agreement between the west and east limbs of the sun. A similar Student's test in DRIFT2 was used to check the consistency of the limb darkening measures from different days. The results of the statistical tests in DRIFT1 are discussed in Section 4.1. The statistical test results from DRIFT2 are presented in Section 4.2.

4.1 Statistical Results from DRIFT1

A flag was set in the reduction program DRIFT1 each time an individual limb darkening measure deviated from the mean by more than 1.96 times the standard deviation. Such deviations were expected to occur 5% of the time at each of the limb positions in every daily set. Out of the 74960 individual limb darkening measures that were computed in this research, only 2700 were flagged by the program. This corresponds to a 3.6% rate of occurrence. Since the

variance of the limb darkening measures was determined primarily by the amplitude of the temperature fluctuations in the atmosphere, this result was probably caused by the granulation in the solar atmosphere. The least-squares quadratic fitting procedure that was used in the reductions in OPTION could also have had some effect on the distribution of the individual measures at each position.

On some days there were sunspots or other active regions that passed through a few of the scans in each of the daily sets. The frequency of unusually large deviations from the mean at such locations was roughly the same as at other positions on the sun. This result undoubtedly stemmed from the fact that the standard deviation itself became proportionally larger whenever a few of the scans in a daily set passed over an anomalous region on the disk. The limb darkening measures at these locations were obviously not reliable, however, and were therefore deleted from the data that were processed in DRIFT2.

Large deviations from the mean occurred exactly 5% of the time in the scattered light reductions. The scattered light measures thus appear to be normally distributed. This result is particularly reassuring since the background radiation in each scan was expected to be almost entirely caused by random statistical processes.

The Student's test in DRIFT1 was designed to test the hypothesis that the limb darkening was the same on

opposite limbs of the sun. The sign of DELTA at each limb position in every daily set is listed in Table 4.1. Parentheses signify that the absolute value of T was greater than the fractile of the Student's distribution that corresponded to a 5% level of significance in the test. Each limb position that was affected by a sunspot is underlined.

Substantially fewer DELTA of one sign or the other in a daily set would indicate that the scans were systematically tilted. Such asymmetric effects could be caused by a nonlinear drift in the instrumental zero, a slow variation in the atmospheric transmission, or a slight change in gain over the duration of each scan.

The statistical hypothesis that a positive or negative value of DELTA was equally likely at each limb position was tested in every daily set. The likelihood of having K positive or K negative values of DELTA in a set of N samples was expected to follow a binomial distribution

$$W_K^N = \frac{N!(0.50)^N}{K!(N-K)!}.$$

The strictest level of significance for which the test hypothesis could be rejected for each daily set was therefore calculated as

Table 4.1. Statistical test results from DRIFT1: sign of DELTA for limb darkening measures.

	Position Index I																									
Daily set	1	2	3	4	5	6	7	8	9	10	11	12	13	14	15	16	17	18	19	20	N ₋	N ₊	α_{\pm}	N _t	α_t	
<u>10840.10 Å</u>																										
1/31/74	+	-	+	-	+	+	-	+	-	-	-	-	+	+	-	+	-	-	+	-	11	9	82.4%	0	100.0%	
2/01/74	+	(-)	-	+	+	-	-	-	-	-	-	(-)	-	-	-	-	-	+	-	-	16	4	1.2%	2	26.4%	
2/02/74	-	+	-	(-)	-	-	-	-	(-)	-	+	-	-	-	-	-	-	-	-	+	17	3	0.3%	2	26.4%	
<u>10854.00 Å</u>																										
2/01/74	+	(-)	+	+	-	-	(-)	+	+	-	(-)	-	-	+	-	-	+	+	+	-	11	9	82.4%	3	7.6%	
2/02/74	-	-	+	-	+	+	+	-	-	(-)	+	-	-	-	-	-	(-)	(-)	(-)	(-)	15	5	4.1%	5	0.3%	
2/02/74	-	-	+	+	-	-	-	(-)	-	+	+	+	-	-	-	(-)	-	-	-	-	15	5	4.1%	2	26.4%	
<u>10865.00 Å</u>																										
1/31/74	(+)	+	+	+	(+)	-	-	-	+	(+)	+	-	+	-	-	-	+	+	-	-	9	11	82.4%	3	7.6%	
2/01/74	(-)	-	-	+	-	+	+	-	-	-	-	-	-	-	-	-	+	+	+	-	14	6	11.5%	1	64.2%	
2/02/74	+	-	-	-	-	-	+	+	-	-	-	-	-	-	-	(-)	-	-	-	-	17	3	0.3%	1	64.2%	
<u>12466.63 Å</u>																										
2/16/74	-	+	+	+	+	-	-	-	-	+	+	+	+	-	(+)	+	+	+	+	+	6	14	11.5%	1	64.2%	
4/21/74	-	-	+	-	+	+	(-)	-	+	+	-	-	-	-	-	+	+	+	-	-	13	7	26.3%	1	64.2%	
4/22/74	+	-	+	+	+	+	-	-	+	+	(+)	+	(+)	(+)	+	+	+	-	+	+	4	16	1.2%	3	7.6%	
4/29/74	(-)	+	(-)	+	-	+	+	+	+	-	+	+	+	+	-	-	+	+	-	-	8	12	50.3%	2	26.4%	
4/30/74	-	+	(+)	+	+	+	-	-	+	+	-	-	+	+	-	+	+	+	+	+	6	14	11.5%	1	64.2%	
<u>12505.51 Å</u>																										
2/16/74	-	(+)	(+)	+	(-)	+	+	(+)	-	(+)	-	-	+	+	+	+	+	+	+	-	6	14	11.5%	5	0.3%	
4/21/74	-	-	+	-	-	-	+	+	-	(-)	(+)	+	+	-	+	+	+	+	+	-	9	11	82.4%	2	26.4%	
4/22/74	-	-	+	-	+	-	+	-	+	-	+	+	+	(+)	+	+	-	+	+	+	7	13	26.3%	1	64.2%	
4/29/74	-	-	-	+	+	+	-	-	-	(-)	-	-	-	-	+	-	+	-	+	+	13	7	26.3%	1	64.2%	
4/30/74	-	-	-	-	(+)	+	+	+	+	-	-	-	+	(-)	-	+	+	+	-	-	11	9	82.4%	2	26.4%	
<u>16222.00 Å</u>																										
2/15/74	+	+	(+)	-	+	+	+	+	(+)	-	(+)	+	-	-	+	+	+	+	+	-	5	14	6.4%	2	24.5%	
2/24/74	+	+	+	+	(+)	+	+	-	+	+	+	-	+	+	+	+	-	+	+	+	3	17	0.3%	1	64.2%	
2/26/74	+	-	+	+	+	+	+	+	-	+	-	+	+	-	+	+	-	+	-	-	7	13	26.3%	0	100.0%	
3/16/74	+	+	-	+	+	-	+	+	+	+	(+)	+	(+)	+	-	-	+	+	-	-	6	14	11.5%	2	26.4%	
4/20/74	+	-	-	+	-	+	+	+	-	+	-	+	+	-	-	+	+	+	-	-	9	11	82.4%	0	100.0%	
4/21/74	-	-	+	+	+	+	+	+	+	-	+	+	-	-	-	+	+	+	+	+	6	14	11.5%	0	100.0%	
4/28/74	+	+	+	+	+	+	+	+	+	+	+	(+)	+	(+)	+	+	+	+	+	+	0	20	0.0%	2	26.4%	
4/29/74	-	+	-	+	+	-	+	+	+	+	+	(+)	+	(+)	+	+	-	-	-	-	7	13	26.3%	1	64.2%	

Table 4.1.--Continued Statistical test results from DRIFT1: sign of DELTA for limb darkening measures.

	Position Index I																									
Daily set	1	2	3	4	5	6	7	8	9	10	11	12	13	14	15	16	17	18	19	20	N ₋	N ₊	a _±	N _t	a _t	
<u>16513.18 Å</u>																										
2/15/74	-	+	(+)	-	-	+	-	+	+	+	-	-	-	-	+	-	-	-	-	-	13	6	16.7%	0	100.0%	
2/24/74	+	-	-	-	+	-	-	-	+	-	-	-	-	-	+	+	+	+	+	-	12	8	50.3%	0	100.0%	
2/25/74	+	-	-	-	-	-	-	-	-	(-)	-	-	(-)	(-)	(-)	(-)	-	-	(-)	(-)	19	1	0.0%	6	0.0%	
2/26/74	+	-	+	+	+	-	+	-	-	+	-	-	-	+	+	+	+	+	-	-	9	11	82.4%	0	100.0%	
3/16/74	-	-	+	(-)	(-)	(-)	-	+	-	-	+	+	-	-	+	+	+	+	+	+	11	9	82.4%	3	7.6%	
4/20/74	-	+	-	-	-	-	+	-	+	-	+	-	+	-	+	+	+	+	+	-	11	9	82.4%	0	100.0%	
4/21/74	+	+	+	+	+	+	-	+	+	-	+	-	-	-	-	-	-	-	-	(-)	11	9	82.4%	1	64.2%	
4/28/74	-	+	+	+	+	+	+	-	+	+	-	+	+	-	-	(-)	(-)	-	-	-	10	10	100.0%	2	26.4%	
4/29/74	-	+	+	+	+	-	-	-	+	+	+	+	+	+	+	+	+	-	+	+	5	15	4.1%	0	100.0%	
<u>21855.59 Å</u>																										
2/24/74	-	+	-	+	-	(-)	-	-	+	-	-	-	-	-	+	+	-	-	+	+	13	7	26.3%	1	64.2%	
4/21/74	+	-	-	+	+	-	+	+	+	+	-	+	-	+	+	+	+	+	+	+	5	15	4.1%	0	100.0%	
4/28/74	+	-	-	+	+	-	-	-	+	+	-	-	+	-	+	-	+	-	+	+	11	9	82.4%	0	100.0%	
4/29/74	+	+	-	+	-	+	-	-	+	+	-	-	+	+	+	-	-	-	-	+	10	10	100.0%	0	100.0%	
<u>21907.47 Å</u>																										
2/24/74	+	+	+	+	+	(+)	+	+	+	+	+	+	+	+	+	+	+	+	+	+	0	20	0.0%	1	64.2%	
3/17/74	-	-	-	-	-	+	-	-	+	+	-	-	-	-	-	-	-	-	-	-	17	3	0.3%	0	100.0%	
4/20/74	-	-	+	+	-	-	-	(+)	+	-	-	-	-	-	-	-	+	+	+	+	12	8	50.3%	1	64.2%	
4/21/74	+	-	-	+	+	(-)	-	-	-	(+)	-	+	+	+	-	-	+	-	+	-	11	9	82.4%	2	26.4%	
4/28/74	+	+	-	+	-	-	-	-	+	-	-	-	-	-	+	+	-	-	-	+	12	8	50.3%	0	100.0%	
4/29/74	+	+	-	-	+	+	+	-	+	+	-	-	-	-	+	-	-	-	-	-	12	8	50.3%	0	100.0%	
<u>23121.03 Å</u>																										
2/24/74	+	-	+	+	+	+	+	+	-	-	-	-	-	-	(-)	-	-	-	-	-	13	7	26.3%	1	64.2%	
2/25/74	-	-	+	+	+	-	+	+	+	-	-	-	(-)	(-)	-	-	-	-	+	+	12	8	50.3%	2	26.4%	
3/16/74	-	(-)	(-)	-	-	-	-	-	-	-	-	-	-	-	-	-	-	-	-	-	20	0	0.0%	2	26.4%	
<u>23127.19 Å</u>																										
2/24/74	-	-	+	-	-	-	+	-	-	-	+	-	-	-	-	-	-	-	+	+	15	5	4.1%	0	100.0%	
2/25/74	+	-	+	+	+	-	+	+	+	+	-	+	-	+	-	-	-	(-)	-	-	10	10	100.0%	1	64.2%	
3/16/74	-	-	+	-	-	-	-	+	+	-	+	+	+	+	+	+	-	-	-	-	11	9	82.4%	0	100.0%	
3/17/74	+	-	-	+	+	+	-	+	+	+	+	+	+	-	+	-	+	+	+	+	5	15	4.1%	0	100.0%	
4/20/74	-	+	+	+	-	+	-	-	-	-	+	-	-	-	-	-	-	-	-	(-)	15	5	4.1%	1	64.2%	
4/29/74	-	-	-	-	+	-	-	-	-	-	-	+	-	+	+	+	+	+	+	+	11	9	82.4%	0	100.0%	

Table 4.1.--Continued Statistical test results from DRIFT1: sign of DELTA for limb darkening measures.

Daily set	Position Index I																				N ₋	N ₊	n±	N _t	a _t
	1	2	3	4	5	6	7	8	9	10	11	12	13	14	15	16	17	18	19	20					
<u>23132.73 Å</u>																									
3/17/74	-	+	-	-	-	-	+	-	+	+	+	+	+	-	-	-	-	-	-	(-)	13	7	26.3%	1	64.2%
4/20/74	-	+	-	+	+	+	-	+	+	-	+	-	+	-	-	-	-	-	-	-	12	8	50.3%	0	100.0%
4/21/74	+	+	-	+	+	-	+	-	-	-	+	+	-	-	-	-	-	+	-	-	12	8	50.3%	0	100.0%
4/22/74	+	-	-	-	(-)	-	+	-	+	-	+	+	+	-	-	-	-	-	-	-	14	6	11.5%	1	64.2%
4/29/74	+	-	-	+	-	-	-	+	-	-	+	+	+	-	+	+	+	+	+	+	8	12	50.3%	0	100.0%
4/30/74	-	-	+	+	+	+	+	-	-	-	(-)	-	-	-	+	-	-	-	-	-	14	6	11.5%	1	64.2%
<u>38839.36 Å</u>																									
5/12/74	+	+	+	+	-	+	+	+	+	-	+	-	+	-	+	-	+	+	-	-	7	11	48.1%	0	100.0%
5/14/74	+	+	(+)	+	+	+	+	(+)	+	+	+	-	+	+	(-)	(-)	-	(-)	-	-	7	13	26.3%	5	0.3%
5/15/74	(+)	+	-	+	-	-	+	+	-	+	-	(-)	+	+	(-)	-	-	-	-	-	12	7	35.9%	2	24.5%
<u>38862.02 Å</u>																									
5/12/74	-	+	-	-	+	+	-	+	+	-	+	-	+	-	-	-	-	-	+	+	9	9	100.0%	0	100.0%
5/14/74	+	+	+	+	+	+	+	(+)	-	+	+	+	-	+	+	+	+	+	+	+	2	18	0.0%	1	64.2%
5/15/74	(+)	+	+	+	-	(+)	+	+	+	+	-	-	+	+	+	+	+	+	+	+	3	16	0.4%	1	62.3%
<u>45908.50 Å</u>																									
5/21/74	-	-	-	-	-	-	-	-	(-)	(-)	(-)	-	(-)	(-)	(-)	(-)	(-)	-	-	-	20	0	0.0%	8	0.0%
5/24/74	-	-	-	+	-	-	+	-	+	-	(-)	-	(-)	(-)	-	-	-	-	-	+	16	4	1.2%	3	7.6%
5/25/74	-	-	(-)	(-)	(-)	-	(-)	(-)	(-)	(-)	(-)	(-)	-	(-)	(-)	-	(-)	-	-	-	20	0	0.0%	12	0.0%
<u>46142.57 Å</u>																									
5/21/74	(+)	+	+	+	+	+	+	+	(-)	+	+	+	+	+	+	+	+	+	+	+	1	19	0.0%	2	26.4%
5/24/74	+	-	+	+	+	+	+	+	+	+	+	+	+	+	+	(+)	+	+	+	+	1	19	0.0%	1	64.2%
5/25/74	+	-	+	+	+	+	+	+	+	+	+	+	-	+	+	+	-	-	-	-	6	14	11.5%	0	100.0%
<u>85636.32 Å</u>																									
5/20/74	+	+	-	-	-	-	-	-	-	+	-	+	-	(-)	-	+	-	-	-	-	15	5	4.1%	1	64.2%
5/25/74	-	-	-	(-)	+	(-)	-	(-)	-	-	-	(-)	-	+	-	-	-	(-)	(-)	(-)	18	2	0.0%	7	0.0%
5/26/74	-	-	-	+	-	+	-	+	+	-	-	-	-	+	-	+	+	-	(-)	-	12	7	35.9%	1	62.3%
<u>104007.55 Å</u>																									
5/20/74	+	+	+	+	+	(-)	-	-	-	+	+	+	-	+	+	+	-	-	-	-	9	11	82.4%	1	64.2%
5/25/74	+	+	+	+	+	+	-	-	+	-	-	-	-	-	(-)	+	(-)	+	+	+	9	11	82.4%	2	26.4%
5/26/74	(-)	-	-	-	-	+	-	-	-	+	-	-	-	+	+	-	+	-	-	-	14	5	6.4%	0	100.0%

$$\alpha_{\pm} = \begin{cases} 2 \sum_{K=0}^{N_+} W_K^N & \text{for } N_+ < N_- \\ 1 & \text{for } N_+ = N_- \\ 2 \sum_{K=0}^{N_-} W_K^N & \text{for } N_+ > N_- \end{cases} .$$

The computed values of α_{\pm} are included in Table 4.1.

A slight tilt to the scans in a daily set was not expected to have much of an effect on the final limb darkening measures since the individual measures from the west and east limbs of the sun were paired together in the data reductions. If the tilt were great enough to cause the values of DELTA to fail the Student's test significantly more often than 5% of the time, however, there could be systematic effects which would need to be considered.

The statistical hypothesis that DELTA had a 5% probability of failing the Student's test was itself tested in each daily set. The likelihood of K failures in N samples was expected to follow a distribution

$$W_K^N = \frac{N! (0.05)^K (0.95)^{N-K}}{K! (N-K)!} .$$

The strictest level of significance for which the test hypothesis could be rejected was therefore calculated as

$$\alpha_T = \sum_{K=N_T}^N W_K^N .$$

The computed values of α_T are also included in Table 4.1.

The values of DELTA for four of the daily sets which have pronounced tilts are presented graphically in Figures 4.1 to 4.4. The daily set at 16513.18 Å is the only daily set at that wavelength which is significantly tilted. The two daily sets at 45908.50 Å, however, are both tilted in the same direction. Since the observed spectrum is depressed by atmospheric lines throughout this particular region, it is possible that an undetected solar line was Doppler shifted in or out of the bandpass of the spectrometer in scanning from one side of the sun to the other at this wavelength. The daily set at 85636.32 Å has a pronounced asymmetry at the extreme limb. This asymmetry is probably caused by seeing.

The statistical test results from DRIFT1 for the scattered light measures are given in Table 4.2. The values of DELTA for five of the daily sets which have pronounced tilts are then presented graphically in Figures 4.5 to 4.9. The tendency of the instrumental zero of the silicon diode detector to drift upward in small steps is probably responsible for the tilts from 10840.10 to 10865.00 Å. The tilts at the other observational wavelengths are probably also caused by irregular changes in the thermal background or the

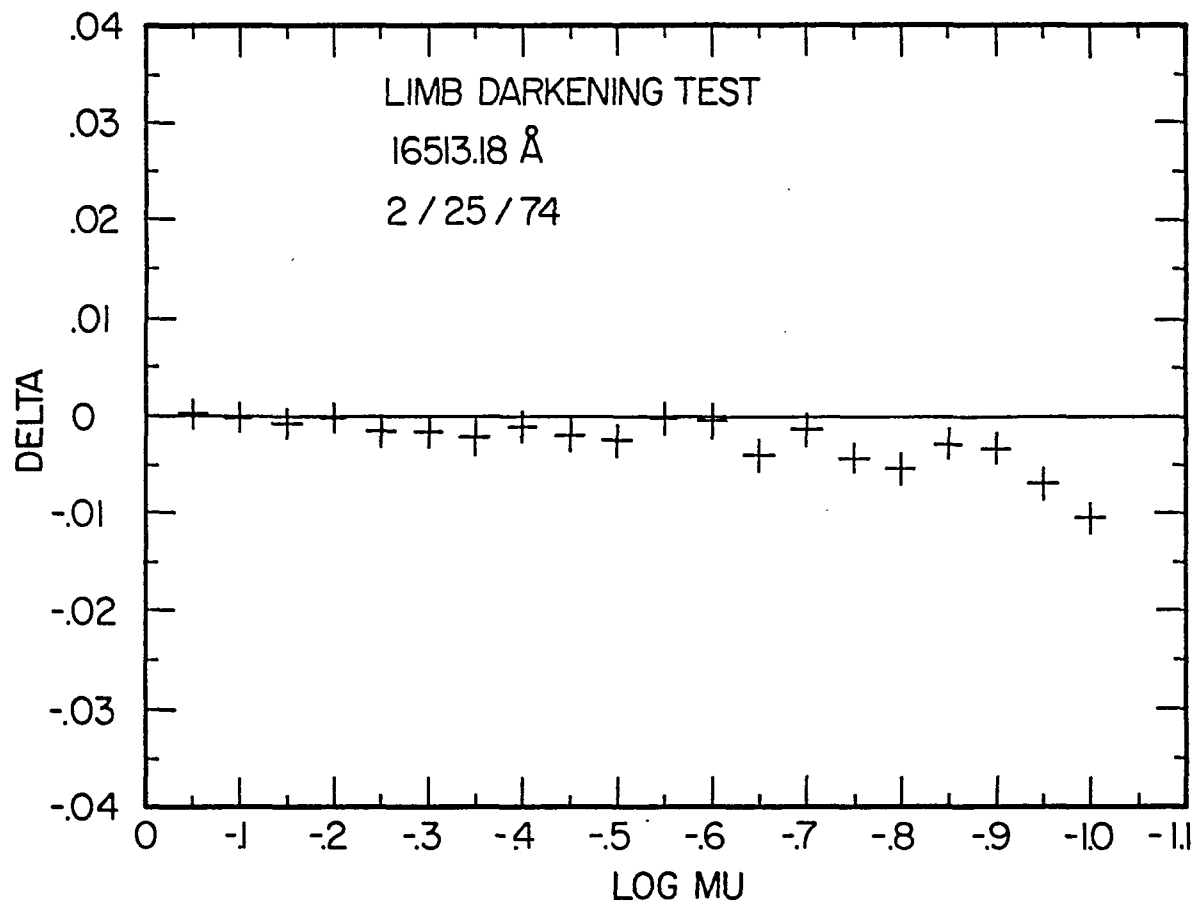


Figure 4.1. Values of DELTA for limb darkening measures at 16513.18 Å on February 25, 1974.

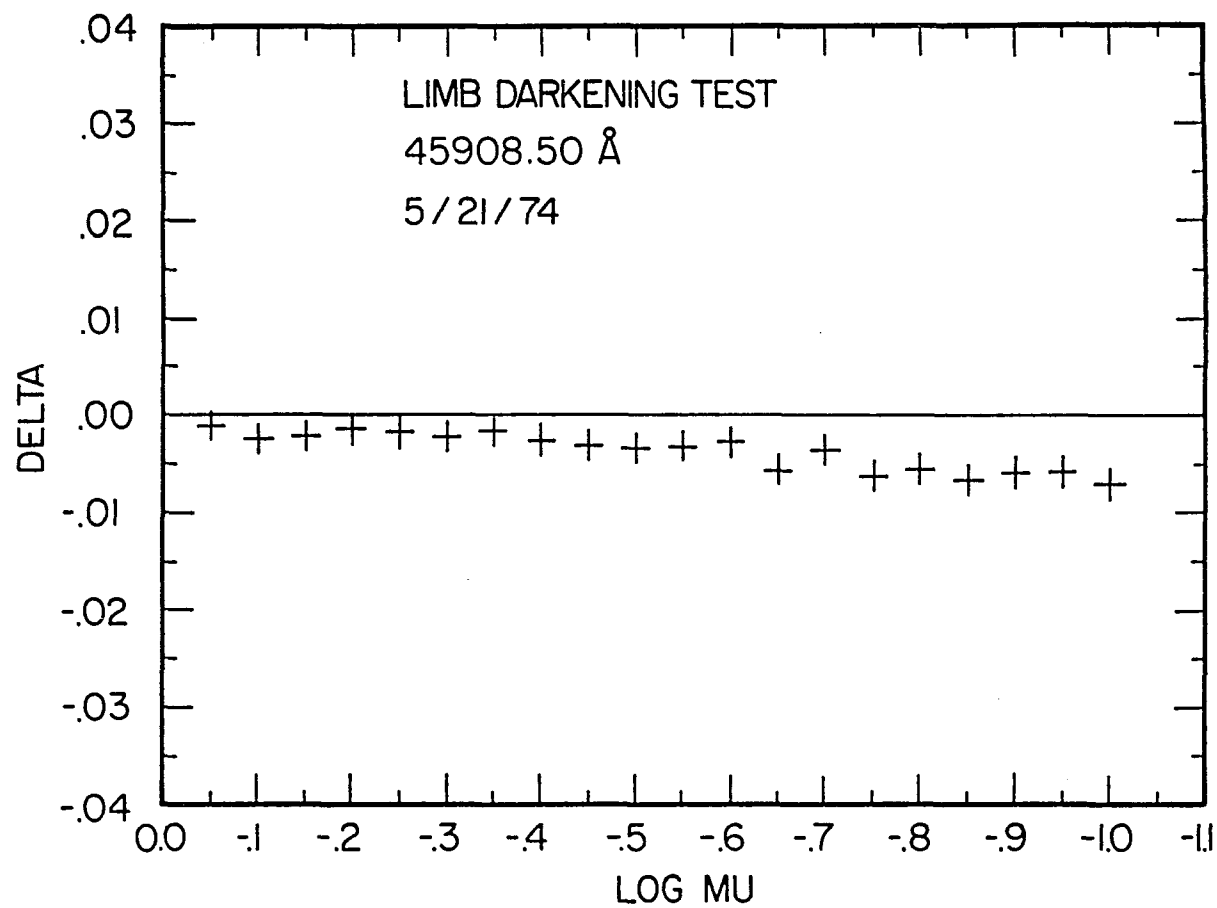


Figure 4.2. Values of DELTA for limb darkening measures at 45908.50 Å on May 21, 1974.

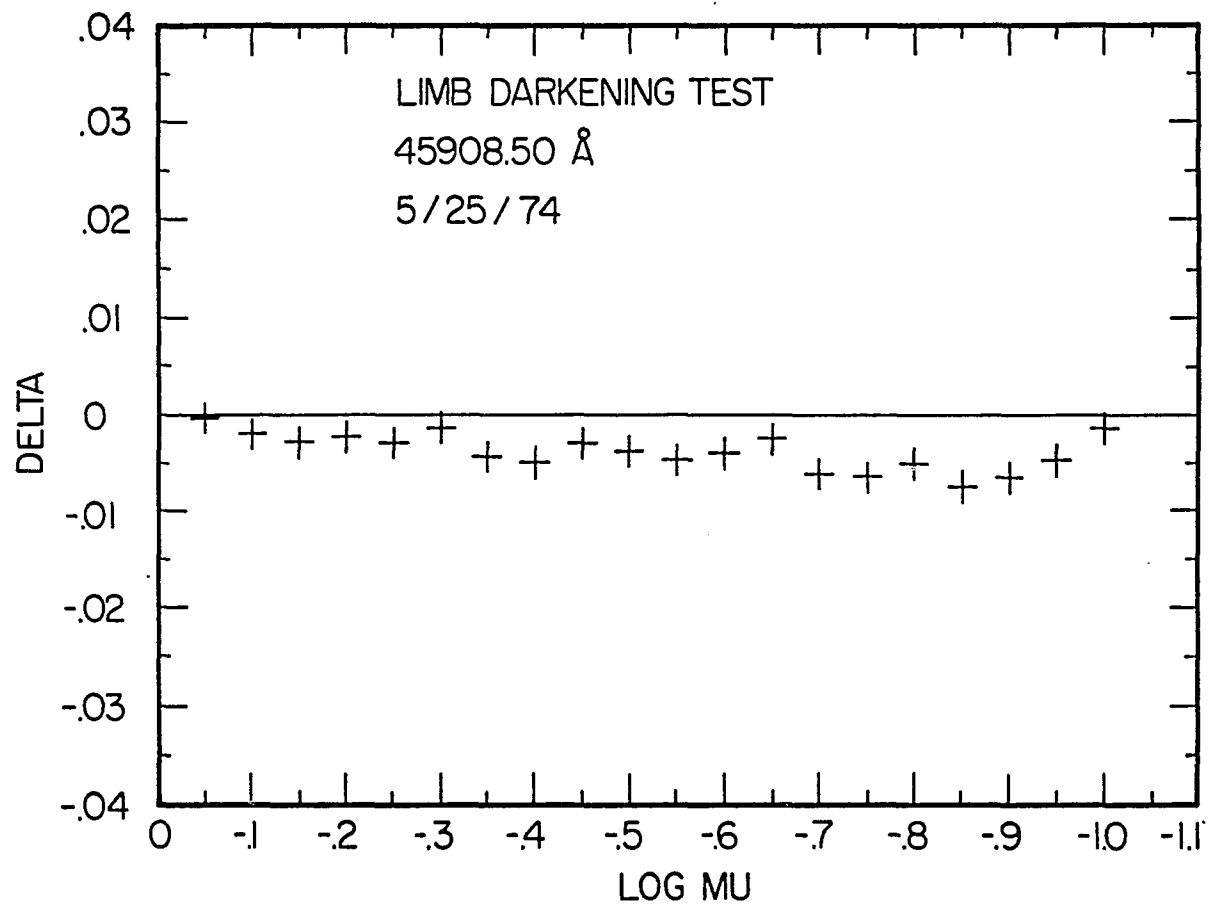


Figure 4.3. Values of DELTA for limb darkening measures at 45908.50 Å on May 25, 1974.

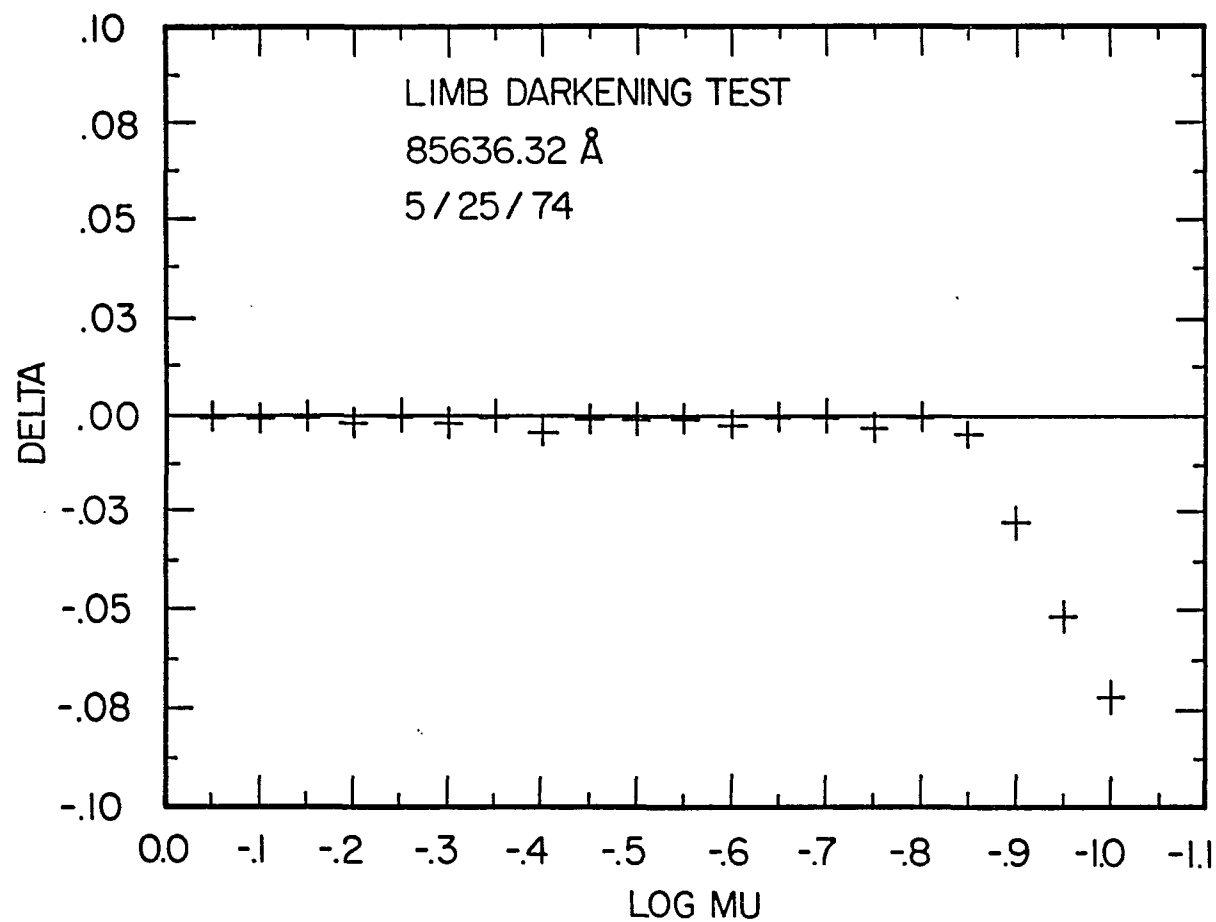


Figure 4.4. Values of DELTA for limb darkening measures at 85636.32 Å on May 25, 1974.

Table 4.2. Statistical test results from DRIFT1: sign of DELTA for scattered light measures.

	Position Index I																									
Daily set	1	2	3	4	5	6	7	8	9	10	11	12	13	14	15	16	17	18	19	20	N ₋	N ₊	α_{\pm}	N _t	α_t	
<u>10840.10 Å</u>																										
1/31/74	-	-	-	-	-	+	+	+	-	+	-	(-)	(-)	(-)	(-)	(-)	(-)	(-)	(-)	(-)	16	4	1.2%	9	0.0%	
2/01/74	-	-	-	-	-	-	-	(-)	(-)	(-)	(-)	(-)	(-)	(-)	(-)	(-)	(-)	(-)	(-)	(-)	20	0	0.0%	13	0.0%	
2/02/74	-	-	-	-	-	-	-	-	-	-	(-)	(-)	(-)	-	-	-	-	-	-	(-)	20	0	0.0%	4	1.6%	
<u>10854.00 Å</u>																										
2/01/74	-	-	-	-	-	-	-	-	-	-	(-)	(-)	(-)	(-)	(-)	(-)	(-)	(-)	-	-	20	0	0.0%	8	0.0%	
2/02/74	+	+	+	-	+	-	-	-	-	-	-	-	-	-	-	(-)	-	-	-	-	16	4	1.2%	1	64.2%	
2/02/74	+	+	-	-	-	-	-	-	-	(-)	-	(-)	(-)	(-)	-	(-)	(-)	(-)	(-)	-	18	2	0.0%	8	0.0%	
<u>10865.00 Å</u>																										
1/31/74	-	-	-	-	-	-	-	-	-	+	+	-	-	-	-	(-)	-	(-)	-	(-)	18	2	0.0%	3	7.6%	
2/01/74	-	-	-	-	-	-	-	-	-	-	(-)	(-)	(-)	(-)	(-)	(-)	(-)	(-)	(-)	(-)	20	0	0.0%	10	0.0%	
2/02/74	-	-	-	-	+	+	+	+	-	-	-	-	-	-	-	-	+	+	-	+	13	7	26.3%	0	100.0%	
<u>12466.63 Å</u>																										
2/16/74	+	-	-	-	-	-	+	+	+	+	-	+	+	-	-	-	-	+	-	-	13	7	26.3%	0	100.0%	
4/21/74	-	+	+	+	+	+	+	+	+	+	+	+	+	+	-	+	+	+	+	+	2	18	0.0%	0	100.0%	
4/22/74	+	-	+	+	+	+	+	+	+	+	+	+	+	+	+	+	-	-	-	-	5	15	4.1%	0	100.0%	
4/29/74	+	+	+	+	+	+	+	+	+	+	+	-	-	-	(-)	-	-	(-)	(-)	(-)	9	11	82.4%	4	1.6%	
4/30/74	-	+	-	-	-	-	-	-	+	+	+	+	+	+	+	+	+	+	+	+	7	13	26.3%	0	100.0%	
<u>12505.51 Å</u>																										
2/16/74	+	+	+	-	-	+	+	+	+	+	-	+	-	-	-	-	-	-	-	(-)	11	9	82.4%	1	64.2%	
4/21/74	-	+	+	+	-	-	-	+	+	+	+	+	+	+	+	+	+	+	+	+	4	16	1.2%	0	100.0%	
4/22/74	-	+	+	+	+	-	-	+	-	-	-	-	-	-	-	+	+	-	-	-	13	7	26.3%	0	100.0%	
4/29/74	+	-	-	-	-	-	-	-	-	-	-	+	-	+	-	-	-	-	-	-	17	3	0.3%	0	100.0%	
4/30/74	-	-	+	+	+	-	-	-	-	-	+	+	+	+	+	+	+	+	+	+	7	13	26.3%	0	100.0%	
<u>16222.00 Å</u>																										
2/15/74	-	-	+	+	-	-	+	+	-	-	+	+	+	+	-	-	+	-	-	-	11	9	82.4%	0	100.0%	
2/24/74	+	+	+	+	+	+	+	+	+	+	+	+	+	+	+	+	+	+	+	+	0	20	0.0%	0	100.0%	
2/26/74	+	+	+	(+)	(+)	+	+	+	+	(+)	(+)	+	-	-	-	+	+	+	+	+	3	17	0.3%	4	1.6%	
3/16/74	+	-	-	+	+	+	+	+	+	+	+	-	-	-	-	-	-	-	-	-	10	10	100.0%	0	100.0%	
4/20/74	-	-	-	-	-	-	-	-	-	-	-	+	-	-	-	-	+	+	+	+	15	5	4.1%	0	100.0%	
4/21/74	+	-	-	+	+	+	+	+	+	+	-	-	-	-	-	-	-	-	-	-	12	8	50.3%	0	100.0%	
4/28/74	+	+	-	-	-	+	+	+	+	+	+	+	+	+	+	+	+	+	-	-	5	15	4.1%	0	100.0%	
4/29/74	+	+	+	+	+	+	-	+	+	+	+	+	+	+	+	+	+	+	+	+	2	18	0.0%	0	100.0%	

Table 4.2.--Continued Statistical test results from DRIFT1: sign of DELTA for scattered light measures.

	Position Index I																								
Daily set	1	2	3	4	5	6	7	8	9	10	11	12	13	14	15	16	17	18	19	20	N ₋	N ₊	α_{\pm}	N _t	α_t
<u>16513.18 Å</u>																									
2/15/74	-	-	-	-	-	-	-	-	-	-	-	+	+	+	+	-	-	+	+	+	13	7	26.3%	0	100.0%
2/24/74	-	-	-	-	-	-	-	-	+	+	+	+	-	-	-	-	-	-	+	+	15	5	4.1%	0	100.0%
2/25/74	-	-	-	-	-	-	-	-	-	-	-	-	+	+	-	+	+	+	-	-	15	5	4.1%	0	100.0%
2/26/74	-	-	-	-	-	-	-	-	-	-	-	-	-	-	+	+	-	+	+	+	15	5	4.1%	0	100.0%
3/16/74	+	+	-	-	-	-	-	-	-	-	-	-	-	+	+	+	+	+	+	(+)	11	9	82.4%	1	64.2%
4/20/74	-	-	+	+	+	-	-	-	-	-	-	-	-	-	-	-	-	-	-	-	17	3	0.3%	0	100.0%
4/21/74	-	-	-	-	-	-	-	-	+	+	+	+	+	+	+	+	-	-	+	-	11	9	82.4%	0	100.0%
4/28/74	-	-	-	-	+	+	+	-	+	+	+	+	+	+	+	+	+	+	+	+	5	15	4.1%	0	100.0%
4/29/74	+	+	+	-	+	+	+	+	+	+	+	+	+	(+)	(+)	+	+	+	+	+	1	19	0.0%	2	26.4%
<u>21855.59 Å</u>																									
2/24/74	-	+	+	-	+	+	-	+	+	+	-	-	-	-	-	-	-	-	(-)	(-)	13	7	26.3%	2	26.4%
4/21/74	+	+	+	+	+	+	+	-	-	-	-	-	-	+	+	-	-	-	+	-	10	10	100.0%	0	100.0%
4/28/74	+	(+)	(+)	(+)	(+)	+	-	-	-	-	+	+	+	-	+	+	+	+	+	+	5	15	4.1%	4	1.6%
4/29/74	-	-	+	+	+	+	-	-	-	-	-	+	+	+	+	+	+	+	+	+	7	13	26.3%	0	100.0%
<u>21907.47 Å</u>																									
4/24/74	-	-	+	+	+	+	+	+	+	+	+	+	+	+	+	+	+	+	+	+	2	18	0.0%	0	100.0%
3/17/74	+	+	-	-	-	-	-	-	-	+	+	-	-	+	+	+	+	+	+	+	9	11	82.4%	0	100.0%
4/20/74	-	+	+	+	+	+	+	+	+	+	+	+	+	+	-	-	-	+	-	-	7	13	26.3%	0	100.0%
4/21/74	-	-	-	-	-	-	-	-	(-)	-	-	-	-	+	-	+	+	+	+	-	15	5	4.1%	1	64.2%
4/28/74	-	-	+	-	-	-	+	-	-	-	-	-	-	-	-	+	+	-	-	+	15	5	4.1%	0	100.0%
4/29/74	(+)	+	-	+	+	+	+	+	+	+	+	+	+	+	+	+	+	+	-	+	2	18	0.0%	1	64.2%
<u>23121.03 Å</u>																									
2/24/74	+	+	-	-	-	-	-	-	-	-	-	-	-	-	-	+	-	-	-	-	17	3	0.3%	0	100.0%
2/25/74	+	+	+	-	-	-	-	-	-	-	-	-	-	-	(-)	-	+	-	-	-	16	4	1.2%	1	64.2%
3/16/74	+	+	+	+	+	+	+	+	+	+	-	(-)	(-)	(-)	(-)	-	-	-	-	-	10	10	100.0%	4	1.6%
<u>23127.19 Å</u>																									
2/24/74	-	-	+	+	-	-	-	+	-	-	-	-	+	+	-	-	-	-	-	-	15	5	4.1%	0	100.0%
2/25/74	-	-	+	-	-	-	-	-	-	-	-	-	-	+	-	-	-	-	-	-	18	2	0.0%	0	100.0%
3/16/74	-	-	-	-	-	+	+	+	+	+	+	+	+	+	+	+	+	-	+	+	6	14	11.5%	0	100.0%
3/17/74	-	-	-	-	-	-	-	-	-	-	+	+	+	+	-	+	+	+	+	+	12	8	50.3%	0	100.0%
4/20/74	-	+	+	+	+	+	+	+	+	+	+	+	+	+	+	+	+	+	+	+	1	19	0.0%	1	64.2%
4/29/74	-	-	-	(-)	-	(-)	(-)	(-)	(-)	(-)	-	-	-	-	-	-	-	-	-	-	20	0	0.0%	6	0.0%

Table 4.2.--Continued Statistical test results from DRIFT1: sign of DELTA for scattered light measures.

Daily set	Position Index I																				N ₋	N ₊	α_{\pm}	N _t	α_t
	1	2	3	4	5	6	7	8	9	10	11	12	13	14	15	16	17	18	19	20					
<u>23132.73 Å</u>																									
3/17/74	+	+	+	-	-	-	-	-	-	-	+	-	-	-	-	-	-	-	-	-	16	4	1.2%	0	100.0%
4/20/74	-	-	-	-	-	-	-	-	-	-	+	-	+	+	+	+	+	+	+	+	11	9	82.4%	0	100.0%
4/21/74	+	(+)	(+)	+	+	(+)	(+)	+	+	+	+	-	-	-	-	-	-	-	+	-	8	12	50.3%	4	1.6%
4/22/74	-	+	+	-	-	+	+	+	+	+	+	+	-	-	-	-	-	-	-	-	11	9	82.4%	0	100.0%
4/29/74	-	-	-	-	-	-	+	+	+	+	+	+	+	+	+	-	-	(-)	-	-	11	9	82.4%	1	64.2%
4/30/74	+	-	-	-	-	+	-	+	+	+	+	(+)	(+)	(+)	+	+	(+)	+	+	+	5	15	4.1%	4	1.6%
<u>38839.36 Å</u>																									
5/12/74	-	-	+	-	-	-	-	-	-	-	+	-	+	+	-	-	-	+	+	+	13	7	26.3%	0	100.0%
5/14/74	(-)	(-)	(-)	(-)	(-)	(-)	(-)	-	(-)	(-)	-	-	-	-	-	-	-	-	-	(-)	20	0	0.0%	10	0.0%
5/15/74	(-)	-	-	-	-	-	-	-	-	-	-	-	-	-	-	-	+	-	+	-	18	2	0.0%	1	64.2%
<u>38862.02 Å</u>																									
5/12/74	+	+	+	-	-	-	-	-	(-)	-	-	-	-	(-)	-	-	-	-	-	(-)	17	3	0.3%	3	7.6%
5/14/74	+	-	+	-	+	+	-	-	-	-	-	-	-	-	-	-	-	-	-	-	16	4	1.2%	0	100.0%
5/15/74	+	-	-	-	+	+	-	-	-	-	-	-	-	(-)	(-)	-	-	-	-	-	17	3	0.3%	2	26.4%
<u>45908.50 Å</u>																									
5/21/74	+	+	+	+	-	-	-	-	-	+	+	+	-	-	-	-	-	-	-	-	13	7	26.3%	0	100.0%
5/24/74	+	-	-	-	-	+	-	-	-	-	-	+	-	+	+	+	+	+	+	+	10	10	100.0%	0	100.0%
5/25/74	-	-	-	-	-	-	-	-	-	-	-	-	-	-	+	-	-	-	-	-	19	1	0.0%	0	100.0%
<u>46142.57 Å</u>																									
5/21/74	+	+	+	+	+	+	+	(+)	(+)	(+)	+	+	+	+	-	-	-	-	-	-	6	14	11.5%	3	7.6%
5/24/74	-	-	-	-	-	-	-	-	+	+	+	+	+	+	+	+	+	+	+	+	9	11	82.4%	0	100.0%
5/25/74	-	-	+	+	+	+	+	+	+	+	+	-	-	+	-	-	-	-	-	-	10	10	100.0%	0	100.0%
<u>85636.32 Å</u>																									
5/20/74	-	-	-	-	-	-	-	(-)	-	-	+	-	-	+	-	+	+	+	-	-	15	5	4.1%	1	64.2%
5/25/74	(-)	(-)	(-)	-	-	-	-	+	+	-	-	-	-	+	-	+	+	+	+	-	13	7	26.3%	3	7.6%
5/26/74	-	-	-	-	-	-	-	-	+	-	+	+	+	+	-	+	-	-	+	+	12	8	50.3%	0	100.0%
<u>104007.55 Å</u>																									
5/20/74	-	-	-	-	-	-	-	-	-	(-)	-	+	+	+	-	+	-	-	-	+	15	5	4.1%	1	64.2%
5/25/74	-	(-)	(-)	-	-	-	+	-	-	-	-	-	-	+	-	-	-	+	-	(-)	17	3	0.3%	3	7.6%
5/26/74	(-)	-	-	-	(-)	-	-	-	-	+	-	-	-	-	-	+	+	+	-	-	16	4	1.2%	2	26.4%

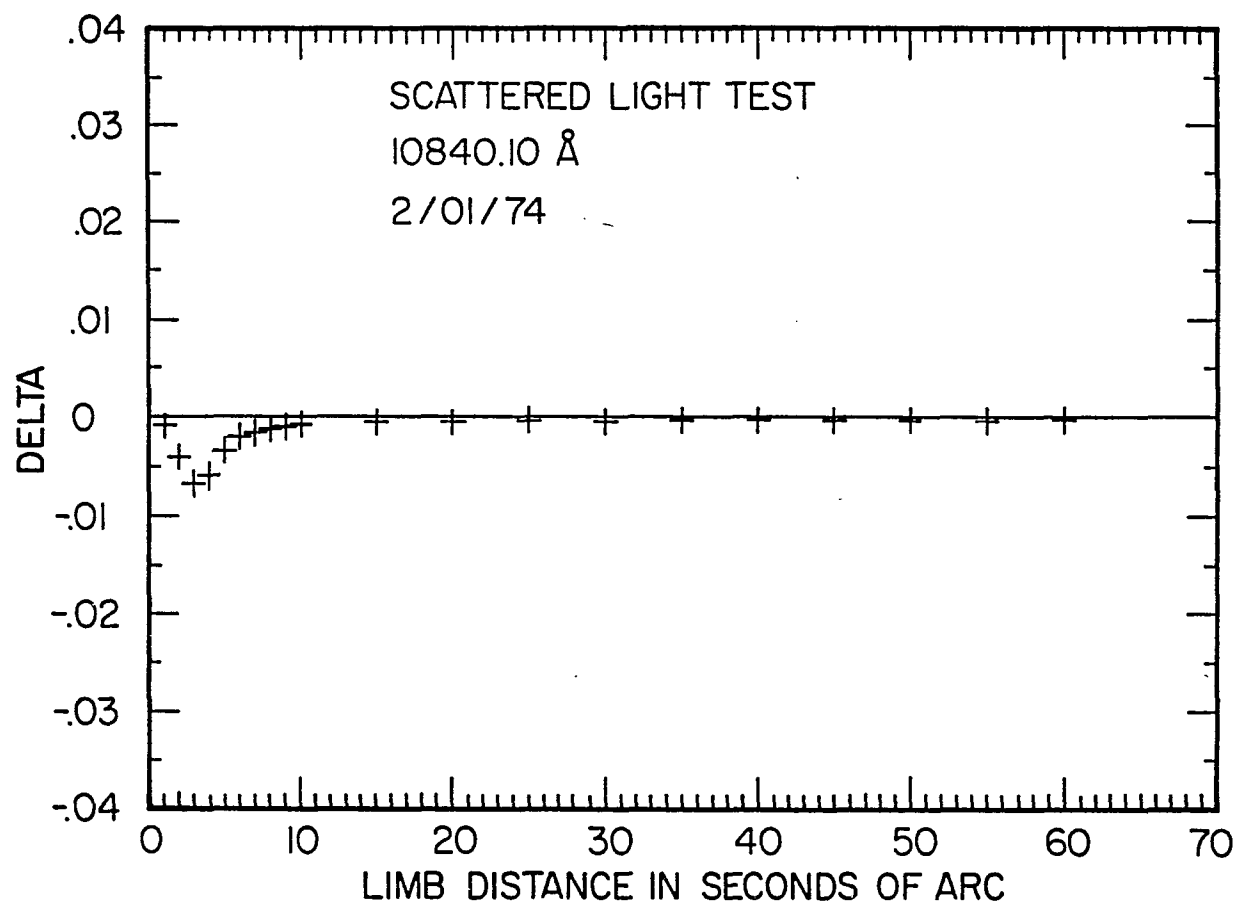


Figure 4.5. Values of DELTA for scattered light measures at 10840.10 Å on February 1, 1974.

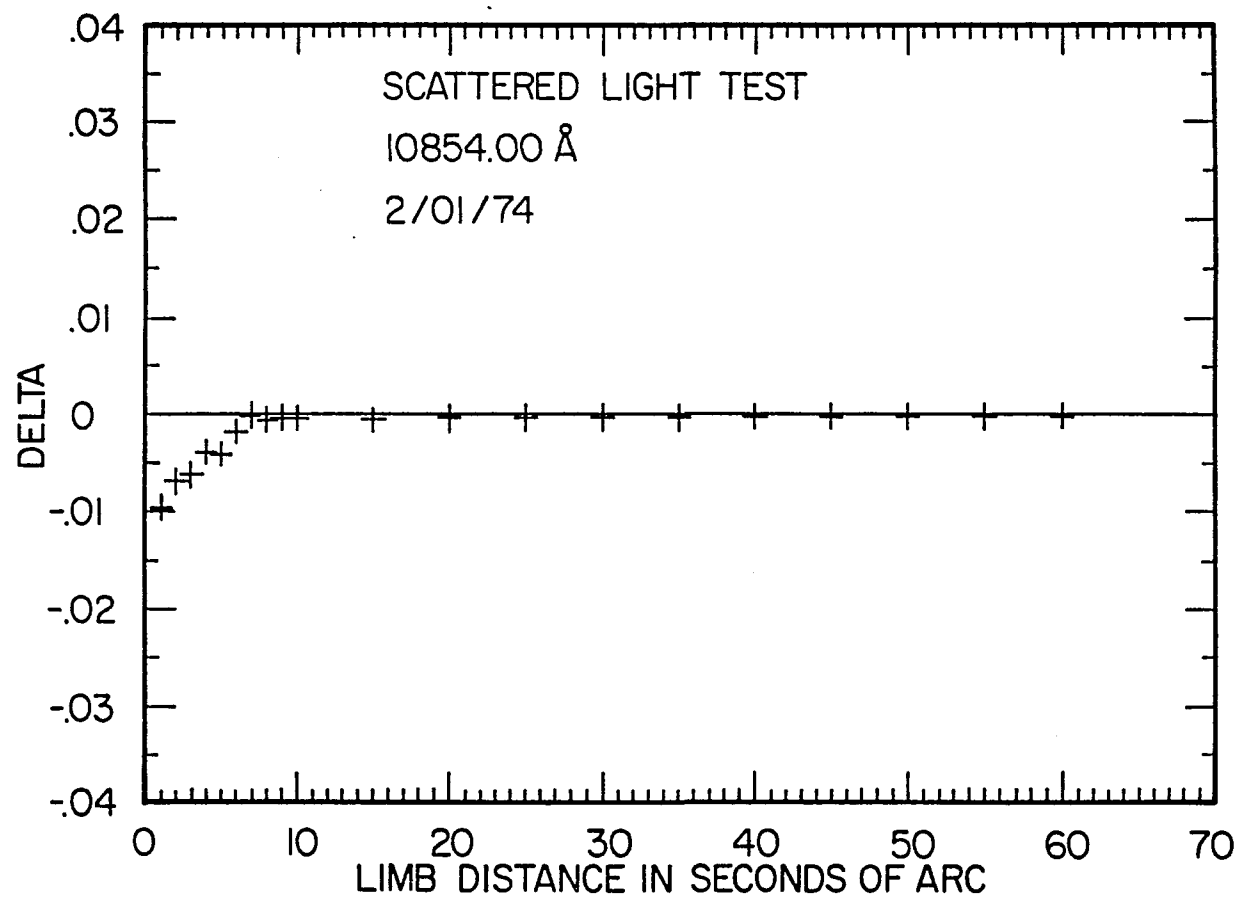


Figure 4.6. Values of DELTA for scattered light measures at 10854.00 Å on February 1, 1974.

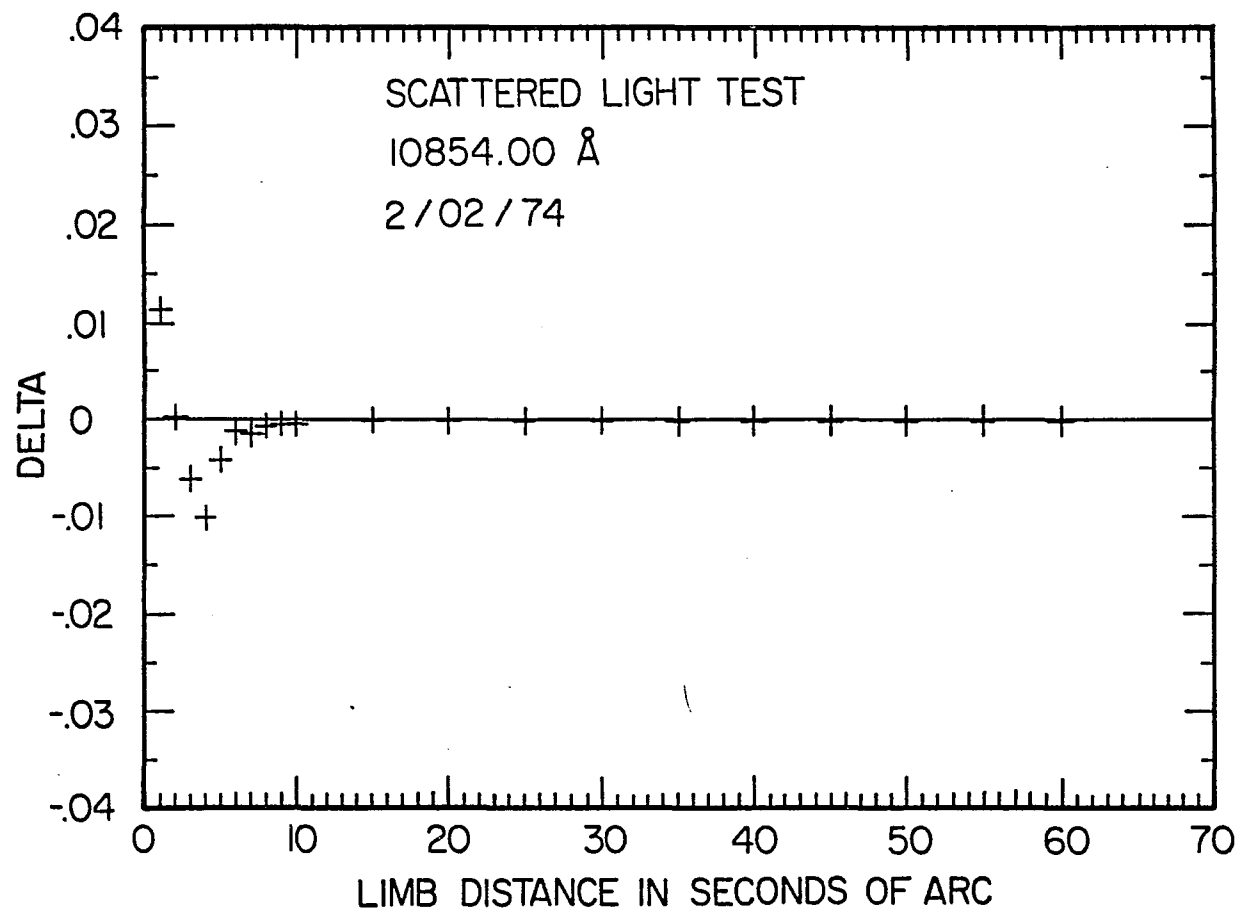


Figure 4.7. Values of DELTA for scattered light measures at 10854.00 Å on February 2, 1974.

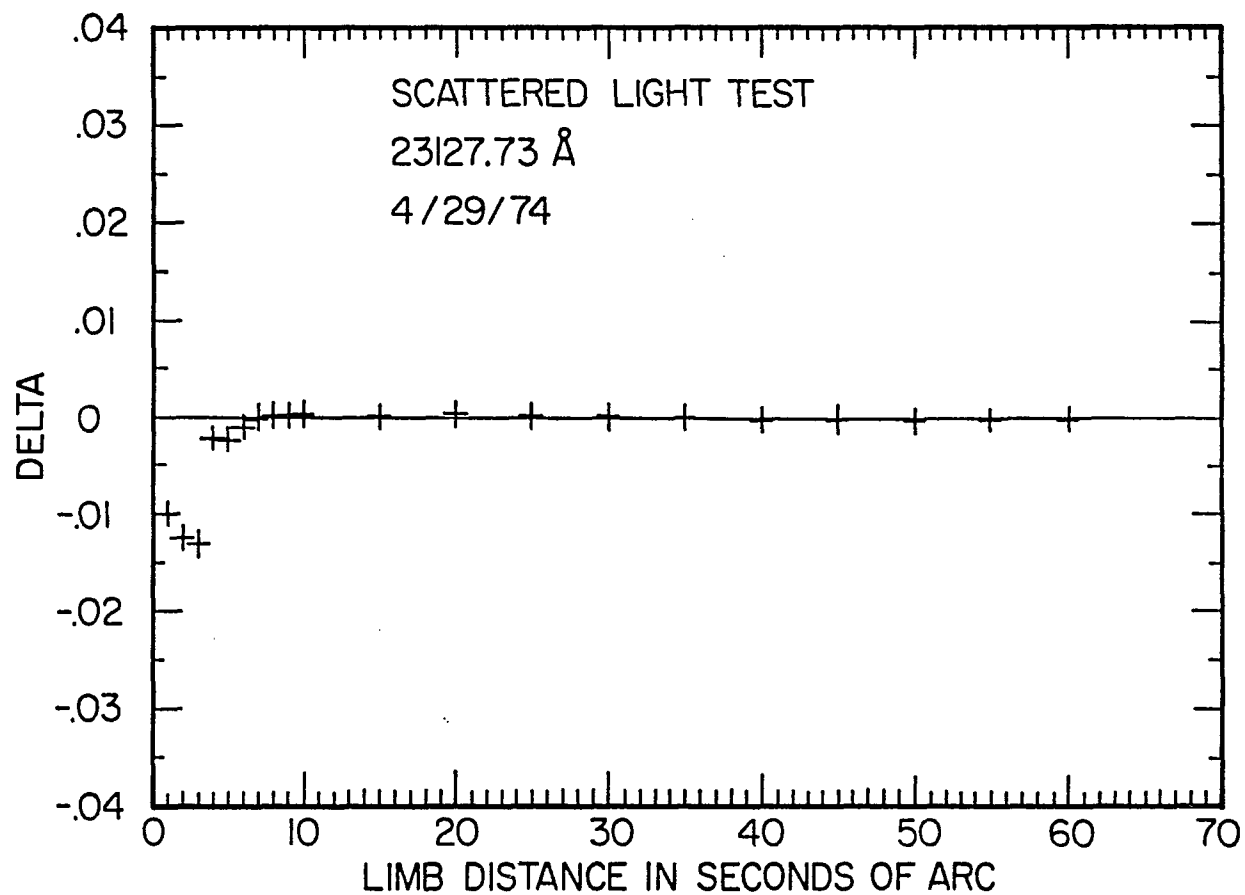


Figure 4.8. Values of DELTA for scattered light measures at 23127.73 Å on April 29, 1974.

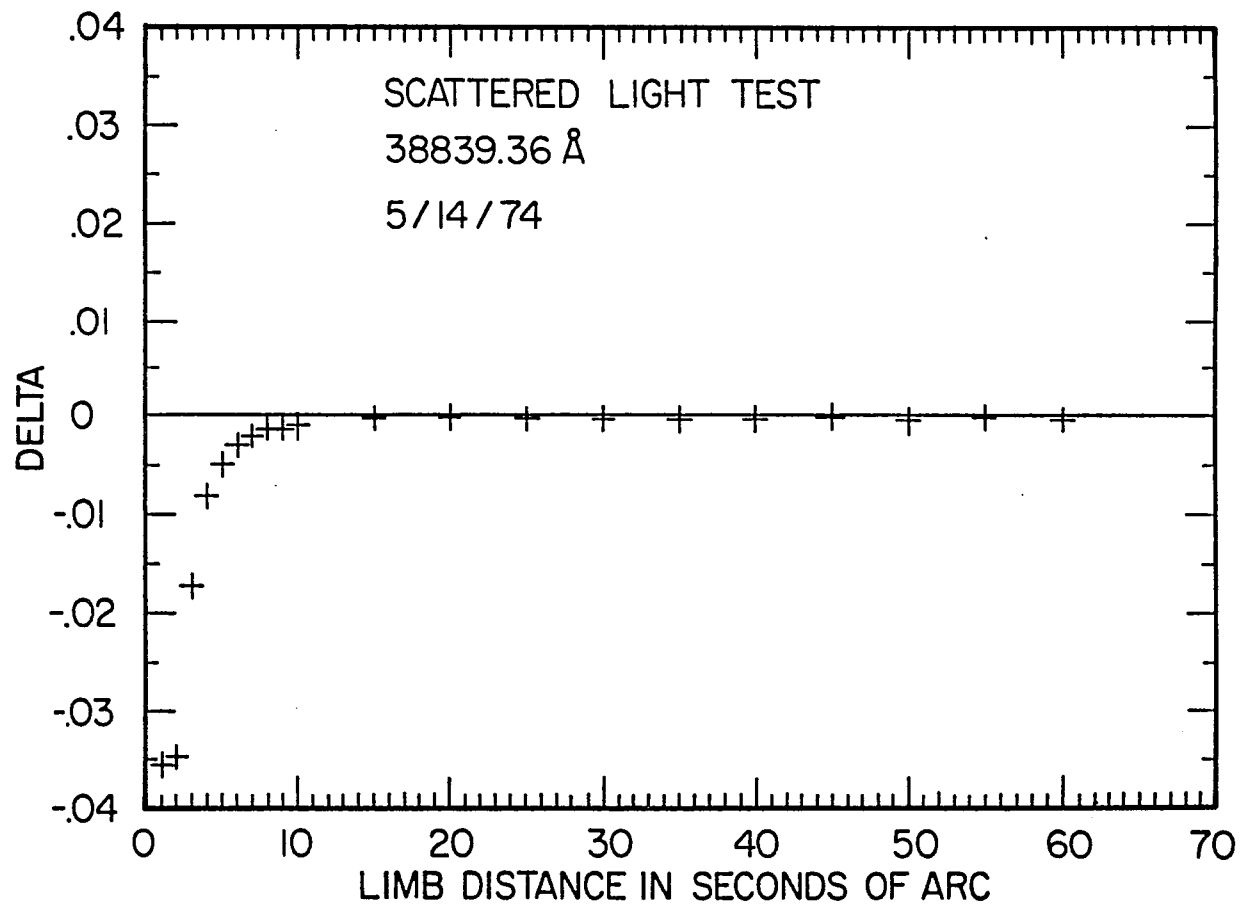


Figure 4.9. Values of DELTA for scattered light measures at 38839.36 Å on May 14, 1974.

instrumental zero. Since the residual errors in the background subtraction procedure generally seem to be less than ± 0.0005 , they should have a negligible effect on the limb darkening measures.

Several conclusions may be drawn from the results of the statistical tests in DRIFT1. Since the scattered light measures appear to be more or less the same off opposite limbs of the sun, one can assume that the background was relatively constant for each scan and that the smearing functions for scattering, seeing, and instrumental diffraction were nearly symmetric. The fact that the limb darkening measures are generally the same on opposite limbs of the sun also demonstrates that the instrumental gain was constant during each scan.

4.2 Statistical Results from DRIFT2

The Student's test in DRIFT2 checked the statistical hypothesis that the limb darkening was the same on all days at each wavelength. The sign of DELTAP is listed at each limb position for every daily set in Table 4.3. Parentheses signify that the absolute value of T was greater than the fractile of the Student's distribution that corresponded to a 5% level of significance in the test. A zero in place of a sign indicates that the measure was deleted because of a sunspot.

Table 4.3. Statistical test results from DRIFT2: sign of DELTAP for limb darkening measures.

Daily set	Position Index I																				N ₋	N ₊	α_{\pm}	N _t	α_t
	1	2	3	4	5	6	7	8	9	10	11	12	13	14	15	16	17	18	19	20					
<u>10840.10 Å</u>																									
1/31/74	+	+	+	+	+	(+)	-	+	-	+	-	+	+	(+)	+	-	(-)	(-)	(-)		7	13	26.3%	5	0.3%
2/01/74	-	-	+	+	-	(-)	-	+	-	-	(-)	-	-	(-)	-	+	(+)	+	+		13	7	26.3%	4	1.6%
2/02/74	+	+	-	-	-	+	(+)	-	+	-	+	+	+	-	+	-	+	+	+	+	7	13	26.3%	1	64.2%
<u>10854.00 Å</u>																									
2/01/74	+	+	-	(+)	-	-	-	-	(-)	+	-	-	-	+	+	-	-	-	-	-	14	6	11.5%	2	26.4%
2/02/74	+	+	+	-	+	-	+	+	+	+	+	+	+	-	-	+	+	+	+	+	4	16	1.2%	0	100.0%
2/02/74	-	-	+	-	-	(+)	+	-	+	-	+	-	+	+	+	-	-	-	+	+	9	11	82.4%	1	64.2%
<u>10865.00 Å</u>																									
1/31/74	-	-	-	-	-	-	-	+	(-)	(+)	(-)	-	+	(-)	-	+	+	+	+	+	12	8	50.3%	4	1.6%
2/01/74	-	-	-	-	-	(-)	-	-	-	+	-	(-)	+	-	-	+	+	+	+	+	14	6	11.5%	2	26.4%
2/02/74	+	+	+	+	+	(+)	+	+	(+)	-	+	+	+	(+)	+	-	(-)	(-)	(-)		5	15	4.1%	6	0.0%
<u>12466.63 Å</u>																									
2/16/74	-	-	-	-	+	-	+	+	-	-	(-)	-	+	-	-	+	+	-	-	-	14	6	11.5%	1	64.2%
4/21/74	-	-	-	-	+	+	+	(+)	+	+	-	-	-	-	-	-	-	-	(-)	(-)	14	6	11.5%	3	7.6%
4/22/74	-	+	+	+	+	-	-	+	-	-	-	-	+	+	+	+	+	+	+	+	8	12	50.3%	0	100.0%
4/29/74	+	(+)	+	+	+	(+)	+	+	+	+	+	+	+	+	-	-	-	+	+	-	4	16	1.2%	2	26.4%
4/30/74	+	-	-	+	-	-	-	-	-	-	(+)	+	-	+	+	+	+	+	+	(+)	9	11	82.4%	2	26.4%
<u>12505.51 Å</u>																									
2/16/74	-	+	-	+	+	+	+	-	+	+	(-)	-	-	-	+	+	+	+	-	-	9	11	82.4%	1	64.2%
4/21/74	-	-	+	-	+	-	-	-	+	+	+	+	-	-	-	-	(-)	(-)	(-)	(-)	14	6	11.5%	4	1.6%
4/22/74	+	+	+	+	+	-	+	-	-	-	(-)	-	-	-	-	-	+	+	+	+	11	9	82.4%	1	64.2%
4/29/74	+	+	+	-	+	(+)	(+)	+	-	+	+	+	+	+	+	-	-	-	-	-	5	14	11.5%	2	26.4%
4/30/74	-	-	-	+	-	(-)	-	+	-	-	(+)	-	-	+	+	+	+	+	+	+	10	10	100.0%	2	26.4%
<u>16222.00 Å</u>																									
2/15/74	-	-	0	+	+	+	-	+	+	+	+	+	(+)	(+)	+	-	+	-	-	-	7	12	16.7%	2	24.5%
2/24/74	-	-	-	+	+	-	-	+	-	-	-	-	+	-	+	+	+	-	-	-	13	7	26.3%	0	100.0%
2/26/74	-	-	+	+	+	-	-	-	+	+	-	-	+	+	+	-	-	+	+	+	10	10	100.0%	0	100.0%
3/16/74	-	+	-	-	-	+	-	+	-	+	-	-	-	-	(-)	(-)	(-)	(-)	(-)	(-)	16	4	1.2%	6	0.0%
4/20/74	+	-	+	+	-	+	+	+	-	+	+	+	+	+	+	+	+	+	(+)	+	5	15	4.1%	1	64.2%
4/21/74	-	+	-	-	-	+	+	+	+	+	+	+	-	+	+	+	+	+	+	+	9	11	82.4%	0	100.0%
4/28/74	+	-	-	-	-	+	+	-	-	-	+	-	+	+	+	+	+	+	+	+	8	12	50.3%	0	100.0%
4/29/74	+	+	+	-	+	-	-	-	-	-	-	+	-	-	-	-	+	-	-	-	14	6	11.5%	0	100.0%

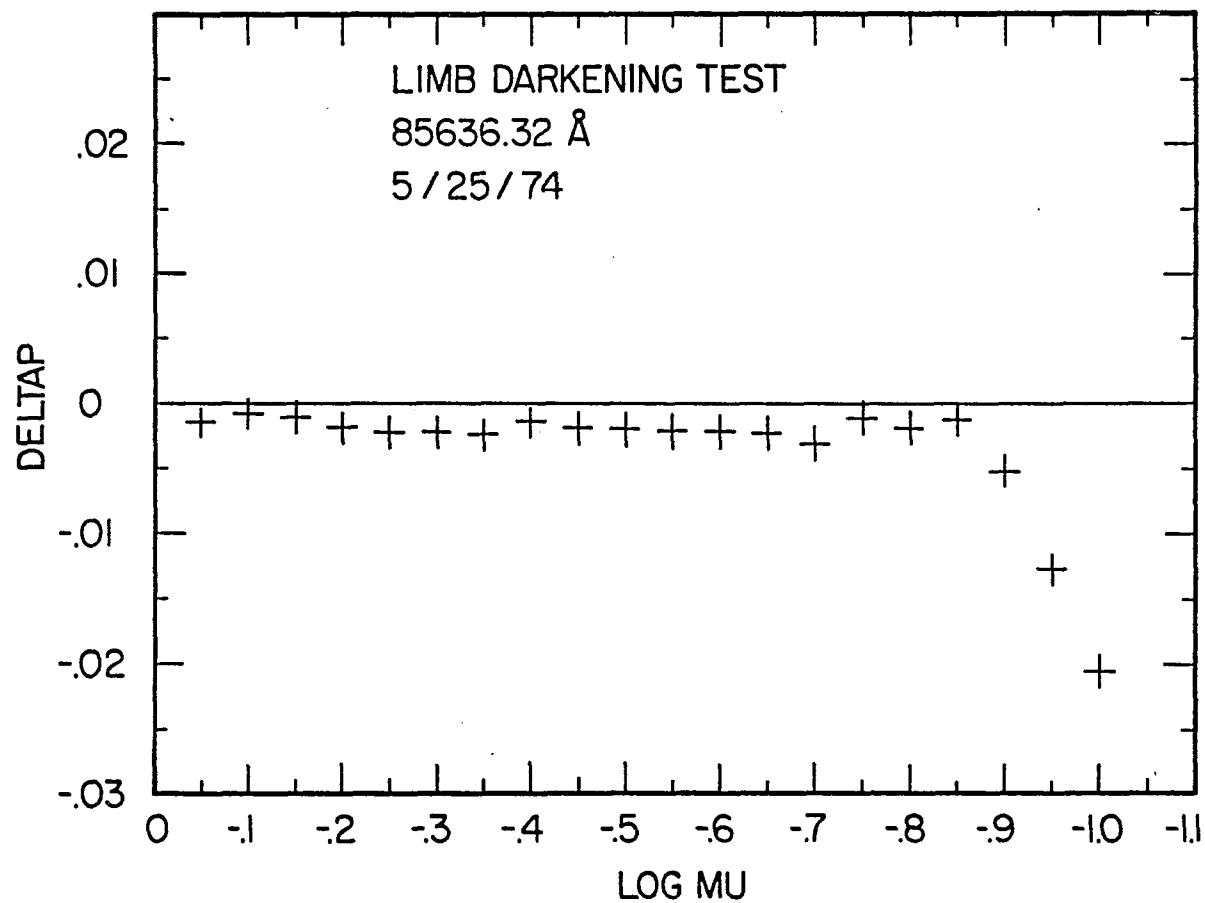
Table 4.3.--Continued Statistical test results from DRIFT2: sign of DELTAP for limb darkening measures.

Daily set	Position Index I																				N ₋	N ₊	α_{\pm}	N _t	α_t
	1	2	3	4	5	6	7	8	9	10	11	12	13	14	15	16	17	18	19	20					
<u>16513.18 Å</u>																									
2/15/74	-	-	0	+	+	-	(-)	-	-	-	+	+	+	+	+	+	+	-	-	-	10	9	100.0%	1	62.3%
2/24/74	+	+	+	-	+	+	+	+	-	-	-	+	+	+	+	+	(+)	(+)	(+)	(+)	3	17	0.3%	4	1.6%
2/25/74	-	-	-	+	+	+	+	(-)	-	(-)	-	-	-	+	+	+	+	+	+	(+)	10	10	100.0%	3	7.6%
2/26/74	+	+	+	+	+	+	+	+	+	+	+	+	+	+	+	+	+	+	+	+	1	19	0.0%	0	100.0%
3/16/74	-	-	+	+	+	+	+	+	+	+	+	+	+	-	-	-	-	-	-	-	9	11	82.4%	0	100.0%
4/20/74	(-)	(-)	(-)	(-)	-	-	-	(-)	(-)	-	-	-	-	-	-	-	-	-	-	-	20	0	0.0%	6	0.0%
4/21/74	+	-	+	-	-	+	-	+	+	+	+	+	-	+	+	-	-	-	-	-	10	10	100.0%	0	100.0%
4/28/74	+	+	+	+	+	+	+	+	+	+	-	+	+	+	-	-	-	-	-	-	8	12	50.3%	0	100.0%
4/29/74	+	+	-	-	-	-	+	+	+	-	-	-	-	(-)	(-)	-	-	-	-	-	5	15	4.1%	2	26.4%
<u>21855.59 Å</u>																									
2/24/74	-	-	-	-	-	-	-	-	-	+	+	+	+	+	-	-	-	-	+	+	18	2	0.0%	0	100.0%
4/21/74	+	+	+	-	-	+	-	+	+	+	+	+	+	+	-	-	-	-	-	-	9	11	82.4%	0	100.0%
4/28/74	-	-	-	+	+	-	-	+	+	-	-	-	+	+	-	+	+	+	+	+	9	11	82.4%	0	100.0%
4/29/74	+	+	+	-	+	+	+	+	+	-	-	-	-	-	+	+	+	+	+	-	9	11	82.4%	0	100.0%
<u>21907.47 Å</u>																									
2/24/74	+	+	+	-	+	+	+	-	+	+	+	-	+	+	+	+	+	+	+	+	3	17	0.3%	0	100.0%
3/17/74	+	+	+	-	-	-	-	-	-	+	+	+	-	(-)	(-)	(-)	(-)	(-)	(-)	(-)	14	6	11.5%	7	0.0%
4/20/74	-	-	-	-	-	+	-	+	-	-	-	+	-	+	+	+	+	(+)	(+)	(+)	10	10	100.0%	3	7.6%
4/21/74	-	+	-	-	-	-	-	+	+	-	-	-	-	+	+	+	+	+	+	+	10	10	100.0%	0	100.0%
4/28/74	+	+	-	(+)	+	+	+	+	+	+	(+)	-	+	+	+	+	-	+	+	+	3	17	0.3%	2	26.4%
4/29/74	-	(-)	-	+	-	+	+	-	-	-	-	+	-	-	-	-	-	-	-	-	16	4	1.2%	1	64.2%
<u>23121.03 Å</u>																									
2/24/74	+	+	+	-	+	+	+	-	+	-	-	-	-	+	-	-	+	+	+	+	8	12	50.3%	0	100.0%
2/25/74	+	+	+	+	+	+	-	(+)	-	+	+	+	+	+	+	+	-	+	+	+	3	17	0.3%	1	64.2%
3/16/74	-	-	-	+	-	(-)	-	+	+	-	-	-	-	-	-	-	-	-	-	-	17	3	0.3%	1	64.2%
<u>23127.19 Å</u>																									
2/24/74	+	+	+	+	+	+	+	(+)	+	+	+	+	(+)	(+)	(+)	(+)	+	+	+	+	0	20	0.0%	5	0.3%
2/25/74	-	-	-	-	+	-	-	+	(-)	-	-	-	+	+	-	-	+	+	+	+	12	8	50.3%	1	64.2%
3/16/74	+	+	+	+	-	-	-	+	-	-	-	-	-	-	(-)	(-)	(-)	-	-	-	15	5	4.1%	3	7.6%
3/17/74	+	-	+	-	+	-	-	+	-	-	+	+	-	-	+	+	+	+	+	+	13	7	26.3%	0	100.0%
4/20/74	-	-	+	+	-	-	+	+	+	+	+	+	+	+	+	+	+	+	+	+	7	13	26.3%	0	100.0%
4/29/74	+	-	-	+	+	+	+	(-)	-	+	+	+	-	-	-	-	-	-	-	+	13	7	26.3%	1	64.2%

Table 4.3.--Continued Statistical test results from DRIFT2: sign of DELTAP for limb darkening measures.

Daily set	Position Index I																				N ₋	N ₊	α_{\pm}	N _t	α_t
	1	2	3	4	5	6	7	8	9	10	11	12	13	14	15	16	17	18	19	20					
<u>23132.73 Å</u>																									
3/17/74	-	+	+	-	-	+	+	+	+	+	+	+	-	+	+	+	-	-	-	-	8	12	50.3%	0	100.0%
4/20/74	-	-	-	-	+	-	-	(-)	-	-	+	-	+	+	+	+	(+)	+	+	+	10	10	100.0%	2	26.4%
4/21/74	-	-	-	+	-	-	-	-	+	(-)	(-)	+	-	(-)	(-)	(-)	-	-	(-)	(-)	17	3	0.3%	7	0.0%
4/22/74	-	-	-	-	-	-	-	+	-	-	-	-	-	-	-	-	+	+	-	-	17	3	0.3%	0	100.0%
4/29/74	+	+	+	-	-	+	+	+	+	-	+	+	+	+	+	-	-	+	+	+	5	15	4.1%	0	100.0%
4/30/74	+	+	+	+	+	+	+	+	+	(+)	+	+	+	+	+	-	-	+	+	+	2	18	0.0%	1	64.2%
<u>38839.36 Å</u>																									
5/12/74	-	-	-	-	-	-	0	0	+	+	+	+	+	+	+	+	+	+	(+)	(+)	6	12	23.8%	2	22.7%
5/14/74	+	+	+	+	+	+	-	+	-	-	-	-	-	+	+	+	-	-	-	-	10	10	100.0%	0	100.0%
5/15/74	0	-	+	-	-	+	+	-	+	+	-	-	-	-	-	-	-	-	-	-	14	5	6.4%	0	100.0%
<u>38862.02 Å</u>																									
5/12/74	+	+	+	+	+	+	0	0	+	-	+	+	+	+	+	+	+	+	+	+	1	17	0.0%	0	100.0%
5/14/74	-	-	-	-	+	-	-	-	(-)	+	-	-	-	-	-	-	-	-	(-)	(-)	18	2	0.0%	3	7.6%
5/15/74	0	-	+	+	-	-	+	+	+	+	-	-	-	+	-	-	-	+	+	+	9	10	100.0%	0	100.0%
<u>45908.50 Å</u>																									
5/21/74	-	-	+	+	-	(-)	-	-	-	-	-	-	(-)	-	-	-	-	-	(-)	-	18	2	0.0%	3	7.6%
5/24/74	-	-	-	+	-	+	+	+	+	+	+	+	+	-	(+)	+	+	+	(+)	(+)	5	15	4.1%	3	7.6%
5/25/74	(+)	+	-	-	+	+	+	-	-	+	-	-	+	+	-	-	-	-	-	-	12	8	50.3%	1	64.2%
<u>46142.57 Å</u>																									
5/21/74	-	-	-	+	+	-	-	+	-	-	-	-	-	-	+	-	-	+	+	+	13	7	26.3%	0	100.0%
5/24/74	+	+	+	-	-	+	+	-	-	+	-	-	-	-	-	+	+	(+)	(+)	(+)	9	11	82.4%	3	7.6%
5/25/74	+	+	+	-	+	+	+	+	+	+	+	+	+	+	+	+	-	-	-	-	5	15	4.1%	0	100.0%
<u>85636.32 Å</u>																									
5/20/74	(+)	(+)	(+)	(+)	(+)	+	+	+	(+)	+	+	+	+	+	-	-	(-)	-	+	+	4	16	1.2%	7	0.0%
5/25/74	(-)	-	-	(-)	(-)	(-)	(-)	-	(-)	(-)	-	(-)	(-)	(-)	-	-	-	-	-	-	20	0	0.0%	10	0.0%
5/26/74	0	-	-	-	-	+	+	+	+	+	+	+	+	+	+	(+)	(+)	+	+	+	4	15	1.9%	2	24.5%
<u>104007.55 Å</u>																									
5/20/74	+	+	+	+	+	-	-	-	+	+	+	-	-	-	-	-	-	(-)	-	-	12	8	50.3%	1	64.2%
5/25/74	-	-	-	-	(-)	-	(-)	(-)	-	-	+	+	+	+	+	+	+	+	(+)	+	12	8	50.3%	4	1.6%
5/26/74	0	+	+	-	+	+	(+)	(+)	+	+	-	-	-	+	+	+	+	+	-	-	6	13	16.7%	2	24.5%

Substantially fewer DELTAP of one sign or the other in a daily set would indicate that the limb darkening measures being tested were systematically different from the measures taken on other days at the same wavelength. The hypothesis that a positive or negative value of DELTAP was equally likely at each limb position was therefore tested in each daily set. The strictest significance level for which the test would fail was computed in the same manner as it was for the statistical test results from DRIFT1. The hypothesis that DELTAP had a 5% probability of failing the Student's test was also checked in each daily set. The computed values of α_{\pm} and α_T are included in Table 4.3. An examination of the test results shows that most of the limb darkening measures agree fairly well from day to day. The values of DELTAP for two daily sets that appear to deviate somewhat more than expected from the other sets at the same wavelength are presented graphically in Figures 4.10 and 4.11. Since the variations in the limb darkening measures from one scan to another were generally as large as those from day to day, it was appropriate to average together the results from all of the drift scans at each wavelength without applying any additional weights to the data.



CHAPTER 5

THE FINAL RESULTS OF THE OBSERVATIONS

Final observational limb darkening measures were calculated in the reduction program DRIFT2. A quadratic fit to these limb darkening measures was also made at each observational wavelength. These fits were restricted to $\log \mu$ values between 0.00 and -0.70 in order to avoid systematic errors near the limb. The coefficients for these quadratic fits and the final limb darkening measures are tabulated in Section 5.1. Systematic errors caused by variations in the solar declination are considered in Section 5.2. A discussion of the uncertainties in the $\log \mu$ positions of the limb darkening measures is given in Section 5.3. The effects of atmospheric scattering, atmospheric seeing, and instrumental diffraction are then described in Section 5.4. Errors produced by variations in the instrumental gain and zero are considered in Section 5.5. Since all of the observational errors were found to be quite small, no systematic corrections were applied to the final limb darkening measures.

5.1 Final Results of the Limb Darkening Observations

The final limb darkening measures are presented in Tables 5.1 to 5.18. The limb darkening measures in these

Table 5.1. Limb darkening results for 10840.10 Å

Log μ	Measured limb darkening	Standard deviation	Number of scans	Fitted limb darkening
-.00	1.00000	.00000	36	.99894
-.05	.96910	.00248	36	.96902
-.10	.94020	.00217	36	.94028
-.15	.91199	.00282	36	.91272
-.20	.88559	.00260	36	.88635
-.25	.85989	.00242	36	.86117
-.30	.83731	.00223	36	.83716
-.35	.81404	.00266	36	.81435
-.40	.79348	.00282	36	.79272
-.45	.77341	.00367	36	.77227
-.50	.75314	.00272	36	.75301
-.55	.73544	.00308	36	.73494
-.60	.71855	.00290	36	.71805
-.65	.70233	.00350	36	.70234
-.70	.68668	.00286	36	.68782

Table 5.2. Limb darkening results for 10854.00 Å

Log μ	Measured limb darkening	Standard deviation	Number of scans	Fitted limb darkening
-.00	1.00000	.00000	35	.99915
-.05	.96972	.00265	35	.96928
-.10	.94019	.00302	35	.94059
-.15	.91250	.00261	35	.91307
-.20	.88600	.00234	35	.88674
-.25	.86040	.00260	35	.86158
-.30	.83756	.00260	35	.83760
-.35	.81530	.00314	35	.81480
-.40	.79269	.00307	35	.79317
-.45	.77372	.00280	35	.77273
-.50	.75531	.00266	35	.75346
-.55	.73467	.00253	35	.73537
-.60	.71888	.00256	35	.71845
-.65	.70268	.00335	35	.70271
-.70	.68722	.00313	35	.68816

Table 5.3. Limb darkening results for 10865.00 Å

Log μ	Measured limb darkening	Standard deviation	Number of scans	Fitted limb darkening
-.00	1.00000	.00000	36	.99920
-.05	.96957	.00210	36	.96942
-.10	.94091	.00293	36	.94081
-.15	.91259	.00276	36	.91338
-.20	.88624	.00326	36	.88712
-.25	.86132	.00344	36	.86204
-.30	.83834	.00267	36	.83813
-.35	.81504	.00329	36	.81539
-.40	.79418	.00271	36	.79383
-.45	.77465	.00265	36	.77345
-.50	.75404	.00285	36	.75424
-.55	.73682	.00251	36	.73620
-.60	.71980	.00291	36	.71934
-.65	.70379	.00328	36	.70366
-.70	.68805	.00289	36	.68915

Table 5.4. Limb darkening results for 12466.63 Å

Log μ	Measured limb darkening	Standard deviation	Number of scans	Fitted limb darkening
-.00	1.00000	.00000	60	.99952
-.05	.97266	.00209	60	.97258
-.10	.94629	.00248	60	.94659
-.15	.92090	.00259	60	.92154
-.20	.89769	.00250	60	.89744
-.25	.87407	.00256	60	.87428
-.30	.85193	.00302	60	.85206
-.35	.83078	.00250	60	.83078
-.40	.81062	.00236	60	.81045
-.45	.79132	.00265	60	.79106
-.50	.77270	.00299	60	.77261
-.55	.75497	.00326	60	.75511
-.60	.73878	.00328	60	.73855
-.65	.72363	.00331	60	.72293
-.70	.70742	.00340	60	.70825

Table 5.5. Limb darkening results for 12505.51 Å

Log μ	Measured limb darkening	Standard deviation	Number of scans	Fitted limb darkening
-.00	1.00000	.00000	60	.99949
-.05	.97246	.00205	60	.97251
-.10	.94677	.00217	60	.94649
-.15	.92104	.00250	60	.92143
-.20	.89711	.00259	60	.89732
-.25	.87320	.00251	60	.87417
-.30	.85191	.00231	60	.85197
-.35	.83060	.00233	60	.83073
-.40	.81047	.00274	60	.81045
-.45	.79165	.00280	60	.79112
-.50	.77284	.00279	60	.77275
-.55	.75626	.00251	60	.75533
-.60	.73932	.00259	60	.73887
-.65	.72324	.00310	60	.72336
-.70	.70793	.00330	60	.70881

Table 5.6. Limb darkening results for 16222.00 Å

Log μ	Measured limb darkening	Standard deviation	Number of scans	Fitted limb darkening
-.00	1.00000	.00000	93	.99979
-.05	.98104	.00178	93	.98099
-.10	.96253	.00190	93	.96258
-.15	.94437	.00227	93	.94455
-.20	.92684	.00202	93	.92691
-.25	.90928	.00204	93	.90965
-.30	.89278	.00186	93	.89278
-.35	.87653	.00238	93	.87630
-.40	.86008	.00198	93	.86020
-.45	.84463	.00226	93	.84449
-.50	.82939	.00220	93	.82916
-.55	.81415	.00248	93	.81422
-.60	.79991	.00240	93	.79967
-.65	.78558	.00282	93	.78551
-.70	.77140	.00305	93	.77173

Table 5.7. Limb darkening results for 16513.18 Å

Log μ	Measured limb darkening	Standard deviation	Number of scans	Fitted limb darkening
-.00	1.00000	.00000	104	.99974
-.05	.98128	.00144	104	.98130
-.10	.96332	.00163	104	.96325
-.15	.94538	.00171	93	.94558
-.20	.92810	.00190	104	.92829
-.25	.91122	.00210	104	.91138
-.30	.89477	.00194	104	.89486
-.35	.87859	.00197	104	.87872
-.40	.86285	.00213	104	.86296
-.45	.84770	.00208	104	.84759
-.50	.83297	.00228	104	.83260
-.55	.81830	.00227	104	.81799
-.60	.80406	.00266	104	.80377
-.65	.78981	.00271	104	.78993
-.70	.77606	.00302	104	.77647

Table 5.8. Limb darkening results for 21855.59 Å

Log μ	Measured limb darkening	Standard deviation	Number of scans	Fitted limb darkening
-.00	1.00000	.00000	47	.99988
-.05	.98374	.00155	47	.98364
-.10	.96769	.00179	47	.96774
-.15	.95204	.00180	47	.95221
-.20	.93678	.00168	47	.93703
-.25	.92257	.00197	47	.92221
-.30	.90755	.00218	47	.90775
-.35	.89352	.00221	47	.89365
-.40	.87973	.00212	47	.87990
-.45	.86669	.00220	47	.86651
-.50	.85379	.00230	47	.85347
-.55	.84065	.00247	47	.84079
-.60	.82865	.00223	47	.82847
-.65	.81672	.00242	47	.81651
-.70	.80454	.00271	47	.80490

Table 5.9. Limb darkening results for 21907.47 Å

Log μ	Measured limb darkening	Standard deviation	Number of scans	Fitted limb darkening
-.00	1.00000	.00000	71	.99971
-.05	.98325	.00132	71	.98334
-.10	.96733	.00154	71	.96735
-.15	.95166	.00157	71	.95174
-.20	.93637	.00163	71	.93651
-.25	.92145	.00179	71	.92166
-.30	.90698	.00186	71	.90718
-.35	.89318	.00188	71	.89309
-.40	.87947	.00179	71	.87938
-.45	.86612	.00194	71	.86605
-.50	.85328	.00210	71	.85309
-.55	.84079	.00201	71	.84052
-.60	.82836	.00213	71	.82833
-.65	.81650	.00215	71	.81651
-.70	.80480	.00266	71	.80508

Table 5.10. Limb darkening results for 23121.03 Å

Log μ	Measured limb darkening	Standard deviation	Number of scans	Fitted limb darkening
-.00	1.00000	.00000	36	.99992
-.05	.98398	.00183	36	.98390
-.10	.96816	.00190	36	.96828
-.15	.95286	.00207	36	.95304
-.20	.93822	.00200	36	.93819
-.25	.92378	.00215	36	.92373
-.30	.90953	.00221	36	.90966
-.35	.89633	.00182	36	.89598
-.40	.88247	.00198	36	.88269
-.45	.86998	.00218	36	.86979
-.50	.85722	.00219	36	.85727
-.55	.84528	.00223	36	.84515
-.60	.83298	.00250	36	.83341
-.65	.82235	.00254	36	.82207
-.70	.81105	.00280	36	.81111

Table 5.11. Limb darkening results for 23127.19 Å

Log μ	Measured limb darkening	Standard deviation	Number of scans	Fitted limb darkening
-.00	1.00000	.00000	70	.99980
-.05	.98393	.00192	70	.98393
-.10	.96852	.00205	70	.96842
-.15	.95313	.00225	70	.95329
-.20	.93837	.00208	70	.93853
-.25	.92381	.00217	70	.92413
-.30	.91025	.00230	70	.91010
-.35	.89602	.00249	70	.89644
-.40	.88340	.00224	70	.88316
-.45	.87037	.00224	70	.87024
-.50	.85792	.00260	70	.85768
-.55	.84597	.00262	70	.84550
-.60	.83367	.00274	70	.83369
-.65	.82189	.00261	70	.82225
-.70	.81108	.00293	70	.81117

Table 5.12. Limb darkening results for 23132.73 Å

Log μ	Measured limb darkening	Standard deviation	Number of scans	Fitted limb darkening
-.00	1.00000	.00000	70	.99968
-.05	.98385	.00147	70	.98382
-.10	.96809	.00177	70	.96832
-.15	.95304	.00193	70	.95319
-.20	.93835	.00186	70	.93842
-.25	.92394	.00175	70	.92402
-.30	.90979	.00195	70	.90998
-.35	.89630	.00184	70	.89631
-.40	.88305	.00215	70	.88301
-.45	.87008	.00204	70	.87007
-.50	.85775	.00199	70	.85750
-.55	.84549	.00201	70	.84529
-.60	.83382	.00260	70	.83344
-.65	.82180	.00272	70	.82197
-.70	.81052	.00284	70	.81085

Table 5.13. Limb darkening results for 38839.36 Å

Log μ	Measured limb darkening	Standard deviation	Number of scans	Fitted limb darkening
-.00	1.00000	.00000	35	.99960
-.05	.98751	.00166	23	.98793
-.10	.97670	.00179	35	.97659
-.15	.96570	.00179	35	.96559
-.20	.95488	.00206	35	.95491
-.25	.94411	.00194	35	.94457
-.30	.93443	.00227	35	.93456
-.35	.92471	.00127	23	.92489
-.40	.91567	.00146	23	.91554
-.45	.90706	.00216	35	.90653
-.50	.89800	.00182	35	.89785
-.55	.88969	.00223	35	.88950
-.60	.88138	.00188	35	.88148
-.65	.87352	.00259	35	.87379
-.70	.86641	.00233	35	.86644

Table 5.14. Limb darkening results for 38862.02 Å

Log μ	Measured limb darkening	Standard deviation	Number of scans	Fitted limb darkening
-.00	1.00000	.00000	36	.99976
-.05	.98828	.00191	24	.98814
-.10	.97681	.00199	36	.97685
-.15	.96563	.00199	36	.96590
-.20	.95509	.00160	36	.95529
-.25	.94494	.00201	36	.94502
-.30	.93540	.00232	36	.93509
-.35	.92506	.00214	24	.92549
-.40	.91556	.00155	24	.91624
-.45	.90783	.00261	36	.90732
-.50	.89856	.00222	36	.89874
-.55	.89117	.00249	36	.89050
-.60	.88346	.00243	36	.88260
-.65	.87499	.00229	36	.87503
-.70	.46699	.00235	36	.86781

Table 5.15. Limb darkening results for 45908.50 Å

Log μ	Measured limb darkening	Standard deviation	Number of scans	Fitted limb darkening
-.00	1.00000	.00000	36	.99961
-.05	.98902	.00225	36	.98892
-.10	.97836	.00228	36	.97851
-.15	.96831	.00264	36	.96839
-.20	.95839	.00239	36	.95855
-.25	.94822	.00239	36	.94899
-.30	.93954	.00315	36	.93971
-.35	.93086	.00241	36	.93072
-.40	.92209	.00300	36	.92201
-.45	.91382	.00316	36	.91359
-.50	.90603	.00296	36	.90545
-.55	.89774	.00296	36	.89759
-.60	.89023	.00330	36	.89001
-.65	.88269	.00213	36	.88272
-.70	.87518	.00279	36	.87571

Table 5.16. Limb darkening results for 46142.57 Å

Log μ	Measured limb darkening	Standard deviation	Number of scans	Fitted limb darkening
-.00	1.00000	.00000	36	.99952
-.05	.98919	.00255	36	.98910
-.10	.97898	.00284	36	.97900
-.15	.96848	.00254	36	.96921
-.20	.95942	.00283	36	.95973
-.25	.95035	.00258	36	.95057
-.30	.94154	.00266	36	.94172
-.35	.93380	.00242	36	.93318
-.40	.92522	.00273	36	.92496
-.45	.91702	.00251	36	.91706
-.50	.90941	.00281	36	.90946
-.55	.90268	.00296	36	.90219
-.60	.89496	.00289	36	.89522
-.65	.88902	.00287	36	.88857
-.70	.88166	.00264	36	.88224

Table 5.17. Limb darkening results for 85636.32 Å

Log μ	Measured limb darkening	Standard deviation	Number of scans	Fitted limb darkening
-.00	1.00000	.00000	35	.99958
-.05	.99367	.00172	23	.99314
-.10	.98658	.00217	35	.98686
-.15	.98032	.00250	35	.98073
-.20	.97386	.00238	35	.97476
-.25	.96900	.00268	35	.96893
-.30	.96256	.00229	35	.96327
-.35	.95805	.00260	35	.95775
-.40	.94290	.00259	35	.95239
-.45	.94760	.00242	35	.94718
-.50	.94210	.00229	35	.94213
-.55	.93775	.00329	35	.93723
-.60	.93295	.00276	35	.93248
-.65	.92752	.00231	35	.92789
-.70	.92292	.00273	35	.92345

Table 5.18. Limb darkening results for 104007.55 Å

Log μ	Measured limb darkening	Standard deviation	Number of scans	Fitted limb darkening
-.00	1.00000	.00000	41	1.00003
-.05	.99488	.00189	23	.99446
-.10	.98872	.00246	41	.98903
-.15	.98349	.00296	41	.98374
-.20	.97813	.00293	41	.97858
-.25	.97365	.00314	41	.97356
-.30	.96844	.00296	41	.96868
-.35	.96506	.00377	41	.96394
-.40	.95980	.00366	41	.95933
-.45	.95489	.00415	41	.95486
-.50	.95034	.00430	41	.95053
-.55	.94610	.00448	41	.94633
-.60	.94129	.00599	41	.94227
-.65	.93802	.00708	41	.93835
-.70	.93545	.00662	41	.93457

tables were computed in DRIFT2 as APAIR2(I); while the standard deviations were computed as SPAIR2(I). The final results have been limited to $\log \mu$ values between 0.00 and -0.70 in order to avoid systematic errors near the limb. The standard error associated with each of the final limb darkening measures is found by dividing the standard deviation at each position by the square root of the number of scans. The standard errors at $\log \mu = -0.70$ range from ± 0.00030 at 16513.18 Å to ± 0.00111 at 104007.55 Å. The standard errors near disk center are generally smaller than those close to the limb.

Systematic errors at most of the observational wavelengths were larger than the standard errors. The largest systematic errors occurred near the limb and were caused by atmospheric scattering, atmospheric seeing, instrumental diffraction, and variations in the gain and zero point of the detector. The limb darkening measures from 10840.10 to 38862.02 Å have a maximum uncertainty of ± 0.002 when these effects are included in the error estimates. The limb darkening measures at 45908.47 Å have an uncertainty of at least ± 0.006 as a result of the tilt in the scans. Those at 46142.57 Å have a maximum uncertainty of ± 0.003 . The limb darkening measures at 85636.32 and 104007.55 Å have a maximum uncertainty of ± 0.004 .

A least-squares quadratic fit was made to the final limb darkening measures at each wavelength. Fitted limb

darkening measures were then computed at each limb position as follows:

$$\text{FIT} = \text{COEF}(1) + \text{COEF}(2) \cdot \text{XLOGMU} + \text{COEF}(3) \cdot \text{XLOGMU}^2.$$

The coefficients for each wavelength are given in Table 5.19. The fitted limb darkening measures themselves are listed in Tables 5.1 to 5.18. An examination of these tables shows that the final limb darkening measures can be reproduced to an accuracy of ± 0.001 at all but a few positions with the quadratic coefficients. The quadratic coefficients can therefore be used to generate a limb darkening measure that is within the observational errors of this research at virtually any point on the sun.

5.2 Corrections for Variations in the Solar Declination

The paths traced across the solar image by the entrance aperture of the spectrometer were conic sections representing lines of constant declination in the image plane. In the geocentric coordinate system shown in Figure 5.1, the apparent motion of the center of the sun is along the surface of a cone swept out by the line SE. The angular rate of motion of the sun about the z coordinate axis is equal to the angular rotation velocity of the earth ω_e . The angular velocity about a tilted instantaneous axis z', however, is given by $\omega_e \cos \delta$. This declination effect in the drift rate must be taken into account when comparing

Table 5.19. Coefficients for the least-squares quadratic fits to the limb darkening measures.

λ (Å)	COEF (1)	COEF (2)	COEF (3)
10840.10	.998943	.610361	.236998
10854.00	.999146	.609143	.235529
10865.00	.999198	.607389	.234940
12466.63	.999517	.548107	.188594
12505.51	.999488	.549065	.191160
16222.00	.999791	.379879	.077243
16513.18	.999739	.372593	.076625
21855.59	.999883	.328533	.071412
21907.47	.999712	.331219	.075965
23121.03	.999920	.324193	.077803
23127.19	.999799	.321132	.073801
23132.73	.999679	.320915	.073093
38839.36	.999597	.236689	.066373
38862.02	.999762	.235892	.067694
45908.50	.999609	.216645	.056635
46142.57	.999519	.211514	.062810
85636.32	.999579	.130260	.030723
104007.55	1.000029	.112736	.027460

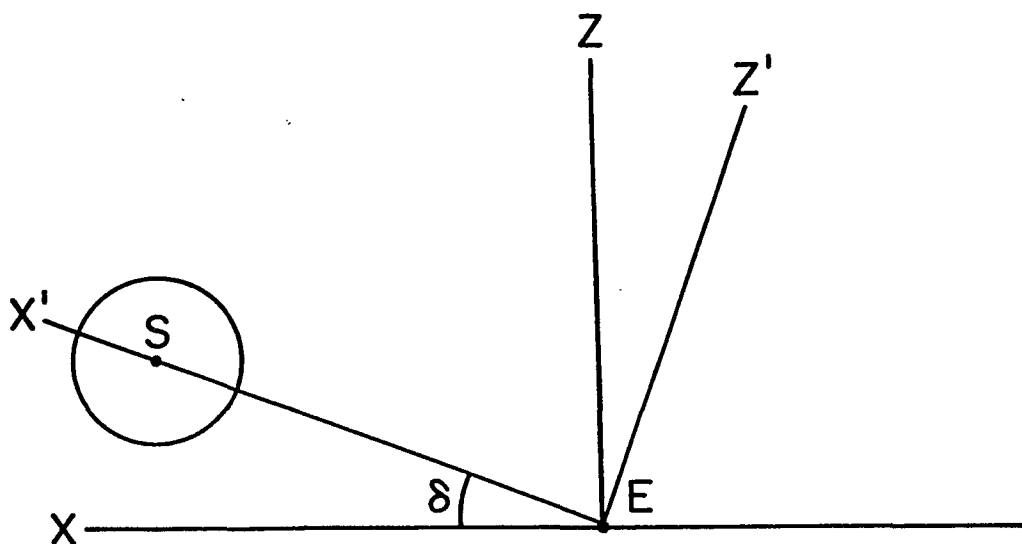


Figure 5.1. Diagram of the coordinate systems used in computing the effect of the solar declination on the path of a drift scan across the sun.

measures of the scattered light off the limb of the sun. It is not important to the calculations of the limb darkening measures because the $\log \mu$ positions used in the reductions were computed from the apparent diameter of the sun in each scan.

The axis of the telescope in Figure 5.1 lies along the line SE which also defines the x' axis of the rotated coordinate system centered on the earth. A scan line across the sun is defined by the locus of points common to the cone swept out by the line SE and the spherical surface of the sun. The equation for such a curve projected into the image plane $x' = -F$ of a telescope objective of focal length F located at the point E is

$$z'^2 \cos 2\delta - 2z'F \cos \delta \sin \delta - y'^2 \sin^2 \delta = 0.$$

At the vernal equinox the solar declination is equal to zero, and the equation reduces to

$$z'^2 = 0$$

which is a straight line. For other solar declinations the path in the image plane is hyperbolic.

The largest declination in the observing run was $+21^\circ 09.5'$ on May 26, 1974, and the diameter of the sun in the scans on this date was $948.7''$. Using 3541.5 cm for the focal length of the West McMath Telescope, a scan through disk center is found to cross the west limb of the sun at the position $y' = +8.1444$ cm and $z' = -0.0036$ cm. This

position represents a deviation from linearity of about 0.21" in going from the center of the disk to the limb. The offset is also produced in a direction that is essentially transverse to the direction of the scan and thus does not directly affect the radial positions of the points actually sampled on the disk. As the effects of the curvature are relatively insignificant, the drift scans were handled in all stages of the data reductions as if they had been taken in straight lines.

5.3 Corrections for Computational Errors in Log μ

Point positions for particular values of XLOGMU in the limb darkening reduction subroutine OPTION were calculated as follows:

$$\begin{aligned} \text{XMU} &= 10.00^{\text{XLOGMU}} \\ \text{THETA} &= \cos^{-1}(\text{XMU}) \\ \text{FRACT} &= \sin(\text{THETA}) \\ \text{POINTW} &= \text{CENTER} - \text{RSOLAR} \cdot \text{FRACT} \\ \text{POINTE} &= \text{CENTER} + \text{RSOLAR} \cdot \text{FRACT} \end{aligned}$$

The variables POINTW and POINTE were thus the point numbers of the two positions in every scan where log μ was equal to XLOGMU. Implicit in the calculation of point numbers from log μ positions in this manner is the geometry shown in Figure 5.2. The center of the solar disk is at C, and the limb is normally taken to be the point L for an

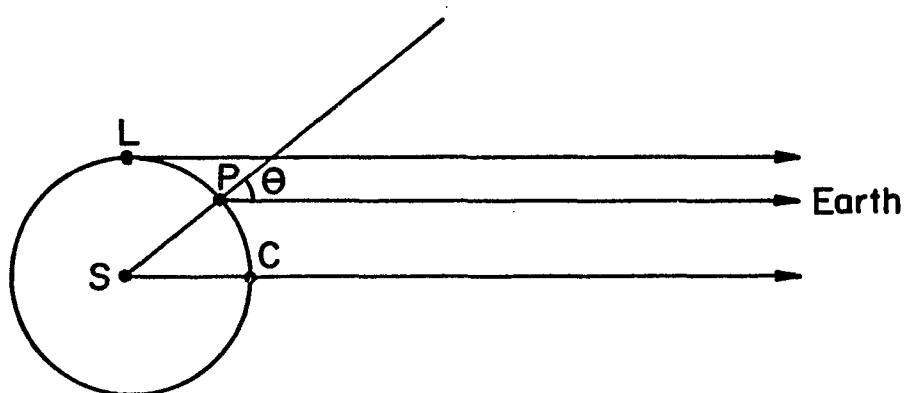


Figure 5.2. Diagram of the geometry used in calculating the limb darkening measures in OPTION.

observer at the earth. With the assumption of this particular geometry, the numerical relationships used in OPTION are exact for points C and L as well as for any other point P on the sun where the emitted ray to the observer makes an angle θ to the normal at the surface.

In actual fact, however, the observed limb does not fall precisely at the point L on the sun because of the finite distance of the sun to the earth. The actual geometry is shown in Figure 5.3. The true value of θ at P' is seen from the geometry to be given by the relation

$$\theta_{\text{true}} = \alpha + \beta.$$

In the subroutine OPTION, however, each point P' was assigned a calculated value of θ such that

$$\theta_{\text{calc}} = \arcsin(\beta/\gamma).$$

The values of θ actually calculated in OPTION are therefore equal to the true values only at disk center where α and β are both zero and at the extreme observable limb L' where

$$\beta = \gamma$$

and

$$\alpha + \beta = \pi/2.$$

At all other points on the disk the true and calculated values of θ are slightly different.

True values of $\log \mu$ are listed for the values of XLOGMU that were used in OPTION in Table 5.20. The true

Table 5.20. True values of $\log \mu$ for a drift scan through disk center ($R_{\odot} = 1599.5$).

XLOGMU	$R_{\odot} = 1599.0$	$R_{\odot} = 1599.5$	$R_{\odot} = 1600.0$
-0.050000	-0.050035	-0.050000	-0.049965
-0.100000	-0.100080	-0.100001	-0.099921
-0.150000	-0.150136	-0.150001	-0.149866
-0.200000	-0.200206	-0.200001	-0.199796
-0.250000	-0.250295	-0.250001	-0.249708
-0.300000	-0.300406	-0.300001	-0.299597
-0.350000	-0.350547	-0.350001	-0.349458
-0.400000	-0.400724	-0.400001	-0.399282
-0.450000	-0.450946	-0.450001	-0.449061
-0.500000	-0.501227	-0.500001	-0.498784
-0.550000	-0.551581	-0.550001	-0.548434
-0.600000	-0.602028	-0.600001	-0.597996
-0.650000	-0.652591	-0.650001	-0.647445
-0.700000	-0.703302	-0.700002	-0.696753
-0.750000	-0.754201	-0.750002	-0.745885
-0.800000	-0.805338	-0.800002	-0.794798
-0.850000	-0.856778	-0.859992	-0.843437
-0.900000	-0.908604	-0.900002	-0.891735
-0.950000	-0.960925	-0.950002	-0.939611
-1.000000	-1.013882	-1.000002	-0.986967

values of $\log \mu$ were calculated using the solar radius given above each column of figures. As the largest systematic error in calculating the solar radius was one-half data point, the three cases cover the possible range of true values for $\log \mu$ when the observed solar radius was 1599.5 data points. The tabulated values were computed using 1.496×10^{13} cm for the distance from the earth to the sun and 6.96×10^{10} cm for the solar radius.

The steepest gradient of the limb darkening in the $\log \mu$ interval from -0.65 to -0.75 was 0.30755 at 10840.10 Å. Using this gradient and the tabulated true values of $\log \mu$, one finds that the observed limb darkening should range from 0.00102 below the true value to 0.00100 above the true value at $XLOGMU = -0.70$. Such errors in the limb darkening will tend to average out over several scans and thus should have a negligible effect on the final limb darkening measures.

The drift scans in each daily set covered a narrow range in declination either side of disk center. The largest offset from disk center was usually 2.5 mm or 14.56". Such an offset changes the apparent diameter of the sun in the scan and also alters the true values of $\log \mu$ that are sampled at various points across the disk. The true values of $\log \mu$ in a scan offset 2.5 mm from disk center are listed in Table 5.21. Using the gradient of 0.30902 that was observed in the limb darkening over the interval in $XLOGMU$ from 0.00 to -0.05 at 10840.10 Å, one finds that the limb

Table 5.21. True values of $\log \mu$ for a drift scan with an offset of 2.5 mm ($R_{\text{O}} = 1599.5$).

XLOGMU	$R_{\text{O}} = 1599.0$	$R_{\text{O}} = 1599.5$	$R_{\text{O}} = 1600.0$
-0.050000	-0.050086	-0.050051	-0.050016
-0.100000	-0.100130	-0.100051	-0.099972
-0.150000	-0.150186	-0.150051	-0.149916
-0.200000	-0.200257	-0.200051	-0.199846
-0.250000	-0.250345	-0.250052	-0.249758
-0.300000	-0.300457	-0.300052	-0.299647
-0.350000	-0.350597	-0.350052	-0.349508
-0.400000	-0.400774	-0.400052	-0.399332
-0.450000	-0.450997	-0.450052	-0.449112
-0.500000	-0.501278	-0.500052	-0.498834
-0.550000	-0.551632	-0.550052	-0.548485
-0.600000	-0.602078	-0.600052	-0.598046
-0.650000	-0.652642	-0.650052	-0.647495
-0.700000	-0.703353	-0.700052	-0.696804
-0.750000	-0.754252	-0.750052	-0.745936
-0.800000	-0.805388	-0.800052	-0.794848
-0.850000	-0.856828	-0.850052	-0.843487
-0.900000	-0.908654	-0.900052	-0.891785
-0.950000	-0.960975	-0.950052	-0.939662
-1.000000	-1.013933	-1.000052	-0.987017

darkening at the center of the sun in the scan should be 0.99998 instead of 1.00000. This error affects all points in the scan equally through the disk-center normalization procedure in OPTION. Even with this additional effect, however, the limb darkening measures at $XLOGMU = -0.70$ should still vary from 0.00102 below to 0.00100 above the true value. The error introduced by offsetting the drift scans is therefore negligible.

5.4 Corrections for Instrumental and Atmospheric Effects

A theoretical drift scan of the sun was generated from the quadratic coefficients at each observational wavelength. These scans were used to study the observational effects that were produced by the diffraction pattern of the telescope, the entrance aperture of the spectrometer, and the atmospheric seeing conditions. The center of the solar profile in each theoretical drift scan was located at the point $I = 2049$, and values of $R(I)$ were computed for a solar radius of 1599.5 data points. The background in each scan was set equal to zero.

The solar image was much larger than the observational smearing functions. The solar limb darkening was therefore expressed as

$$l_1(x,y) = l(x) = R(I); x = (I-2049)/4096.$$

The coordinates x,y were thus defined in units that were

dimensionless fractions of a block length, and the solar profile was assumed to be independent of the variable y .

The transmission function of the entrance aperture of the spectrometer was expressed as

$$a_1(x,y) = a(r) = \frac{1}{\pi r_o^2 s_o^2} \pi \left(\frac{r}{r_o s_o} \right) =$$

$$\begin{cases} \frac{1}{\pi r_o^2 s_o^2} & \text{for } r < r_o s_o \\ \frac{1}{2\pi r_o^2 s_o^2} & \text{for } r = r_o s_o \\ 0 & \text{for } r > r_o s_o \end{cases} ; r = (x^2 + y^2)^{1/2}.$$

The scale factor $s_o = 0.0237 \text{ cm}^{-1}$ was used to convert distances in the image plane into dimensionless fractions of a block length. The parameter r_o was equal to the physical radius of the entrance aperture of the spectrometer.

The diffraction pattern of the telescope was given by the intensity distribution

$$d_1(x,y) = d(r) = \frac{4\pi R_o^2}{(\lambda f_o s_o)^2} \cdot \frac{J_1 \left(\frac{2\pi R_o r}{\lambda f_o s_o} \right)^2}{\left(\frac{2\pi R_o r}{\lambda f_o s_o} \right)^2} ;$$

$$r = (x^2 + y^2)^{1/2}.$$

The parameter $R_o = 40.6 \text{ cm}$ was the radius of the entrance

pupil of the telescope, and $f_o = 3541.5$ cm was the focal length of the primary mirror.

The seeing function for the observations was assumed to be a Gaussian of the form

$$s_1(x,y) = s(r) = \frac{4}{\pi d_o^2 s_o^2} e^{-(4r^2/d_o^2 s_o^2)}; \quad r = (x^2 + y^2)^{1/2}.$$

The parameter d_o was the width of the seeing disk in the image plane.

The observed solar profile was expected to appear very much like the convolution of the functions

$$L(x) = l_1(x, 0),$$

$$A(x) = \int_{-\infty}^{+\infty} a_1(x, y) dy,$$

$$D(x) = \int_{-\infty}^{+\infty} d_1(x, y) dy,$$

and

$$S(x) = \int_{-\infty}^{+\infty} s_1(x, y) dy.$$

The convolution $L(x) * A(x)$ was computed as a direct sum at each point since

$$A(x) = \frac{2(r_o^2 s_o^2 - x^2)^{1/2}}{\pi r_o^2 s_o^2}.$$

The Fourier transform of $L(x) * A(x)$ was then computed in REDUCER using the command FOURTRAN. The transform $\overline{L(x) * A(x)}$ = $\overline{L(x)} \cdot \overline{A(x)}$ was next multiplied by $\overline{D(x)} \cdot \overline{S(x)}$. Since a

Hankel transform is equivalent to an Abel transform followed by a one-dimensional Fourier transform, $\overline{D(x)}$ and $\overline{S(x)}$ were computed from the Hankel transforms of $d(r)$ and $s(r)$. Thus,

$$D(x) = \frac{2}{\pi} \left[\cos^{-1} \left(\frac{\lambda f_o s_o u}{2R_o} \right) - \left(\frac{\lambda f_o s_o u}{2R_o} \right) \left(1 - \left(\frac{\lambda f_o s_o u}{2R_o} \right)^2 \right)^{1/2} \right]$$

and

$$\overline{S(x)} = e^{-\left(\frac{\pi s_o d_o u}{2} \right)^2}$$

where u is the coordinate in frequency space. The product $\overline{L(x)} \cdot \overline{A(x)} \cdot \overline{D(x)} \cdot \overline{S(x)}$ was then inverse transformed with the REDUCER command INVTRAN. The resulting solar profile was equal to $L(x) * A(x) * D(x) * S(x)$.

The theoretical drift scans and the convolved drift scans were each processed with REDUCER and the limb darkening subroutine OPTION. The difference between each limb darkening measure that was derived from $L(x) * A(x) * D(x) * S(x)$ and the corresponding measure from $L(x)$ was then calculated at each limb position. The differences for three limb positions are listed in Table 5.22.

A short scan of the background radiation was made from each convolved drift scan in order to determine if the convolution procedure accurately predicted the scattered light in the observational drift scans. These short scans were processed with REDUCER, and the resulting measures of the scattered light were compared to the observational measures at each wavelength. The theoretical scattered

Table 5.22. Theoretical limb darkening errors for a 2" seeing disk.

λ (Å)	XLOGMU		
	-0.50	-0.70	-0.95
10840.10	.00040	.00069	.00057
10854.00	.00041	.00070	.00060
10865.00	.00040	.00068	.00056
12466.63	.00033	.00058	.00049
12505.51	.00031	.00053	.00036
16222.00	-.00004	-.00017	-.00116
16513.18	-.00009	-.00030	-.00151
21855.59	-.00043	-.00113	-.00400
21907.47	-.00044	-.00117	-.00410
23121.03	-.00051	-.00134	-.00463
23127.19	-.00051	-.00133	-.00458
23132.73	-.00050	-.00132	-.00457
38839.36	-.00115	-.00299	-.00991
38862.02	-.00116	-.00300	-.00994
45908.50	-.00137	-.00357	-.01187
46142.57	-.00139	-.00362	-.01207
85636.32	-.00299	-.00852	-.12200
104007.55	-.00352	-.01009	-.13392

light measures for a 2" seeing disk are given along with the observational measures of the scattered light in Tables 5.23 to 5.40. The observed measures from 10840.10 to 12505.51 Å are all greater than expected. Those from 16222.00 to 21907.47 Å are high just beyond the limb and almost the same as expected farther out. The observational measures from 23127.19 to 104007.55 Å tend to be smaller than those predicted at nearly all positions off the limb.

The high values of the scattered light can be accounted for fairly easily since Rayleigh and aerosol scattering could cause the observed measures to be greater than expected. The low measures of the scattered light, however, are more difficult to explain. The possibility of an error in the theoretical treatment of the atmospheric seeing was ruled out when it was found that the discrepancy between the observed and predicted measures remained even when the smearing function for the seeing was left out of the computations. An error in the theoretical treatment of the diffraction was also unlikely since the scattered light from a two-dimensional integral of an approximate expression for the diffraction pattern of the telescope was found to be nearly identical to the scattered light that was predicted from the theoretical drift scans.

The discrepancy between the observed and predicted measures of the scattered light was finally resolved when it was realized that the spectrometer was a partially coherent

Table 5.23. Scattered light results for 10840.10 Å

Distance from limb	Measured scattered light	Standard deviation	Number of scans	Expected scattered light
1"	.24353	.02285	36	.18555
2"	.14540	.02969	36	.05413
3"	.07945	.02822	36	.01079
4"	.04094	.01860	36	.00367
5"	.02150	.00947	36	.00255
6"	.01267	.00492	36	.00205
7"	.00790	.00246	36	.00172
8"	.00552	.00162	36	.00148
9"	.00428	.00117	36	.00130
10"	.00348	.00103	36	.00116
15"	.00178	.00028	36	.00074
20"	.00127	.00020	36	.00054
25"	.00103	.00017	36	.00042
30"	.00089	.00016	36	.00033
35"	.00078	.00015	36	.00027
40"	.00071	.00016	36	.00023
45"	.00063	.00015	36	.00019
50"	.00058	.00015	36	.00017
55"	.00053	.00015	36	.00014
60"	.00049	.00014	36	.00012

Table 5.24. Scattered light results for 10854.00 Å

Distance from limb	Measured scattered light	Standard deviation	Number of scans	Expected scattered light
1"	.24329	.03233	35	.18574
2"	.14975	.04233	35	.05422
3"	.08319	.03080	35	.01085
4"	.04169	.01862	35	.00368
5"	.02257	.01182	35	.00256
6"	.01185	.00481	35	.00205
7"	.00739	.00273	35	.00172
8"	.00518	.00185	35	.00148
9"	.00390	.00112	35	.00130
10"	.00311	.00079	35	.00116
15"	.00166	.00036	35	.00075
20"	.00121	.00020	35	.00054
25"	.00099	.00017	35	.00042
30"	.00086	.00016	35	.00033
35"	.00077	.00014	35	.00027
40"	.00069	.00013	35	.00023
45"	.00063	.00013	35	.00020
50"	.00057	.00014	35	.00017
55"	.00052	.00012	35	.00014
60"	.00047	.00013	35	.00012

Table 5.25. Scattered light results for 10865.00 Å

Distance from limb	Measured scattered light	Standard deviation	Number of scans	Expected scattered light
1"	.24152	.02211	36	.18537
2"	.13636	.02958	36	.05406
3"	.06843	.02644	36	.01077
4"	.03562	.02033	36	.00368
5"	.01966	.01428	36	.00256
6"	.01184	.00843	36	.00206
7"	.00814	.00668	36	.00172
8"	.00569	.00414	36	.00148
9"	.00426	.00193	36	.00130
10"	.00341	.00111	36	.00116
15"	.00181	.00040	36	.00075
20"	.00130	.00025	36	.00054
25"	.00105	.00018	36	.00042
30"	.00090	.00016	36	.00033
35"	.00080	.00015	36	.00028
40"	.00071	.00015	36	.00023
45"	.00066	.00015	36	.00020
50"	.00059	.00013	36	.00017
55"	.00053	.00015	36	.00014
60"	.00047	.00014	36	.00013

Table 5.26. Scattered light results for 12466.63 Å

Distance from limb	Measured scattered light	Standard deviation	Number of scans	Expected scattered light
1"	.21675	.02684	60	.18521
2"	.11249	.03409	60	.05475
3"	.05344	.02768	60	.01155
4"	.02727	.02092	60	.00425
5"	.01553	.01316	60	.00299
6"	.00910	.00613	60	.00241
7"	.00651	.00448	60	.00203
8"	.00490	.00341	60	.00175
9"	.00366	.00214	60	.00154
10"	.00283	.00143	60	.00137
15"	.00133	.00041	60	.00089
20"	.00088	.00036	60	.00065
25"	.00068	.00036	60	.00050
30"	.00057	.00038	60	.00041
35"	.00052	.00035	60	.00034
40"	.00048	.00036	60	.00028
45"	.00043	.00034	60	.00024
50"	.00038	.00034	60	.00021
55"	.00035	.00034	60	.00018
60"	.00036	.00033	60	.00016

Table 5.27. Scattered light results for 12505.51 Å

Distance from limb	Measured scattered light	Standard deviation	Number of scans	Expected scattered light
1"	.22412	.02994	60	.18449
2"	.12286	.03415	60	.05445
3"	.06563	.02438	60	.01138
4"	.03557	.01696	60	.00426
5"	.02072	.01141	60	.00301
6"	.01331	.00663	60	.00242
7"	.00931	.00496	60	.00204
8"	.00716	.00375	60	.00175
9"	.00538	.00327	60	.00154
10"	.00405	.00207	60	.00138
15"	.00171	.00062	60	.00089
20"	.00100	.00035	60	.00065
25"	.00074	.00027	60	.00051
30"	.00060	.00023	60	.00041
35"	.00053	.00023	60	.00034
40"	.00048	.00022	60	.00029
45"	.00045	.00021	60	.00024
50"	.00037	.00022	60	.00021
55"	.00036	.00020	60	.00018
60"	.00034	.00022	60	.00016

Table 5.28. Scattered light results for 16222.00 Å

Distance from limb	Measured scattered light	Standard deviation	Number of scans	Expected scattered light
1"	.21274	.03514	93	.17647
2"	.11868	.04082	93	.05264
3"	.06417	.02966	93	.01131
4"	.03712	.02271	93	.00558
5"	.02242	.01328	93	.00408
6"	.01479	.00977	93	.00330
7"	.01038	.00675	93	.00279
8"	.00744	.00410	93	.00241
9"	.00559	.00258	93	.00212
10"	.00441	.00191	93	.00190
15"	.00186	.00069	93	.00124
20"	.00105	.00049	93	.00090
25"	.00071	.00044	93	.00070
30"	.00054	.00039	93	.00057
35"	.00046	.00037	93	.00047
40"	.00040	.00038	93	.00040
45"	.00035	.00041	93	.00034
50"	.00031	.00038	93	.00029
55"	.00026	.00039	93	.00026
60"	.00025	.00037	93	.00022

Table 5.29. Scattered light results for 16513.18 Å

Distance from limb	Measured scattered light	Standard deviation	Number of scans	Expected scattered light
1"	.20993	.03616	104	.17458
2"	.11263	.03872	104	.05191
3"	.06006	.02956	104	.01117
4"	.03334	.01915	104	.00568
5"	.02034	.01309	104	.00417
6"	.01284	.00704	104	.00337
7"	.00928	.00533	104	.00285
8"	.00678	.00331	104	.00247
9"	.00531	.00251	104	.00217
10"	.00417	.00195	104	.00195
15"	.00175	.00062	104	.00127
20"	.00100	.00041	104	.00092
25"	.00066	.00038	104	.00072
30"	.00050	.00037	104	.00058
35"	.00041	.00036	104	.00048
40"	.00034	.00036	104	.00040
45"	.00031	.00035	104	.00035
50"	.00027	.00034	104	.00030
55"	.00023	.00033	104	.00026
60"	.00023	.00033	104	.00023

Table 5.30. Scattered light results for 21855.59 Å

Distance from limb	Measured scattered light	Standard deviation	Number of scans	Expected scattered light
1"	.18963	.03165	47	.16644
2"	.09273	.02962	47	.05051
3"	.04621	.01821	47	.01363
4"	.02424	.00790	47	.00745
5"	.01532	.00520	47	.00566
6"	.01045	.00361	47	.00460
7"	.00774	.00260	47	.00388
8"	.00597	.00200	47	.00337
9"	.00498	.00174	47	.00297
10"	.00421	.00164	47	.00266
15"	.00203	.00068	47	.00173
20"	.00130	.00052	47	.00126
25"	.00099	.00043	47	.00098
30"	.00078	.00035	47	.00079
35"	.00065	.00032	47	.00065
40"	.00055	.00034	47	.00055
45"	.00049	.00035	47	.00047
50"	.00044	.00032	47	.00041
55"	.00041	.00028	47	.00035
60"	.00038	.00029	47	.00031

Table 5.31. Scattered light results for 21907.47 Å

Distance from limb	Measured scattered light	Standard deviation	Number of scans	Expected scattered light
1"	.19137	.03754	71	.16559
2"	.09552	.03818	71	.05011
3"	.04636	.02519	71	.01362
4"	.02580	.01613	71	.00746
5"	.01590	.01057	71	.00567
6"	.01034	.00636	71	.00461
7"	.00737	.00341	71	.00389
8"	.00561	.00239	71	.00338
9"	.00441	.00155	71	.00298
10"	.00358	.00126	71	.00266
15"	.00162	.00073	71	.00173
20"	.00096	.00065	71	.00126
25"	.00063	.00048	71	.00098
30"	.00045	.00042	71	.00079
35"	.00041	.00044	71	.00065
40"	.00035	.00049	71	.00055
45"	.00029	.00053	71	.00047
50"	.00026	.00049	71	.00041
55"	.00025	.00043	71	.00036
60"	.00022	.00042	71	.00031

Table 5.32. Scattered light results for 23121.03 Å

Distance from limb	Measured scattered light	Standard deviation	Number of scans	Expected scattered light
1"	.18500	.02675	36	.16351
2"	.08247	.03203	36	.04963
3"	.03774	.01962	36	.01416
4"	.01783	.00741	36	.00786
5"	.01080	.00542	36	.00601
6"	.00767	.00460	36	.00490
7"	.00570	.00353	36	.00413
8"	.00417	.00191	36	.00359
9"	.00327	.00145	36	.00317
10"	.00264	.00119	36	.00283
15"	.00143	.00064	36	.00184
20"	.00097	.00062	36	.00134
25"	.00068	.00064	36	.00104
30"	.00054	.00055	36	.00084
35"	.00047	.00063	36	.00069
40"	.00041	.00069	36	.00059
45"	.00034	.00083	36	.00050
50"	.00023	.00093	36	.00043
55"	.00020	.00089	36	.00038
60"	.00025	.00085	36	.00033

Table 5.33. Scattered light results for 23127.19 Å

Distance from limb	Measured scattered light	Standard deviation	Number of scans	Expected scattered light
1"	.19163	.03456	70	.16410
2"	.09510	.02887	70	.04993
3"	.04700	.02168	70	.01419
4"	.02530	.01085	70	.00787
5"	.01551	.00588	70	.00602
6"	.01068	.00374	70	.00490
7"	.00794	.00283	70	.00414
8"	.00625	.00246	70	.00359
9"	.00495	.00200	70	.00317
10"	.00407	.00174	70	.00283
15"	.00187	.00081	70	.00184
20"	.00095	.00074	70	.00134
25"	.00065	.00078	70	.00104
30"	.00043	.00072	70	.00084
35"	.00028	.00068	70	.00070
40"	.00029	.00066	70	.00059
45"	.00022	.00064	70	.00050
50"	.00023	.00066	70	.00043
55"	.00017	.00068	70	.00038
60"	.00012	.00069	70	.00033

Table 5.34. Scattered light results for 23132.73 Å

Distance from limb	Measured scattered light	Standard deviation	Number of scans	Expected scattered light
1"	.18060	.03998	70	.16431
2"	.08538	.03161	70	.05004
3"	.03960	.01481	70	.01420
4"	.02060	.00697	70	.00787
5"	.01299	.00435	70	.00602
6"	.00933	.00343	70	.00490
7"	.00704	.00280	70	.00413
8"	.00545	.00217	70	.00359
9"	.00441	.00179	70	.00317
10"	.00369	.00146	70	.00283
15"	.00181	.00086	70	.00184
20"	.00102	.00079	70	.00134
25"	.00072	.00072	70	.00104
30"	.00056	.00053	70	.00084
35"	.00042	.00053	70	.00070
40"	.00035	.00050	70	.00059
45"	.00027	.00054	70	.00050
50"	.00026	.00049	70	.00043
55"	.00021	.00056	70	.00038
60"	.00019	.00051	70	.00033

Table 5.35. Scattered light results for 38839.36 Å

Distance from limb	Measured scattered light	Standard deviation	Number of scans	Expected scattered light
1"	.12644	.03110	35	.16447
2"	.04888	.01971	35	.05132
3"	.02357	.00842	35	.02147
4"	.01413	.00376	35	.01368
5"	.00958	.00302	35	.01049
6"	.00720	.00173	35	.00862
7"	.00568	.00147	35	.00731
8"	.00449	.00126	35	.00633
9"	.00367	.00089	35	.00559
10"	.00304	.00070	35	.00500
15"	.00148	.00053	35	.00323
20"	.00090	.00043	35	.00234
25"	.00057	.00041	35	.00180
30"	.00040	.00036	35	.00144
35"	.00032	.00039	35	.00118
40"	.00032	.00046	35	.00098
45"	.00022	.00040	35	.00083
50"	.00012	.00039	35	.00071
55"	.00018	.00037	35	.00061
60"	.00008	.00032	35	.00053

Table 5.36. Scattered light results for 38862.02 Å.

Distance from limb	Measured scattered light	Standard deviation	Number of scans	Expected scattered light
1"	.13248	.03635	36	.16417
2"	.04870	.01600	36	.05128
3"	.02253	.00759	36	.02145
4"	.01457	.00483	36	.01370
5"	.00965	.00325	36	.01051
6"	.00716	.00225	36	.00864
7"	.00552	.00162	36	.00732
8"	.00443	.00136	36	.00634
9"	.00356	.00114	36	.00560
10"	.00306	.00099	36	.00501
15"	.00158	.00060	36	.00324
20"	.00094	.00055	36	.00234
25"	.00059	.00047	36	.00180
30"	.00043	.00048	36	.00144
35"	.00037	.00045	36	.00118
40"	.00023	.00045	36	.00099
45"	.00018	.00051	36	.00083
50"	.00012	.00041	36	.00071
55"	.00008	.00040	36	.00061
60"	.00007	.00039	36	.00053

Table 5.37. Scattered light results for 45908.50 Å.

Distance from limb	Measured scattered light	Standard deviation	Number of scans	Expected scattered light
1"	.15621	.02980	36	.16824
2"	.06981	.01909	36	.05672
3"	.03955	.01159	36	.02500
4"	.02738	.01263	36	.01624
5"	.01831	.00708	36	.01249
6"	.01378	.00472	36	.01026
7"	.01109	.00410	36	.00870
8"	.00915	.00329	36	.00754
9"	.00782	.00320	36	.00666
10"	.00663	.00277	36	.00595
15"	.00366	.00184	36	.00385
20"	.00233	.00147	36	.00278
25"	.00179	.00141	36	.00214
30"	.00139	.00138	36	.00171
35"	.00073	.00142	36	.00141
40"	.00056	.00140	36	.00117
45"	.00051	.00135	36	.00099
50"	.00049	.00137	36	.00085
55"	.00035	.00152	36	.00073
60"	.00043	.00130	36	.00063

Table 5.38. Scattered light results for 46142.57 Å.

Distance from limb	Measured scattered light	Standard deviation	Number of scans	Expected scattered light
1"	.14030	.03651	36	.16678
2"	.06242	.02232	36	.05659
3"	.03528	.01640	36	.02493
4"	.02315	.00997	36	.01641
5"	.01645	.00582	36	.01265
6"	.01279	.00569	36	.01038
7"	.01019	.00401	36	.00881
8"	.00845	.00317	36	.00764
9"	.00665	.00220	36	.00675
10"	.00584	.00206	36	.00603
15"	.00302	.00174	36	.00390
20"	.00217	.00151	36	.00282
25"	.00145	.00139	36	.00217
30"	.00109	.00135	36	.00173
35"	.00072	.00131	36	.00142
40"	.00056	.00157	36	.00119
45"	.00057	.00139	36	.00100
50"	.00057	.00146	36	.00086
55"	.00035	.00118	36	.00074
60"	.00051	.00156	36	.00064

Table 5.39. Scattered light results for 85636.32 Å

Distance from limb	Measured scattered light	Standard deviation	Number of scans	Expected scattered light
1"	.26510	.02483	35	.29581
2"	.19072	.03245	35	.22835
3"	.12714	.03418	35	.16609
4"	.08026	.02988	35	.11123
5"	.04571	.02160	35	.06816
6"	.02564	.01116	35	.03899
7"	.01472	.00588	35	.02358
8"	.00993	.00308	35	.01738
9"	.00751	.00293	35	.01431
10"	.00632	.00273	35	.01236
15"	.00337	.00159	35	.00758
20"	.00181	.00219	35	.00540
25"	.00135	.00145	35	.00413
30"	.00074	.00125	35	.00330
35"	.00071	.00173	35	.00270
40"	.00034	.00156	35	.00226
45"	.00047	.00179	35	.00191
50"	.00029	.00134	35	.00163
55"	-.00014	.00122	35	.00140
60"	.00036	.00127	35	.00121

Table 5.40. Scattered light results for 104007.55 Å.

Distance from limb	Measured scattered light	Standard deviation	Number of scans	Expected scattered light
1"	.25750	.02243	41	.29597
2"	.19019	.02952	41	.22870
3"	.12706	.02918	41	.16716
4"	.07959	.02652	41	.11338
5"	.04069	.01689	41	.07131
6"	.02262	.01249	41	.04339
7"	.01243	.01036	41	.02785
8"	.01083	.01017	41	.02089
9"	.00757	.00894	41	.01736
10"	.00863	.00966	41	.01503
15"	.00285	.00498	41	.00925
20"	.00319	.00545	41	.00660
25"	.00189	.00556	41	.00505
30"	.00072	.00510	41	.00403
35"	.00074	.00572	41	.00331
40"	-.00102	.00498	41	.00276
45"	.00057	.00490	41	.00233
50"	-.00009	.00434	41	.00199
55"	.00098	.00496	41	.00171
60"	.00227	.00478	41	.00148

detector and that the theoretical estimates of the scattered light would only hold if the diffraction pattern of the telescope were very much larger or smaller than the entrance aperture of the spectrometer. The phase of the radiation falling on various parts of the entrance aperture must be taken into account for all situations in between these two extremes. The observed measures of the scattered light seem to be low at a number of wavelengths in this research because a significant fraction of the radiation outside the central maximum of the telescope diffraction pattern missed the collimator of the spectrometer after it passed through the entrance aperture. Since the scattered light is very sensitive to the instrumental configuration, the observational measures of the scattered light in Tables 5.23 to 5.40 really only apply to the drift scans that were taken in this research. The results also indicate that deconvolutions which are based only on the diffraction pattern of the telescope and the size of the entrance aperture of the spectrometer are not reliable. In many cases in the past such computations have resulted in predictions of limb brightening at wavelengths that are formed far below the chromosphere.

The calculated differences between the limb darkening measures that were derived from the convolved drift scans and the limb darkening measures from the theoretical drift scans were intended to be used to correct the

observational measures of the limb darkening. Since the scattered light was underestimated at short wavelengths and overestimated at long wavelengths, estimates of the systematic errors in the limb darkening measures were derived from the observational measures of the scattered light rather than the theoretical computations. These estimates were based on the assumption that the scattered light at a given distance beyond the limb was equal to the radiation lost at the same distance inside the limb. This hypothesis was tested by comparing the scattered light measures at 6" from the limb to the differences between the fitted and observed limb darkening measures at $\log \mu = -0.95$. Table 5.41 shows that the agreement is excellent except at 85636.32 and 104007.55 Å. The disparity at these two wavelengths is due to the fact that the entrance aperture of the spectrometer was 14.6" in diameter.

The position $\log \mu = -0.70$ was located approximately 19.3" inside the limb of the sun in each drift scan. The scattered light measures at 20" off the limb of the sun thus provide reasonable estimates of the corrections that are needed at $\log \mu = -0.70$. These scattered light measures are plotted as a function of wavelength in Figure 5.4. The limb darkening measures from 10840.10 to 38862.02 Å need to be raised by amounts that vary from 0.00088 to 0.00130. Those from 45908.50 to 104007.55 Å need to be raised by amounts that range from 0.00181 to 0.00319. The corrections

Table 5.41. Fitted limb darkening minus observed limb darkening at $\log \mu = -0.95$ and the scattered light 6" from the limb.

λ (Å)	Fitted limb darkening minus observed limb darkening	Measured scattered light
10840.10	.01398	.01267
10854.00	.01317	.01185
10865.00	.01226	.01184
12466.63	.00880	.00910
12505.51	.01144	.01331
16222.00	.01136	.01479
16513.18	.01148	.01284
21855.59	.01093	.01045
21907.47	.01060	.01034
23121.03	.00844	.00767
23127.19	.01197	.01068
23132.73	.00806	.00933
38839.36	.00728	.00720
38862.02	.00842	.00716
45908.50	.01281	.01378
46142.57	.01400	.01279
85636.32	.07068	.02564
104007.55	.08349	.02262

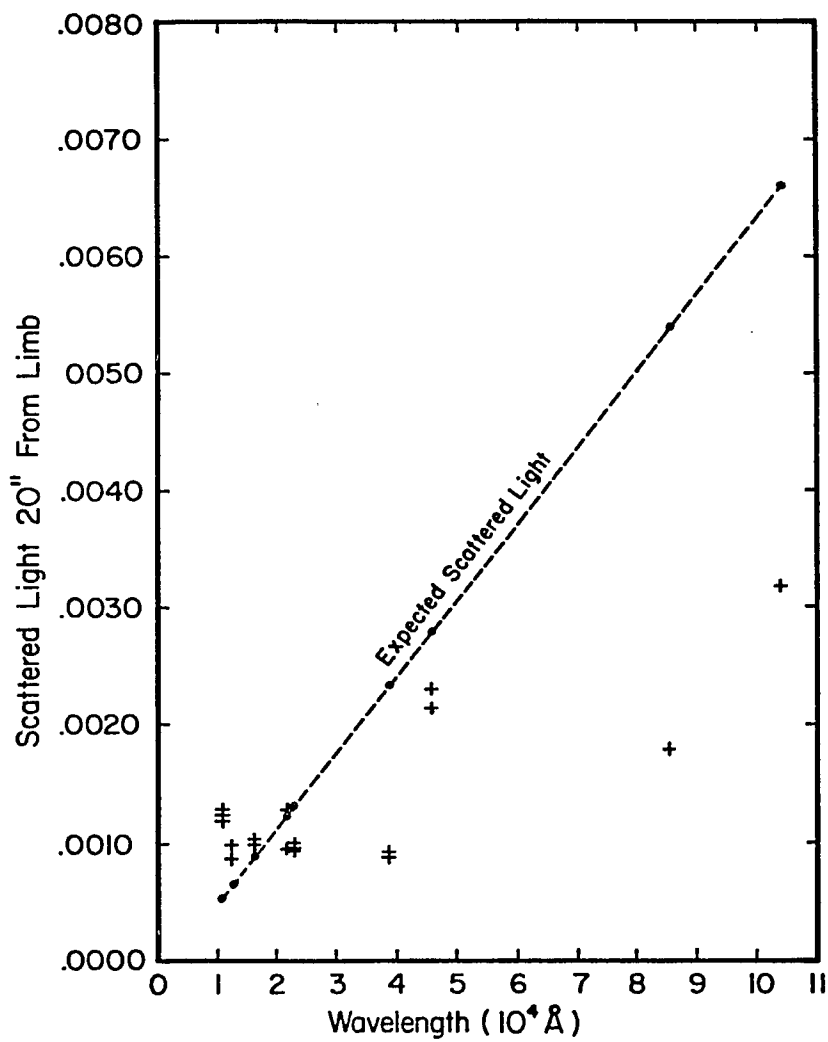


Figure 5.4. Observed measures of the scattered light 20" from the limb.

that are needed closer to disk center are significantly smaller. Because of the small and uncertain nature of the estimated corrections, none were actually applied to the final limb darkening measures.

The limb darkening reductions assumed that the background radiation was identically equal to zero at 2.5 or 3.0' from the limb. The convolved drift scans indicated that this background radiation actually varied from 0.0001 at the shortest wavelengths in the observing program to 0.0015 at the longest wavelengths. The fact that the observed scattered light measures were about three times smaller than those predicted at the longest wavelengths, however, tends to indicate that the actual background radiation was probably less than 0.0005 at all wavelengths. Direct observations that were taken at 3' and 5° from the sun at several wavelengths support this conclusion.

5.5 Corrections for Nonlinearities in the Instrumentation

The agreement between the west and east limbs of the sun shows that there were no significant variations in the instrumental gain during the drift scans. Background scans taken at the end of each daily set with the entrance aperture of the spectrometer closed also indicate that the instrumental zero varied in a highly linear manner. Solar heating effects on the entrance aperture of the spectrometer were also investigated and found to be negligible. Light

contamination from other spectral orders was eliminated by carefully selecting the filters and slit widths that were used at each wavelength during the observations.

The linearity of the InSb detector was checked at 21907.47 Å at the end of the observing run. The transmission of a broad-band filter in front of the entrance slit of the spectrometer was measured at four different light levels by changing the width of the exit slit of the spectrometer. A different gain setting on the a/d converter was used for each set of measures. Ten measures of the filter transmission were taken at each light level. The mean measures of the filter transmission and the standard errors of the mean measures are listed in Table 5.42. The average value of all the measures is 0.80589. The per cent difference between each mean measure and the average for all of the measures is shown in Figure 5.5. Since the average value of the filter transmission lies within the standard error range of each mean measure, there is no indication of a non-linearity in the detector. No linearity tests were performed with the silicon diode or the arsenic-doped silicon detector. Both of these detectors were expected to be acceptably linear at the signal levels that were encountered in this research.

Table 5.42. Results of the detector linearity test.

Exit slit	Filter transmission	Standard error	Gain setting
0.100 mm	0.80617	± 0.00050	.01 mA
0.200 mm	0.80626	± 0.00048	.02 mA
0.400 mm	0.80557	± 0.00032	.05 mA
0.600 mm	0.80554	± 0.00035	.10 mA

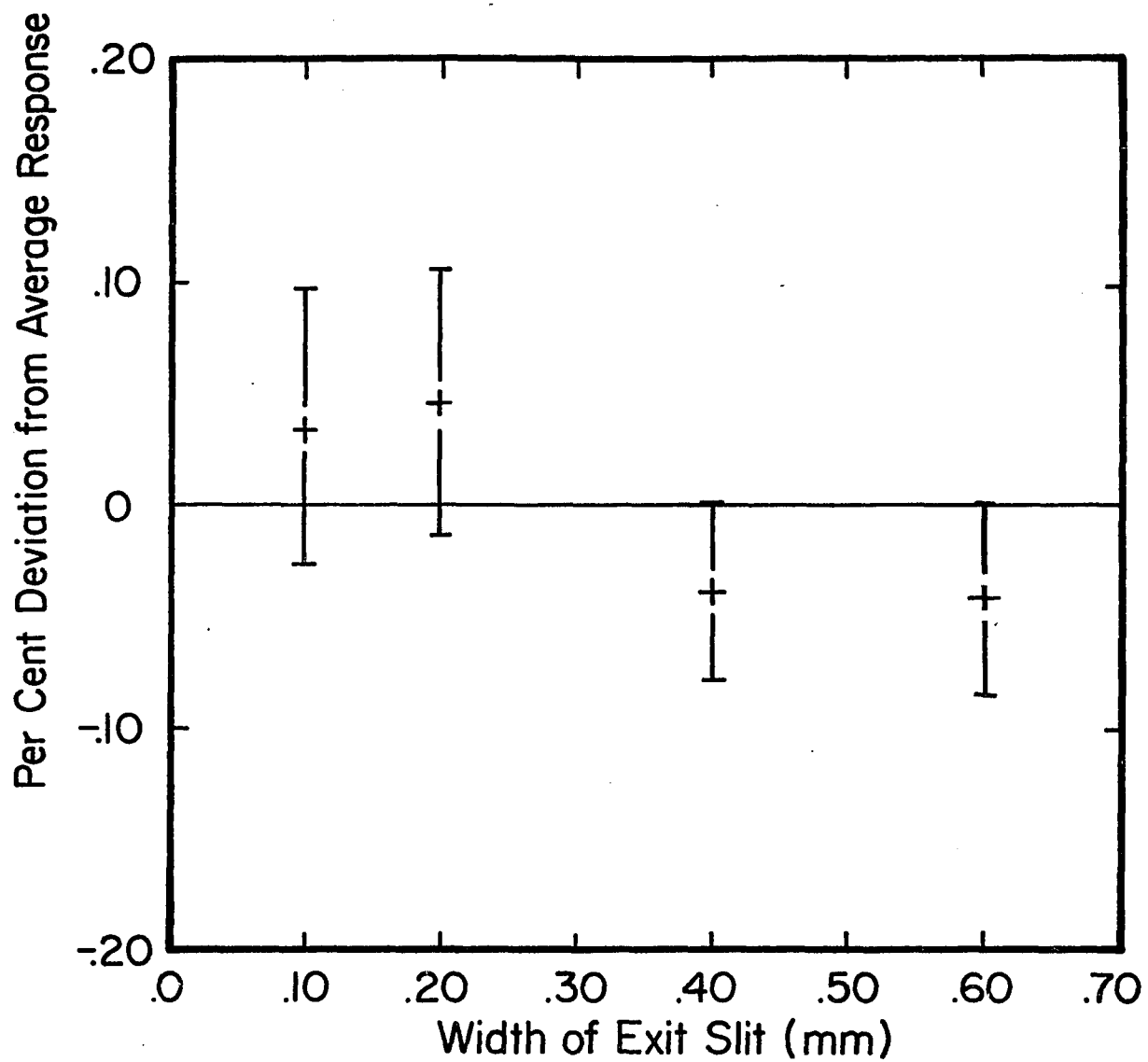


Figure 5.5. Per cent deviation from the average response for the InSb detector.

CHAPTER 6

THE SOLAR ABSOLUTE INTENSITY OBSERVATIONS

The absolute intensity measures of several independent investigators were used to develop empirical models of the solar temperature structure in this research. In general, only a few well-calibrated measures were chosen from each investigator. Many of these measures were corrected for line blanketing or for changes in the absolute temperature scale before they were used in calibrating the models. A brief discussion of the basic principles that are involved in measuring solar absolute intensities is provided in Section 6.1. The observations of Labs and Neckel (1962, 1963, 1967, 1968, 1970) are then discussed in Section 6.2. The absolute intensity observations of Saiedy and Goody (1959) and Saiedy (1960) are described in Section 6.3. The observations of Houtgast (1970) are discussed in Section 6.4.

6.1 Principles of the Solar Absolute Intensity Observations

Published absolute solar intensity measures are normally referenced to black body sources that have been calibrated either on the International Practical Temperature Scale of 1948 (IPTS-48) or the International Practical

Temperature Scale of 1968 (ITS-68). The Celsius temperature scale in the ITS-48 was fixed to the freezing point of water at 0°C and the boiling point of water at 100°C. The Kelvin scale was then established by adopting the unit of temperature for the Celsius scale and assigning a value of 273.15°K to the ice point at 0°C. In the ITS-68 the triple point of water was fixed at 0.01°C. The basic unit of temperature, the Kelvin, was then defined as the fraction 1/273.16 of the thermodynamic temperature of the triple point. Usage of the term "degree Kelvin" was discontinued, and Kelvin temperatures in the ITS-68 are expressed directly in Kelvins (K). Celsius temperatures are still properly given in degrees C (°C). A further discussion of the ITS-68 can be found in Barber (1969). A similar description of the older ITS-48 is given in Stimson (1949).

The highest primary fixed point in both the ITS-48 and the ITS-68 is the freezing point of gold. All temperatures above the gold point are then defined by the following equation that is based on the Planck radiation law:

$$\frac{I_{\lambda}(T)}{I_{\lambda}(T_{Au})} = \frac{\exp(c_2/\lambda T_{Au}) - 1}{\exp(c_2/\lambda T) - 1} .$$

In this equation $I_{\lambda}(T)$ is equal to the intensity of a black body at the temperature T , and $I_{\lambda}(T_{Au})$ is equal to the intensity of a black body at the temperature of freezing gold T_{Au} . The effective temperature of an unknown source is

thus defined directly by the ratio of its own intensity to that of an ideal black body at the gold point. Such an ideal black body can be approximated experimentally by placing a spherical cavity with a small observing aperture in direct contact with a mixture of liquid and solid gold. If the material on the internal surface of the cavity is moderately diffusive and also has a high absorptivity, the overall cavity emissivity will be very close to unity. The intensity distribution of the radiation emitted by the cavity will then be given by the Planck function.

An unknown absolute intensity $I_\lambda(T)$ is often determined experimentally by using a differential observing technique to measure the ratio $I_\lambda(T)/I_\lambda(T_{Au})$. Usually in such an experiment both the radiation source under investigation and a primary standard black body are examined alternately with the same observing equipment. The angular distribution and wavelength of the incident radiation that reaches the detector will then be identical for the two sources, making the ratio of the instrumental signals $S_\lambda(T)/S_\lambda(T_{Au})$ a direct measure of the intrinsic intensity ratio $I_\lambda(T)/I_\lambda(T_{Au})$. The unknown intensity $I_\lambda(T)$ is then calculated from the observed signal ratio as follows:

$$I_\lambda(T) = \frac{S_\lambda(T)}{S_\lambda(T_{Au})} \cdot \frac{2c_1/\lambda^5}{\exp(c_2/\lambda T_{Au}) - 1} \cdot$$

In this equation the calculated intensity $I_{\lambda}(T)$ is shown to depend not only on the observed signal ratio but also on the values adopted for the physical constants c_1 , c_2 , and T_{Au} . The value of the radiation constant $c_1 = hc^2$ is left undefined in both the IPTS-48 and the IPTS-68 because it does not explicitly appear in any of the equations used to define either temperature scale. The radiation constant $c_2 = hc/k$ does have a defined value, however, because it specifically appears in the equation establishing the temperature scale above the gold point. The value of c_2 adopted in the IPTS-48 was 1.4380 cm °K. This value was then revised to 1.4388 cm K in the IPTS-68. The thermodynamic temperature of freezing gold is also defined in both the IPTS-48 and the IPTS-68. The value of T_{Au} in the IPTS-48 was 1336.15 °K. This value was changed to 1337.58 °K in the IPTS-68.

6.2 Absolute Intensity Observations of Labs and Neckel

A comprehensive set of solar absolute intensity measures from 3287.9 to 12480.0 Å was published and discussed by Labs and Neckel (1962, 1963, 1967, 1968, 1970). The disk-center intensity measures that were reported in this series of papers were obtained at the Jungfrauoch Scientific Station in Switzerland at an altitude of 3600 m. These observations were performed differentially by measuring the radiation from both the sun and a calibrated tungsten

ribbon lamp with an equatorially-mounted Cassegrain telescope and double monochromator. During the observations the Cassegrain telescope was switched back and forth between the sun and the comparison lamp at regular intervals not exceeding 15 minutes. Neutral density filters were mounted in front of the sun in order to reduce the intensity difference between the sun and the lamp. The transmission of each filter set was redetermined every day.

The filament of a calibrated tungsten ribbon lamp was placed at the exact focus of a large collimating mirror that was aimed at the Cassegrain telescope during the comparison lamp measurements. The reflectivity of the collimating mirror was measured as a function of wavelength on several occasions during each observing run. The two tungsten ribbon lamps that served alternately as the comparison source were both calibrated at the Happel Laboratory of the Heidelberg Observatory. A detailed description of the black body and the procedure that was used to calibrate it against a gold point standard can be found in Mehlretter (1960).

Atmospheric extinction coefficients were determined directly at a number of preselected wavelengths each day. These extinction coefficients were used to extrapolate the solar intensity measures to zero airmass. The extinction coefficients at most wavelengths were interpolated from the extinction coefficients actually measured.

Labs and Neckel (1962) described the techniques that they used to obtain 132 absolute intensity measures from 4010.0 to 6569.0 Å. Labs and Neckel (1963) then presented 32 additional measures of the solar intensity from 6389.0 to 12480.0 Å. The passbands for all of these measures were 20.0 Å wide and almost perfectly rectangular. Regions in the solar spectrum that were strongly affected by atmospheric absorption were not investigated.

Labs and Neckel (1967) published a complete revision of their original intensity measures from 4010.0 to 12480.0 Å. Included as part of this revision were 44 new measures that were taken from 3287.9 to 4127.1 Å. The passbands for these new measures were 20.5 Å wide. The revision of the original measures from 4010.0 to 12480.0 Å resulted from intercomparisons which had been made with a number of standard lamps that had been calibrated at Heidelberg and several other laboratories from 1958 through 1965. These intercomparisons indicated that lamp intensities based on the Heidelberg black body were systematically too high relative to the radiation standards at the other laboratories. Labs and Neckel (1967) therefore recomputed all of their absolute intensity measures using lamp intensities that were uniformly reduced by 1%. Labs and Neckel (1968) later republished these results using a revised gold point of 1337.58 °K and a new value of c_1 . Labs and Neckel (1970) then published a differential correction scheme that

could be used to bring these data into complete agreement with the IPTS-68. Table 6.1 gives a simplified listing of the physical constants that were assumed in each paper of this series.

Table 6.1. Physical constants for the absolute intensity measures of Labs and Neckel.

Reference	$2c_1$ (erg·cm ² ·s ⁻¹)	c_2 (cm·K)	T_{Au} (K)
1962	1.1970×10^{-5}	1.4380	1336.20
1963	1.1907×10^{-5}	1.4380	1336.20
1967	1.1907×10^{-5}	1.4380	1336.20
1968	1.1910×10^{-5}	1.4380	1337.58
1970	1.1910×10^{-5}	1.4388	1337.58

Several of the disk-center absolute intensity measures of Labs and Neckel (1967) were used in calibrating the solar models in this research. The passbands for these measures were located in regions of the spectrum that were believed to be relatively free from blanketing by solar and terrestrial absorption lines. The atmospheric extinction in each of the selected passbands had also been accurately measured during the observations.

The intensity at the central wavelength in each calibration passband was obtained in this research by

dividing the published integrated intensity by the width of the passband. These intensities were then converted from the IPTS-48 to the IPTS-68 as follows:

$$I^{68} = I^{48} \cdot \frac{1.1910}{1.1907} \cdot \frac{\exp(1.4380/(\lambda \cdot 2500.0)) - 1}{\exp(1.4388/(\lambda \cdot 2503.6)) - 1}.$$

The resulting intensities are listed as I_λ and I_ν in Table 6.2. A revised temperature of 2503.6 K was adopted for the Heidelberg black body since it was originally calibrated against a gold point standard at several wavelengths near 5700 Å.

The observational absolute intensities in Table 6.2 were corrected for absorption lines using high resolution spectra that were taken with the McMath Solar Telescope and the Main Spectrometer. These spectra were fitted with a parabolic solar continuum for a range of several hundred angstroms about each observational passband. The program chose the solar continuum in each region by minimizing the area between the parabola and the spectrum without allowing the parabola to fall below the spectrum at any point over the range of the fit. The spectrum was then normalized by adjusting the fitted continuum to a value of unity at each wavelength. A line blanketing coefficient η for each passband was calculated by a direct integration of the normalized solar spectrum. The continuum intensity in each passband was then computed by dividing the observed

Table 6.2. Absolute solar intensities for the passbands used by Labs and Neckel.

λ (Å)	Observed absolute intensity		Line blanketing		Corrected continuum intensity	
	I_λ	I_ν			I'_λ	I'_ν
	$(\frac{\text{erg cm}^{-2} \text{s}^{-1}}{\text{ster cm}})$	$(\frac{\text{erg cm}^{-2} \text{s}^{-1}}{\text{ster Hz}})$	Present research	L & N (1968)	$(\frac{\text{erg cm}^{-2} \text{s}^{-1}}{\text{ster cm}})$	$(\frac{\text{erg cm}^{-2} \text{s}^{-1}}{\text{ster Hz}})$
6080	$.3102 \times 10^{15}$	$.3825 \times 10^{-4}$.0243	.0210	$.3179 \times 10^{15}$	$.3920 \times 10^{-4}$
6239	$.2955 \times 10^{15}$	$.3837 \times 10^{-4}$.0513	.0330	$.3115 \times 10^{15}$	$.4045 \times 10^{-4}$
6399	$.2874 \times 10^{15}$	$.3925 \times 10^{-4}$.0382	.0270	$.2988 \times 10^{15}$	$.4081 \times 10^{-4}$
6621	$.2772 \times 10^{15}$	$.4053 \times 10^{-4}$.0108	.0070	$.2802 \times 10^{15}$	$.4098 \times 10^{-4}$
7465	$.2216 \times 10^{15}$	$.4119 \times 10^{-4}$.0171	.0130	$.2254 \times 10^{15}$	$.4191 \times 10^{-4}$
8465	$.1731 \times 10^{15}$	$.4137 \times 10^{-4}$.0291	.0160	$.1783 \times 10^{15}$	$.4261 \times 10^{-4}$
9815	$.1272 \times 10^{15}$	$.4087 \times 10^{-4}$.0379	.0100	$.1322 \times 10^{15}$	$.4249 \times 10^{-4}$

intensity by $1 - \eta$. The line blanketing coefficients and the continuum intensities I'_λ and I'_ν are given in Table 6.2.

There are several potential sources of error in using the line blanketing coefficients from the high resolution spectra to calculate continuum intensities from the observed disk-center intensity measures. Atmospheric absorption lines are largely eliminated through the extinction corrections. Correcting the observed intensities for line blanketing thus results in a second correction for the atmospheric lines in each passband. Solar lines at either end of the instrumental passband will also be inaccurately accounted for in computing the line blanketing. A proper treatment would require an exact knowledge of the original instrumental passband. The line blanketing coefficients that were calculated from the high resolution scans are accurate to only $\pm 10\%$ as a result of these uncertainties. Since most of the line blanketing coefficients are quite small, the overall effect of this error on the continuum intensities is actually fairly insignificant.

Labs and Neckel (1968) also published line blanketing coefficients for each of their observational passbands. Above 5500 \AA these line blanketing coefficients were obtained from a direct planimetry of published solar atlases. Coefficients for the passbands that were used in calibrating the solar models are shown in Table 6.2. In most cases these line blanketing coefficients are somewhat

smaller than those that were derived from the high resolution spectra. This discrepancy is probably caused by the large uncertainty that is inherent in trying to determine the level of the continuum in published atlas spectra.

According to Labs and Neckel (1968) the standard error associated with their absolute intensity measures is $\pm 1.5\%$. Systematic errors that might affect the overall calibration of the measures were thought to be less than $\pm 2\%$. Any solar model that produces disk-center continuum intensities that are more than a few per cent from those in Table 6.2 should probably be rejected.

6.3 Absolute Intensity Observations of Saiedy and Goody

A well-calibrated solar absolute intensity measure at 111000 \AA was published by Saiedy and Goody (1959). Two similar measures of the solar absolute intensity at 86300 and 120200 \AA were later published by Saiedy (1960). The solar observations that were used in deriving these absolute intensity measures were taken at the Ascot Field Station of the Department of Meteorology, Imperial College during 1958 and 1959. A sidereostat was used with a parabolic primary mirror to form an image of the sun on the entrance slit of a grating double monochromator in these observations. A chopping wheel in front of the double monochromator modulated the incoming radiation at 11 Hz . The infrared radiation from the double monochromator was

detected with a Golay cell which was coupled to a phase-sensitive rectifier and a Honeywell-Brown recorder.

The sidereostat was rotated into a position where radiation was sent to the double monochromator from a carefully regulated black body reference source at 1300 °K between individual observations of the sun. A parabolic mirror was used in the reference source measurements to send a collimated beam of radiation from the black body to the sidereostat. Except for the additional reflection at this mirror and the change in the angle of reflection at the sidereostat, the radiation from the black body followed the same optical path as the radiation from the sun. The reflectivity of the collimating mirror and the angular dependence of the reflectivity of the sidereostat were both calibrated using a Nernst filament and a special optical system with the double monochromator. Polarization effects were not included in the measurements. The large intrinsic intensity difference between the sun and the black body was minimized in the observations by placing a second sector wheel in front of the double monochromator during the observations of the sun. This sector wheel was calibrated geometrically and interrupted the incoming beam of radiation at 100 Hz. This sector wheel had no effect on the linearity of the measurements.

The final recorder deflections were used with the various instrumental calibrations to obtain individual

measures of the solar intensity. A least-squares linear fit to each series of intensity measures was then used to extrapolate the observations to zero airmass. A small correction was also made for the effects of limb darkening. The final absolute intensity measures are listed in Table 6.3. These measures are based on a revised black body temperature of 1301.32 K.

Table 6.3. Absolute intensity measures of Siedy and Goody.

λ (Å)	Observed absolute intensity	
	I_λ	I_ν
	$\left(\frac{\text{erg cm}^{-2} \text{s}^{-1}}{\text{ster cm}}\right)$	$\left(\frac{\text{erg cm}^{-2} \text{s}^{-1}}{\text{ster Hz}}\right)$
86300	6.543×10^{10}	1.625×10^{-6}
111000	2.412×10^{10}	$.9914 \times 10^{-6}$
120200	1.777×10^{10}	$.8564 \times 10^{-6}$

6.4 Absolute Intensity Observations of Houtgast

Houtgast (1970) described a series of absolute intensity measures that were obtained during July and August, 1960 with the Snow Spectrometer at Mt. Wilson. These measures covered high points in the solar spectrum from 2935.3 to 4087.4 Å. A coelostat and a large optical flat were used to direct solar radiation to the primary

mirror of the telescope during observations of the sun. A calibrated tungsten ribbon lamp and a large auxiliary flat were used during the comparison source measurements. The comparison lamp was located in front of and slightly to the side of the spectrometer. Light from the filament reflected off the primary and travelled to the auxiliary flat. The reflected radiation from the flat then travelled back to the primary mirror and was reimaged on the slit of the spectrometer.

Comparison lamp measurements were usually taken first at all wavelengths. Tracings of the solar spectrum were then recorded at as many wavelengths as possible. A final series of comparison lamp measurements were taken immediately after the solar observations. Because of weather conditions, the entire observing sequence was finished on only two occasions. Relative measurements were obtained on several additional days.

The reflectivities of the mirrors were measured in a separate series of measurements that incorporated an extra flat that was identical to that which was used in the comparison lamp measurements. Polarization effects were not investigated directly although a 3% loss was expected during the observations of the sun. This was balanced by a 4% loss that was caused by placing the lamp filament in front of the spectrometer during the comparison source measurements. Uncertainties were also introduced in

calibrating the ribbon lamp and in determining the solar intensity outside the earth's atmosphere. The cumulative effects of these and other errors were estimated to range from $\pm 18\%$ at 3000 \AA to $\pm 8\%$ at 4000 \AA .

The extinction at each wavelength was based on a set of extinction coefficients that were obtained by Dunkelmann and Scolnik (1959) at Mt. Lemmon on October 4, 1959. Houtgast used these coefficients for his reductions after he increased the Rayleigh scattering component of the extinction by 9% in order to account for the airmass difference between Mt. Wilson and Mt. Lemmon. The ozone component of the extinction was assumed to be the same at both locations. Although this procedure is acceptable in principle, the results are difficult to verify. Houtgast (1970) claimed that the observations at Mt. Wilson were compatible with the corrected extinction coefficients from Mt. Lemmon. The estimates of the extinction at Mt. Wilson, however, were frequently based on only two observations of the sun at each wavelength.

Most conventional solar models produce intensities that are almost 50% higher than those of Houtgast (1970) near 3000 \AA . Since the observations of Houtgast provide evidence of a missing opacity source in the ultraviolet, it is important to know whether the observational errors could be large enough to account for this discrepancy. Labs and Neckel (1967) measured the solar intensity in a passband

from 3287.9 to 3308.4 Å. High resolution spectra taken with the McMath Solar Telescope indicate that $\eta = 0.31$ in this passband. When this line blanketing is taken into account, the intensity of the apparent continuum in this spectral region is found to be 5% above that measured by Houtgast (1970) in the window at 3300.3 Å. Both sets of observations thus agree to well within the quoted estimates. Errors as large as 50% are quite unlikely in view of the excellent agreement between the two independent sets of observations. The absolute intensity measures of Houtgast (1970) at 3204.7 and 4019.7 Å were used to evaluate the ultraviolet predictions of the solar models in this research.

CHAPTER 7

THE SOLAR MODELS

A series of continuum solar models were computed with the SOURCE model atmosphere program in this research. Details of this program have been published by Gingerich (1964); Carbon and Gingerich (1969); Carbon, Gingerich, and Latham (1969); and Gingerich et al. (1971). A description of the specific version of the program that was used in computing the solar models is given in Section 7.1.

Limb darkening observations from 3033.27 to 7296.75 Å have recently been taken by Pierce and Slaughter (1977) with the McMath Solar Telescope. Limb darkening measures from these observations were used in deriving several of the solar models in this research. A brief discussion of the limb darkening observations of Pierce and Slaughter (1977) is therefore provided in Section 7.2.

Techniques for fitting the solar models to the observations are described in Section 7.3. One-component models of the solar atmosphere are then discussed in Section 7.4. A discussion of two-component models follows in Section 7.5. A number of basic conclusions that can be drawn from the solar models are presented in Section 7.6.

7.1 Description of the Model Atmosphere Computations

The temperature structure of the solar atmosphere can be studied with theoretical models. The emergent intensity at any angle to the surface of a plane-parallel atmosphere can be calculated as

$$I_{\lambda}(\mu) = \int_0^{\infty} S_{\lambda}(\tau_{\lambda}) e^{-\tau_{\lambda}/\mu} \frac{d\tau_{\lambda}}{\mu},$$

where $S_{\lambda}(\tau_{\lambda})$ is the source function and τ_{λ} is the monochromatic optical depth along a normal to the surface. The integral is normally performed as a finite sum over a large number of depths in the atmosphere. The source function $S_{\lambda}(\tau_{\lambda})$ is the ratio of the emissivity to the absorptivity at each depth. The physical conditions at each point in the atmosphere depend only on the surface gravity, the chemical composition, and the local temperature if one assumes hydrostatic equilibrium and LTE. It is therefore possible to determine the temperature structure of the solar atmosphere by empirically matching the predictions of a theoretical model to actual observations of the solar intensity once one knows the surface gravity and the chemical composition of the atmosphere.

A series of continuum solar models were computed with the SOURCE model atmosphere program. The temperatures in each of these models were defined at regular intervals in the logarithm of the continuous opacity at 5000 Å. There

were 20 steps per decade of optical depth from $\log \tau = -8.0$ to $\log \tau = +1.4$ in each model. The He/H ratio by number was set at 1/10. All other atomic abundances except iron were taken from Lambert (1968) and Lambert and Warner (1968). The iron abundance was derived by Garz et al. (1969). The elemental abundances are given in Table 7.1. The level populations of all atomic and molecular species including hydrogen were assumed to be in LTE. Hydrostatic equilibrium was also assumed in all of the models.

Contributions to the opacity from H, H^- , H_2^+ , H_2^- , He^- , Rayleigh scattering, electron scattering, and the metals were included in the computations. References for the opacity representations in the program are given in Table 7.2. The references in this table are listed in chronological order. The primary reference for the theoretical work is therefore listed first. Scattering contributions to the source function were computed at nineteen steps in the atmosphere. The scattering at all other steps was found by interpolation. The scattering contributions to the source function were small throughout most of the atmosphere.

Since H^- is the dominant opacity source in both the visible and the infrared throughout most of the photosphere, errors in the computation of the bound-free or free-free absorption coefficient of H^- could significantly affect the models. Geltman (1962) computed the H^- bound-free

Table 7.1. Elemental abundances by number in the model atmosphere program.

Element	Abundance
H	1.000×10^0
He	1.000×10^{-1}
C	3.548×10^{-4}
N	8.511×10^{-5}
O	5.888×10^{-4}
Na	1.514×10^{-6}
Mg	3.020×10^{-5}
Al	2.512×10^{-6}
Si	3.548×10^{-5}
S	1.622×10^{-5}
K	1.122×10^{-7}
Ca	2.138×10^{-6}
Fe	3.162×10^{-5}

Table 7.2. References for the opacity representations in the model atmosphere program.

Opacity source	Reference
H	Menzel and Pekeris (1935) Burgess (1958) Karsas and Latter (1961) Gingerich (1964) Carbon and Gingerich (1969)
H^- bound-free	Geltman (1962) Gingerich (1964) Carbon and Gingerich (1969)
H^- free-free	Stilly and Callaway (1970) Kurucz (1970)
C	Peach (1967) Carbon and Gingerich (1969)
Mg, Si	Peach (1970) Kurucz (1970)
H_2^+	Bates (1951, 1952) Bates, Ledsham, and Steward (1953) Gingerich (1964) Carbon and Gingerich (1969)
H_2^-	Somerville (1964) Dalgarno and Lane (1966) Carbon et al. (1969)
He^- free-free	John (1968) Carbon et al. (1969)
H Rayleigh	Dalgarno (1962) Gingerich (1964) Carbon and Gingerich (1969)
H_2 Rayleigh	Dalgarno and Williams (1962) Gingerich (1964)

absorption coefficient using a seventy-parameter bound-state wave function and a variationally determined free-state wave function. Doughty, Fraser, and McEachran (1966) and Bell and Kingston (1967) have also calculated the bound-free absorption coefficient of H^- . The velocity results of Geltman (1962) and Doughty et al. (1966) agree to $\pm 5\%$ from 300 to 13000 Å. The velocity results of Bell and Kingston (1967) also agree to $\pm 20\%$ with those of Geltman (1962) over the same spectral range. Errors larger than $\pm 20\%$ in the H^- bound-free absorption coefficient should therefore be confined to regions of the spectrum that are outside the range from 3000 to 13000 Å. Stilly and Callaway (1970) computed the free-free absorption coefficient of H^- using polarized orbital theory to obtain the continuum state of the external electron. The length and velocity results in their formulation agree to $\pm 10\%$ beyond 10000 Å. Since the results of Stilly and Callaway (1970) also agree very well with those of Doughty and Fraser (1966) and Bell, Kingston, and McIlveen (1975), systematic errors in the H^- free-free absorption coefficient are probably less than $\pm 10\%$ beyond 10000 Å.

Departures from LTE can significantly affect the solar radiation field. Vernazza, Avrett, and Loeser (1976) developed an empirical model of the solar photosphere and low chromosphere in which they explicitly solved the statistical equilibrium and radiative transfer equations for

H, H^- , C I, and Si I. Non-LTE effects in hydrogen and carbon were generally found to be negligible except in the chromosphere. Non-LTE effects in silicon, however, were found to be important in the upper levels of the photosphere and in the temperature minimum. These non-LTE effects may have a slight influence on the limb darkening measures at 85636.32 and 104077.55 Å. Small changes in the upper levels of the photosphere, however, cannot significantly affect the limb darkening measures at any of the other observational wavelengths. Non-LTE effects are therefore unimportant in the layers of the solar atmosphere that are of primary interest in this study.

7.2 Limb Darkening Observations of Pierce and Slaughter

Pierce and Slaughter (1977) have recently published several tables which can be used to reconstruct observational profiles of the solar limb darkening at a number of wavelengths from 3033.27 to 7297.75 Å. The numerical coefficients that are listed in these tables were derived from least-squares polynomial fits to drift scans that were taken with the Main McMath Solar Telescope during 1974 and 1975.

Pierce and Slaughter (1977) used the Main Spectrometer in double pass for their observations. The background in each drift scan was determined by closing the intermediate shutter of the spectrometer for a short period of

time when the solar image was about nine-tenths of a solar radius away from the entrance aperture of the spectrometer. Two additional closures of the intermediate shutter as the sun actually passed over the entrance slit were used to determine the amount of stray light that was scattered inside the spectrometer. This stray light was then subtracted out of each scan by assuming that it was directly proportional to the solar intensity at each point on the disk. The inflection points that occurred on opposite sides of the solar profiles were used to define the solar limbs in the data reductions. A least-squares polynomial fit to a series of normal points across the solar disk was used to derive a final limb darkening curve at each wavelength. A fifth-degree polynomial in μ was found to be the most accurate. No corrections for diffraction, atmospheric seeing, or atmospheric scattering were made from disk center to $\mu = 0.10$. Probable errors over this range were generally less than ± 0.005 . Most, but not all, of the observations were taken in relatively clean windows of the solar spectrum.

7.3 Procedure for Testing the Solar Models

A large number of solar models were investigated in this research. A few of the more successful models are discussed in the remaining sections of this chapter. The temperatures in most of these models were adjusted until the limb darkening and absolute intensity predictions of the

model atmosphere program matched the observational measures as well as possible. Limb darkening residuals for each solar model were calculated by subtracting the observational measures of the limb darkening from the limb darkening measures that were derived from the program. Each positive residual indicated that the model limb darkening was too high; while each negative residual indicated that the model limb darkening was too low. Observational measures of the limb darkening in the infrared were computed from the quadratic coefficients in Table 5.19. Observational measures of the limb darkening at 3204.68, 4019.70, 4615.10, 4929.05, 5256.35, 6109.75, and 6694.00 Å were computed from the coefficients of the fifth-degree polynomials in μ that were published by Pierce and Slaughter (1977). High resolution atlas spectra indicated that these particular wavelengths were relatively unaffected by solar and terrestrial absorption lines. Ratios of the predicted absolute intensity at disk center to the observed absolute intensity at disk center were also calculated at several wavelengths in each model.

The temperatures at various depths in the solar models were adjusted up or down in an effort to minimize the absolute values of the limb darkening residuals at each wavelength. An effort was also made to keep the absolute intensity ratios as close as possible to one. At most wavelengths the solar limb darkening can be approximated by

an equation of the form

$$I_{\lambda}(\mu)/I_{\lambda}(1.0) = a + b \mu.$$

The source function under such conditions can be expressed as

$$S_{\lambda}(\tau_{\lambda}) = a I_{\lambda}(1.0) + b I_{\lambda}(1.0) \tau_{\lambda}.$$

The solar limb darkening at 4500 Å is approximately equal to $0.25 + 0.75 \mu$, and the source function can be expressed as

$$S_{\lambda}(\tau_{\lambda}) = 0.25 I_{\lambda}(1.0) + 0.75 I_{\lambda}(1.0) \tau_{\lambda}.$$

Starting with this expression one can show that a $\pm 5\%$ error in the source function of a proposed solar model at all depths above $\tau_{\lambda} = 0.099$ or a $\mp 5\%$ error at all depths below $\tau_{\lambda} = 2.44$ could be responsible for a limb darkening residual of ± 0.0050 at $\mu = 0.20$. At 22000 Å the limb darkening is approximately equal to $0.75 + 0.25 \mu$, and the source function can be expressed as

$$S_{\lambda}(\tau_{\lambda}) = 0.75 I_{\lambda}(1.0) + 0.25 I_{\lambda}(1.0) \tau_{\lambda}.$$

A limb darkening residual of ± 0.0020 at $\mu = 0.20$ at this wavelength could be caused by a $\pm 2\%$ error in the source function at all depths above $\tau_{\lambda} = 0.100$ or by a $\mp 2\%$ error at all depths below $\tau_{\lambda} = 2.43$. A ± 40 K error at 5000 K or a ± 78 K error at 7000 K would be large enough to produce a $\pm 5\%$ error in the source function at 4500 Å. A ± 57 K error at 5000 K or a ± 93 K error at 7000 K would be sufficient to

produce a $\pm 2\%$ error in the source function at 22000 Å. As a whole, these results indicate that the residuals in both the visible and the infrared will be smaller than the observational errors as long as the temperature errors in a proposed model are less than ± 40 K above $\tau_\lambda = 0.10$ and less than ± 80 K below $\tau_\lambda = 2.43$.

7.4 One-Component Models of the Solar Atmosphere

The HSRA was recomputed with the version of the SOURCE model atmosphere program that was described in Section 7.1. The physical parameters of this model are given in Table 7.3 and are slightly different from those that were published by Gingerich et al. (1971). Most of the differences are extremely small and result from changes in the opacity representations that have been incorporated into the current version of the model atmosphere program.

The limb darkening residuals for the HSRA are given in Table 7.4. The absolute intensity ratios for the HSRA are listed with those of other one-component models in Table 7.9 (p. 167). The largest limb darkening residuals occur at 3204.68, 16222.00, and 16513.18 Å. The residuals at 3204.68 Å are positive; while those at 16222.00 and 16513.18 Å are negative. Since optical depth unity at each of these wavelengths lies below optical depth unity at 5000 Å, most of the radiation at all three wavelengths comes from deep within the photosphere. The positive residuals at 3204.68 Å

Table 7.3. Physical parameters of the HSRA.

Log τ_{5000} Å	T (K)	Log P_{gas} (dyne/cm ²)	Log P_{e} (dyne/cm ²)	Log density (g/cm ³)	Log depth (cm)
-5.0	5300	1.668	-1.205	-9.864	7.947
-4.9	5170	1.885	-1.254	-9.636	7.916
-4.8	5040	2.074	-1.314	-9.436	7.888
-4.7	4910	2.242	-1.370	-9.256	7.862
-4.6	4790	2.392	-1.398	-9.095	7.838
-4.5	4660	2.524	-1.400	-8.952	7.817
-4.4	4530	2.636	-1.365	-8.827	7.798
-4.3	4400	2.729	-1.317	-8.722	7.782
-4.2	4280	2.808	-1.276	-8.630	7.769
-4.1	4200	2.879	-1.240	-8.551	7.757
-4.0	4170	2.946	-1.195	-8.481	7.745
-3.9	4175	3.011	-1.139	-8.417	7.734
-3.8	4190	3.073	-1.080	-8.356	7.722
-3.7	4205	3.135	-1.022	-8.296	7.711
-3.6	4225	3.195	-.964	-8.237	7.699
-3.5	4250	3.255	-.903	-8.180	7.687
-3.4	4280	3.314	-.842	-8.124	7.675
-3.3	4305	3.373	-.783	-8.068	7.663
-3.2	4330	3.431	-.724	-8.013	7.650
-3.1	4355	3.488	-.666	-7.958	7.636
-3.0	4380	3.546	-.608	-7.903	7.623
-2.9	4405	3.603	-.551	-7.848	7.609
-2.8	4430	3.660	-.494	-7.794	7.594
-2.7	4460	3.716	-.435	-7.740	7.579
-2.6	4490	3.773	-.376	-7.686	7.563
-2.5	4525	3.829	-.316	-7.633	7.547
-2.4	4550	3.885	-.260	-7.580	7.529
-2.3	4575	3.941	-.204	-7.526	7.511
-2.2	4600	3.997	-.148	-7.472	7.493
-2.1	4630	4.053	-.090	-7.419	7.473
-2.0	4660	4.109	-.033	-7.366	7.452
-1.9	4690	4.165	.025	-7.313	7.430
-1.8	4720	4.220	.082	-7.260	7.407
-1.7	4750	4.276	.139	-7.207	7.382
-1.6	4790	4.332	.200	-7.155	7.356
-1.5	4840	4.387	.264	-7.104	7.327
-1.4	4895	4.443	.329	-7.054	7.297
-1.3	4950	4.498	.395	-7.003	7.263
-1.2	5010	4.554	.462	-6.953	7.227
-1.1	5080	4.609	.533	-6.904	7.187

Table 7.3.--Continued

Log τ_{5000} Å	T (K)	Log P_{gas} (dyne/cm ²)	Log P_e (dyne/cm ²)	Log density (g/cm ³)	Log depth (cm)
-1.0	5160	4.664	.608	-6.856	7.142
-.9	5240	4.718	.685	-6.808	7.091
-.8	5330	4.772	.767	-6.761	7.034
-.7	5430	4.825	.857	-6.716	6.968
-.6	5540	4.876	.956	-6.674	6.892
-.5	5650	4.925	1.060	-6.634	6.801
-.4	5765	4.971	1.170	-6.596	6.691
-.3	5890	5.015	1.290	-6.562	6.550
-.2	6035	5.055	1.428	-6.532	6.355
-.1	6200	5.091	1.582	-6.508	6.033
.0	6390	5.123	1.755	-6.498	0.000
.1	6610	5.151	1.947	-6.477	5.982
.2	6860	5.174	2.154	-6.470	6.255
.3	7140	5.194	2.372	-6.468	6.403
.4	7440	5.210	2.589	-6.470	6.499
.5	7750	5.223	2.797	-6.475	6.569
.6	8030	5.235	2.973	-6.479	6.624
.7	8290	5.245	3.127	-6.483	6.669
.8	8520	5.255	3.256	-6.486	6.709
.9	8710	5.265	3.358	-6.487	6.747
1.0	8880	5.275	3.447	-6.487	6.782
1.1	9050	5.285	3.533	-6.486	6.816
1.2	9220	5.296	3.616	-6.485	6.850
1.3	9390	5.307	3.697	-6.484	6.882
1.4	9560	5.318	3.774	-6.482	6.914

Table 7.4. Residuals for the HSRA.

λ (Å)	Log μ						
	-.10	-.20	-.30	-.40	-.50	-.60	-.70
3204.68	+.0159	+.0255	+.0305	+.0342	+.0363	+.0361	+.0335
4019.70	-.0011	-.0019	-.0022	-.0006	+.0020	+.0042	+.0050
4615.10	-.0053	-.0095	-.0110	-.0096	-.0069	-.0046	-.0041
4929.05	-.0050	-.0087	-.0105	-.0102	-.0084	-.0059	-.0037
5256.35	-.0008	-.0049	-.0051	-.0046	-.0039	-.0025	-.0001
6109.75	-.0023	-.0043	-.0043	-.0035	-.0023	-.0007	+.0007
6694.00	-.0068	-.0066	-.0059	-.0060	-.0063	-.0057	-.0045
10840.10	-.0029	-.0047	-.0052	-.0048	-.0045	-.0049	-.0064
10854.00	-.0031	-.0050	-.0055	-.0052	-.0048	-.0051	-.0066
10865.00	-.0033	-.0053	-.0059	-.0057	-.0054	-.0057	-.0073
12466.63	-.0033	-.0057	-.0069	-.0071	-.0067	-.0065	-.0067
12505.51	-.0031	-.0053	-.0065	-.0067	-.0065	-.0065	-.0069
16222.00	-.0048	-.0093	-.0132	-.0162	-.0183	-.0194	-.0197
16513.18	-.0048	-.0093	-.0133	-.0163	-.0185	-.0199	-.0205
21855.59	-.0030	-.0054	-.0069	-.0078	-.0080	-.0077	-.0071
21907.47	-.0025	-.0048	-.0063	-.0071	-.0074	-.0072	-.0069
23121.03	-.0027	-.0047	-.0061	-.0069	-.0071	-.0070	-.0069
23127.19	-.0028	-.0050	-.0065	-.0073	-.0075	-.0073	-.0069
23132.73	-.0027	-.0049	-.0064	-.0071	-.0073	-.0070	-.0065
38839.36	-.0006	-.0011	-.0016	-.0019	-.0025	-.0032	-.0042
38862.02	-.0007	-.0015	-.0020	-.0026	-.0033	-.0043	-.0056
46142.57	-.0003	-.0009	-.0015	-.0023	-.0033	-.0045	-.0060
85636.32	-.0017	-.0034	-.0049	-.0060	-.0070	-.0078	-.0083
104007.55	-.0022	-.0041	-.0057	-.0069	-.0079	-.0088	-.0095

suggest that the temperatures below optical depth unity rise too slowly; while the negative residuals at 16222.00 and 16513.18 Å indicate that these temperatures rise too rapidly. The temperature gradient in the deep layers of the HSRA is thus too low to produce the dramatic limb darkening that is observed at short wavelengths and too high to account for the rather mild limb darkening that is observed near the H^- opacity minimum at 16400 Å. The absolute intensities at 3204.7 and 4019.7 Å are also quite high; while those at longer wavelengths tend to be too low. Since similar discrepancies in the deep layers of the photosphere occur in one form or another with virtually all of the solar models that have been presented in recent years, these problems are not restricted solely to the HSRA. It will be shown in later sections of this chapter that many of the discrepancies in the deep layers of the photosphere can be explained by line blanketing and by the temperature fluctuations that are associated with the solar granulation.

An effort was initially made to develop a one-component solar model that would deviate only slightly from the HSRA and still fit the new infrared limb darkening measures. The atmospheric model that was achieved in this effort is shown as Model 1 in Figure 7.1. The physical parameters of Model 1 at regular intervals in $\log \tau$ are listed in Table 7.5. Model 1 has a minimum temperature of 4136 K at $\log \tau = -4.0$. Temperatures from $\log \tau = -3.6$ to

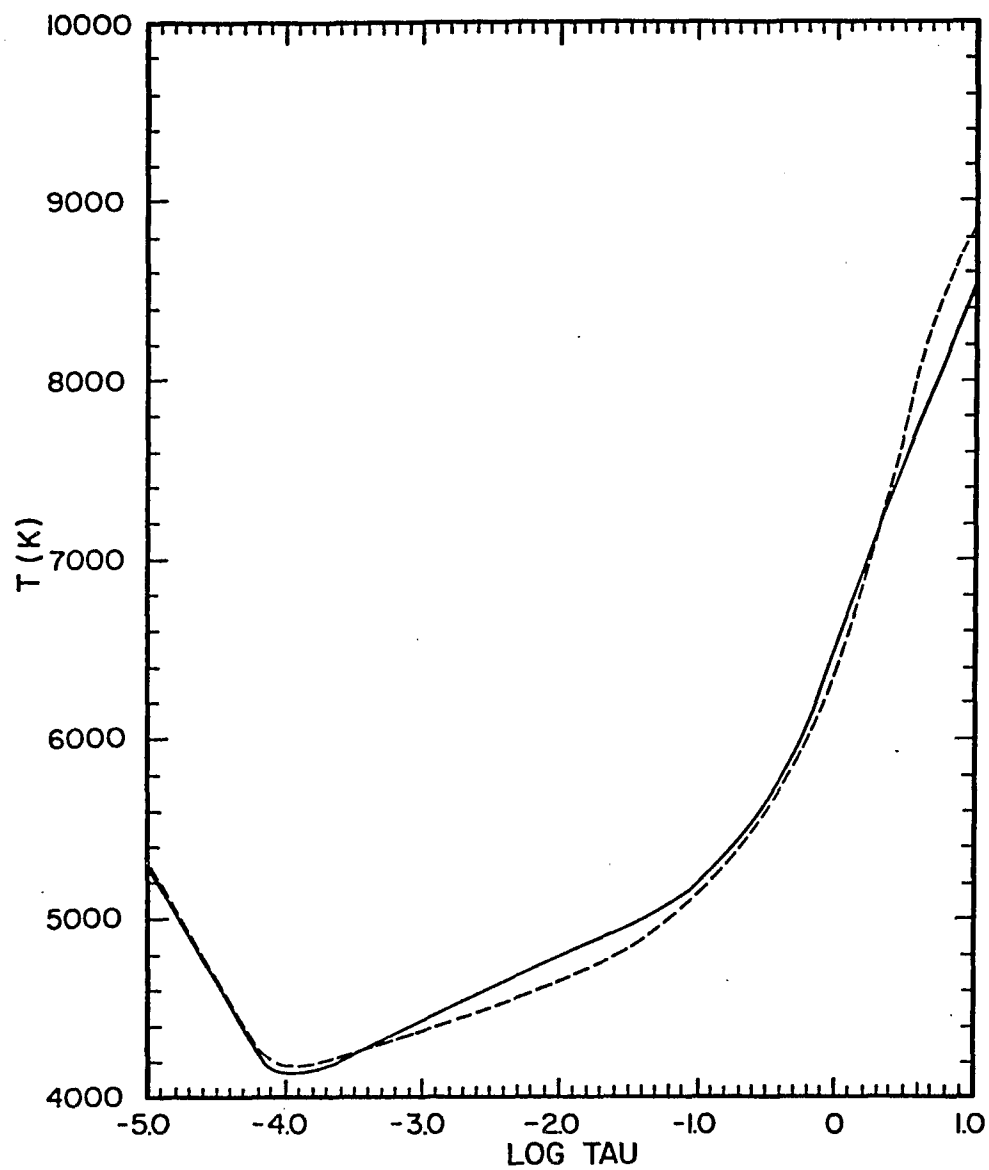


Figure 7.1. Solar models: (a) Model 1, —; (b) HSRA, ---.

Table 7.5. Physical parameters of Model 1

Log τ_{5000} Å	T (K)	Log P_{gas} (dyne/cm ²)	Log P_{e} (dyne/cm ²)	Log density (g/cm ³)	Log depth (cm)
-5.0	5300	1.669	-1.205	-9.863	7.948
-4.9	5168	1.886	-1.256	-9.635	7.917
-4.8	5036	2.075	-1.318	-9.435	7.889
-4.7	4904	2.243	-1.376	-9.254	7.863
-4.6	4772	2.395	-1.412	-9.091	7.839
-4.5	4640	2.527	-1.410	-8.947	7.817
-4.4	4512	2.638	-1.369	-8.823	7.799
-4.3	4384	2.730	-1.319	-8.719	7.783
-4.2	4256	2.808	-1.283	-8.628	7.770
-4.1	4160	2.879	-1.256	-8.547	7.758
-4.0	4136	2.946	-1.210	-8.478	7.747
-3.9	4142	3.010	-1.154	-8.414	7.736
-3.8	4156	3.073	-1.096	-8.353	7.724
-3.7	4178	3.135	-1.035	-8.293	7.713
-3.6	4208	3.195	-.971	-8.236	7.701
-3.5	4244	3.255	-.906	-8.180	7.690
-3.4	4280	3.314	-.842	-8.124	7.677
-3.3	4316	3.372	-.778	-8.070	7.665
-3.2	4352	3.431	-.715	-8.015	7.652
-3.1	4388	3.488	-.653	-7.961	7.639
-3.0	4424	3.546	-.591	-7.907	7.625
-2.9	4460	3.603	-.529	-7.853	7.611
-2.8	4496	3.660	-.468	-7.800	7.596
-2.7	4532	3.717	-.407	-7.746	7.580
-2.6	4568	3.774	-.346	-7.693	7.564
-2.5	4604	3.830	-.286	-7.640	7.548
-2.4	4640	3.886	-.226	-7.587	7.530
-2.3	4676	3.943	-.166	-7.534	7.512
-2.2	4712	3.999	-.106	-7.481	7.492
-2.1	4748	4.055	-.047	-7.428	7.472
-2.0	4784	4.111	.013	-7.376	7.451
-1.9	4820	4.167	.072	-7.323	7.428
-1.8	4856	4.222	.131	-7.271	7.404
-1.7	4892	4.278	.190	-7.218	7.378
-1.6	4928	4.334	.249	-7.166	7.351
-1.5	4964	4.389	.308	-7.114	7.321
-1.4	5000	4.444	.367	-7.061	7.290
-1.3	5042	4.499	.428	-7.010	7.255
-1.2	5092	4.555	.492	-6.959	7.218
-1.1	5150	4.609	.560	-6.909	7.176

Table 7.5.--Continued

Log τ_{5000} Å	T (K)	Log P_{gas} (dyne/cm ²)	Log P_e (dyne/cm ²)	Log density (g/cm ³)	Log depth (cm)
-1.0	5216	4.664	.631	-6.860	7.130
-.9	5290	4.718	.706	-6.812	7.078
-.8	5372	4.771	.786	-6.766	7.019
-.7	5462	4.824	.873	-6.721	6.951
-.6	5560	4.874	.967	-6.678	6.871
-.5	5672	4.923	1.072	-6.638	6.776
-.4	5800	4.968	1.193	-6.602	6.660
-.3	5954	5.010	1.336	-6.571	6.512
-.2	6134	5.047	1.503	-6.547	6.311
-.1	6328	5.080	1.680	-6.529	5.986
.0	6528	5.108	1.858	-6.514	0.000
.1	6728	5.133	2.030	-6.503	5.943
.2	6928	5.155	2.195	-6.493	6.226
.3	7128	5.175	2.353	-6.486	6.387
.4	7328	5.193	2.504	-6.480	6.498
.5	7528	5.210	2.648	-6.475	6.584
.6	7728	5.226	2.785	-6.470	6.653
.7	7928	5.242	2.916	-6.466	6.712
.8	8128	5.257	3.041	-6.463	6.763
.9	8328	5.271	3.161	-6.460	6.809
1.0	8528	5.285	3.275	-6.457	6.850
1.1	8728	5.299	3.385	-6.454	6.888
1.2	8928	5.313	3.490	-6.452	6.923
1.3	9128	5.326	3.590	-6.449	6.956
1.4	9328	5.339	3.686	-6.447	6.987

$\log \tau = -1.4$ rise at exactly 360 K per decade of optical depth; while those below $\log \tau = -0.1$ rise at 2000 K per decade of optical depth. Model 1 reaches a temperature of 6528 K at optical depth unity.

The limb darkening residuals for Model 1 are shown in Table 7.6. The absolute intensity ratios for Model 1 are given in Table 7.9 (p. 167). The limb darkening residuals in the infrared range from -0.0040 to $+0.0028$. Those in the visible range from $+0.0004$ to $+0.0764$. The largest residuals in the infrared are only slightly bigger than the observational errors. The largest residuals in the visible, however, are many times the size of the expected errors in the observational measures of the limb darkening. The limb darkening residuals at 3204.68 and 4019.70 Å range from $+0.0223$ to $+0.0764$; while those from 4615.10 to 6694.00 Å range from $+0.0004$ to $+0.0202$. Although the residuals in the infrared are quite a bit smaller than those in the visible, there are similar trends as a function of wavelength. The residuals from 10840.10 to 12505.51 Å are all positive; while those from 16222.00 to 23132.73 Å are positive near disk center and negative close to the limb. The residuals from 38839.36 to 46142.57 Å are all negative. Positive limb darkening residuals thus tend to occur at short wavelengths; while negative residuals tend to occur at long wavelengths. The absolute intensities for Model 1 are in good agreement with the observations except at 3204.7 and 4019.7 Å.

Table 7.6. Residuals for Model 1.

λ (Å)	Log μ						
	-.10	-.20	-.30	-.40	-.50	-.60	-.70
3204.68	+.0391	+.0622	+.0728	+.0764	+.0747	+.0692	+.0610
3204.68 ^a	+.0225	+.0358	+.0423	+.0464	+.0486	+.0487	+.0471
4019.70	+.0223	+.0351	+.0403	+.0417	+.0407	+.0381	+.0343
4019.70 ^b	+.0203	+.0323	+.0377	+.0399	+.0402	+.0392	+.0371
4615.10	+.0127	+.0183	+.0202	+.0209	+.0208	+.0198	+.0179
4929.05	+.0106	+.0150	+.0159	+.0153	+.0147	+.0147	+.0153
5256.35	+.0126	+.0152	+.0170	+.0166	+.0153	+.0150	+.0164
6109.75	+.0068	+.0090	+.0099	+.0099	+.0101	+.0112	+.0131
6694.00	+.0004	+.0038	+.0051	+.0044	+.0036	+.0042	+.0063
10840.10	+.0016	+.0019	+.0019	+.0022	+.0024	+.0023	+.0018
10854.00	+.0013	+.0016	+.0017	+.0018	+.0021	+.0021	+.0016
10865.00	+.0012	+.0012	+.0013	+.0014	+.0015	+.0014	+.0009
12466.63	+.0018	+.0023	+.0024	+.0023	+.0023	+.0023	+.0022
12505.51	+.0020	+.0027	+.0028	+.0027	+.0026	+.0024	+.0021
16222.00	+.0012	+.0015	+.0012	+.0004	-.0007	-.0018	-.0028
16513.18	+.0011	+.0013	+.0008	-.0001	-.0013	-.0027	-.0040
21855.59	+.0003	.0000	-.0006	-.0014	-.0020	-.0024	-.0024
21907.47	+.0007	+.0005	.0000	-.0008	-.0015	-.0020	-.0023
23121.03	+.0001	-.0003	-.0010	-.0019	-.0027	-.0032	-.0036
23127.19	.0000	-.0006	-.0014	-.0024	-.0030	-.0035	-.0037
23132.73	+.0001	-.0005	-.0013	-.0021	-.0028	-.0032	-.0032
38839.36	-.0010	-.0021	-.0028	-.0031	-.0032	-.0030	-.0027
38862.02	-.0012	-.0025	-.0033	-.0037	-.0039	-.0040	-.0040
46142.57	-.0007	-.0015	-.0019	-.0020	-.0019	-.0016	-.0016
85636.32	-.0002	-.0004	-.0002	+.0002	+.0009	+.0014	+.0021
104007.55	-.0005	-.0008	-.0008	-.0006	-.0003	-.0001	-.0001

^aH⁻ bound-free absorption coefficient raised 81%.^bH⁻ bound-free absorption coefficient raised 16%.

When the residuals for the limb darkening observations of Pierce and Slaughter (1977) were first computed, it became obvious that Model 1 was unsatisfactory in the visible. An attempt was therefore made to improve the fit of the model by modifying the temperatures in the deeper layers of the photosphere. Model 1a is the result of this effort and illustrates what happens when the temperature gradient is steepened near optical depth unity. The deeper layers of Model 1 and 1a are shown together in Figure 7.2. The physical parameters of Model 1a are given in Table 7.7. Temperatures above $\log \tau = -0.4$ are the same in both models. Temperatures just below this level, however, are lower in Model 1a than they are in Model 1. Temperatures in Model 1a then rise above those in Model 1 slightly below optical depth unity. Temperatures below $\log \tau = +0.4$ are identical in both models. Model 1a reaches a temperature of 6508 K at optical depth unity.

The limb darkening residuals for Model 1a are listed in Table 7.8. The absolute intensity ratios for the model are given in Table 7.9. The modifications to the atmospheric temperature structure in Model 1a produce a number of small but important changes in the limb darkening residuals. It is useful to study these changes with the aid of Table 7.10. This table contains a list of the monochromatic optical depths that correspond to regular intervals of $\log \tau$ at 5000 Å in Model 1. It can therefore be used to determine

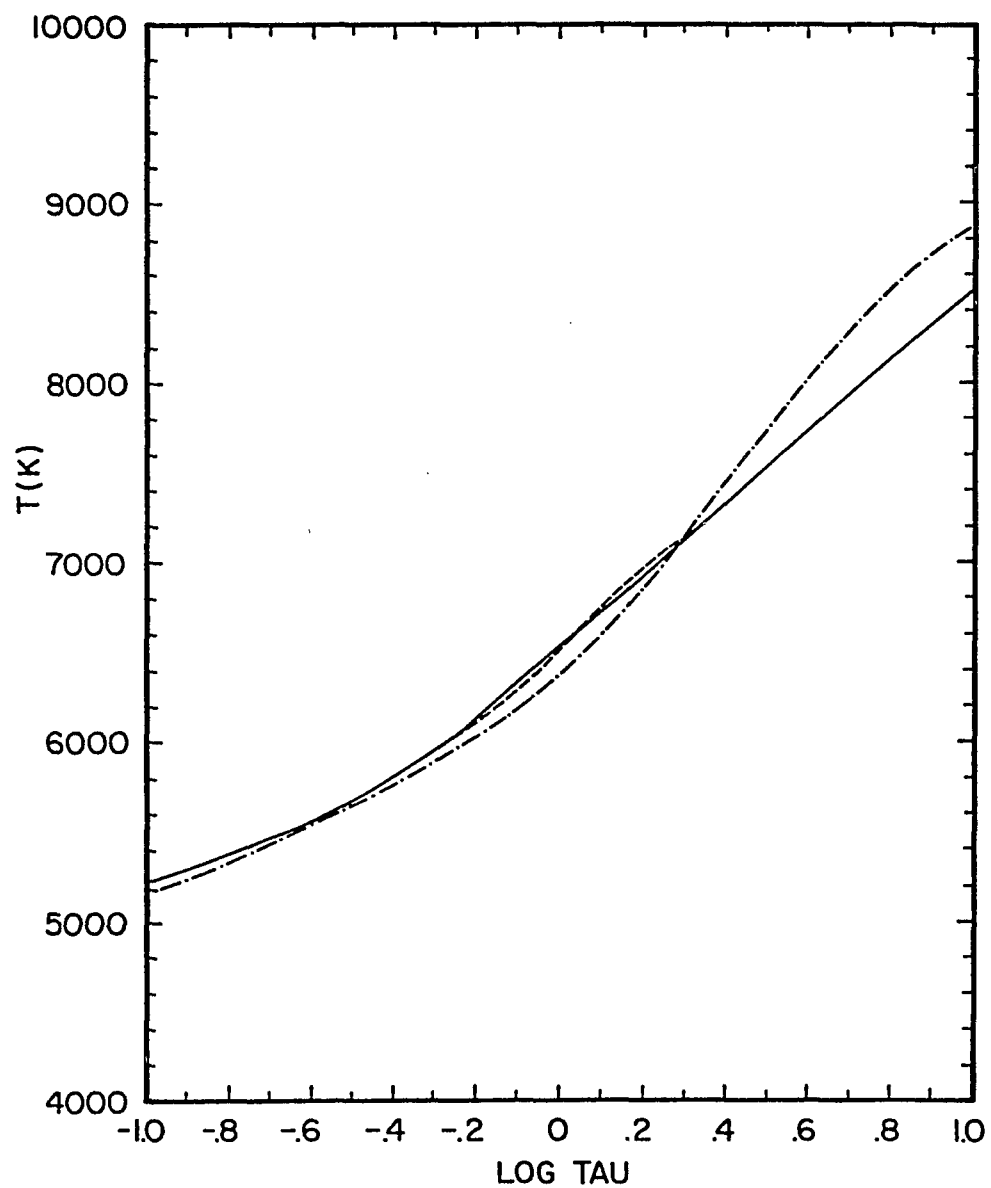


Figure 7.2. Solar models: (a) Model 1, —; (b) Model 1a, ---; (c) HSRA, -·-.

Table 7.7. Physical parameters of Model 1a.

Log τ_{5000} Å	T (K)	Log P_{gas} (dyne/cm ²)	Log P_e (dyne/cm ²)	Log density (g/cm ³)	Log depth (cm)
-5.0	5300	1.669	-1.205	-9.863	7.948
-4.9	5168	1.886	-1.256	-9.635	7.917
-4.8	5036	2.075	-1.318	-9.435	7.889
-4.7	4904	2.243	-1.376	-9.254	7.863
-4.6	4772	2.395	-1.412	-9.091	7.839
-4.5	4640	2.527	-1.410	-8.947	7.818
-4.4	4512	2.638	-1.369	-8.823	7.799
-4.3	4384	2.730	-1.319	-8.719	7.784
-4.2	4256	2.808	-1.283	-8.628	7.771
-4.1	4160	2.879	-1.256	-8.547	7.759
-4.0	4136	2.946	-1.210	-8.478	7.748
-3.9	4142	3.010	-1.154	-8.414	7.736
-3.8	4156	3.073	-1.096	-8.353	7.725
-3.7	4178	3.135	-1.035	-8.293	7.714
-3.6	4208	3.195	-.971	-8.236	7.702
-3.5	4244	3.255	-.906	-8.180	7.690
-3.4	4280	3.314	-.842	-8.124	7.678
-3.3	4316	3.372	-.778	-8.070	7.666
-3.2	4352	3.431	-.715	-8.015	7.653
-3.1	4388	3.488	-.653	-7.961	7.640
-3.0	4424	3.546	-.591	-7.907	7.626
-2.9	4460	3.603	-.529	-7.853	7.612
-2.8	4496	3.660	-.468	-7.800	7.597
-2.7	4532	3.717	-.407	-7.746	7.582
-2.6	4568	3.774	-.346	-7.693	7.566
-2.5	4604	3.830	-.286	-7.640	7.549
-2.4	4640	3.886	-.226	-7.587	7.531
-2.3	4676	3.943	-.166	-7.534	7.513
-2.2	4712	3.999	-.106	-7.481	7.494
-2.1	4748	4.055	-.047	-7.428	7.474
-2.0	4784	4.111	.013	-7.376	7.452
-1.9	4820	4.167	.072	-7.323	7.430
-1.8	4856	4.222	.131	-7.271	7.406
-1.7	4892	4.278	.190	-7.218	7.380
-1.6	4928	4.334	.249	-7.166	7.353
-1.5	4964	4.389	.308	-7.114	7.324
-1.4	5000	4.444	.367	-7.061	7.292
-1.3	5042	4.499	.428	-7.010	7.258
-1.2	5092	4.555	.492	-6.959	7.220
-1.1	5150	4.609	.560	-6.909	7.179

Table 7.7.--Continued

Log τ_{5000} Å	T (K)	Log P_{gas} (dyne/cm ²)	Log P_e (dyne/cm ²)	Log density (g/cm ³)	Log depth (cm)
-1.0	5216	4.664	.631	-6.860	7.133
-.9	5290	4.718	.706	-6.812	7.082
-.8	5372	4.771	.786	-6.766	7.023
-.7	5462	4.824	.873	-6.721	6.956
-.6	5560	4.874	.967	-6.678	6.877
-.5	5672	4.923	1.072	-6.638	6.784
-.4	5800	4.968	1.193	-6.602	6.670
-.3	5944	5.010	1.329	-6.571	6.525
-.2	6104	5.048	1.479	-6.544	6.327
-.1	6284	5.082	1.645	-6.523	5.999
.0	6508	5.111	1.844	-6.509	0.000
.1	6756	5.136	2.053	-6.501	5.934
.2	6960	5.157	2.220	-6.494	6.212
.3	7140	5.176	2.362	-6.485	6.373
.4	7330	5.194	2.506	-6.479	6.487
.5	7528	5.211	2.648	-6.474	6.574
.6	7728	5.227	2.786	-6.469	6.645
.7	7928	5.243	2.916	-6.465	6.704
.8	8128	5.258	3.042	-6.462	6.756
.9	8328	5.272	3.161	-6.459	6.802
1.0	8528	5.286	3.276	-6.456	6.844
1.1	8728	5.300	3.385	-6.453	6.882
1.2	8928	5.313	3.490	-6.451	6.918
1.3	9128	5.327	3.590	-6.449	6.951
1.4	9328	5.340	3.687	-6.447	6.982

Table 7.8. Residuals for Model 1a.

λ (Å)	Log μ						
	-.10	-.20	-.30	-.40	-.50	-.60	-.70
3204.68	+.0383	+.0602	+.0695	+.0719	+.0697	+.0643	+.0569
4019.70	+.0214	+.0333	+.0377	+.0385	+.0373	+.0350	+.0320
4615.10	+.0117	+.0163	+.0175	+.0178	+.0179	+.0175	+.0164
4929.05	+.0096	+.0131	+.0133	+.0125	+.0122	+.0128	+.0142
5256.35	+.0116	+.0133	+.0146	+.0141	+.0132	+.0135	+.0156
6109.75	+.0059	+.0074	+.0080	+.0082	+.0090	+.0107	+.0131
6694.00	-.0004	+.0024	+.0036	+.0032	+.0029	+.0041	+.0067
10840.10	+.0011	+.0010	+.0010	+.0014	+.0019	+.0023	+.0021
10854.00	+.0008	+.0007	+.0007	+.0010	+.0016	+.0021	+.0019
10865.00	+.0007	+.0004	+.0003	+.0006	+.0011	+.0015	+.0012
12466.63	+.0013	+.0014	+.0012	+.0011	+.0013	+.0016	+.0019
12505.51	+.0015	+.0018	+.0017	+.0015	+.0015	+.0017	+.0018
16222.00	+.0011	+.0011	+.0003	-.0009	-.0024	-.0039	-.0050
16513.18	+.0010	+.0009	.0000	-.0014	-.0031	-.0048	-.0062
21855.59	-.0001	-.0009	-.0019	-.0030	-.0037	-.0039	-.0036
21907.47	+.0003	-.0004	-.0013	-.0023	-.0031	-.0035	-.0036
23121.03	-.0003	-.0012	-.0023	-.0033	-.0041	-.0045	-.0045
23127.19	-.0004	-.0015	-.0027	-.0038	-.0045	-.0047	-.0046
23132.73	-.0003	-.0014	-.0026	-.0036	-.0043	-.0044	-.0041
38839.36	-.0010	-.0018	-.0023	-.0022	-.0021	-.0018	-.0014
38862.02	-.0012	-.0022	-.0027	-.0029	-.0029	-.0028	-.0028
46142.57	-.0005	-.0009	-.0010	-.0010	-.0008	-.0005	-.0004
85636.32	-.0002	-.0003	-.0001	+.0003	+.0009	+.0015	+.0022
104007.55	-.0005	-.0008	-.0008	-.0006	-.0003	-.0001	-.0001

Table 7.9. Ratios of the predicted absolute intensity at disk center to the observed absolute intensity at disk center for the one-component solar models.

λ (Å)	Model		
	HSRA	Model 1	Model 1a
3204.7	1.378	1.363	1.368
4019.7	1.109	1.094	1.094
6080.0	.983	1.012	1.010
6239.0	.963	.992	.991
6399.0	.966	.995	.993
6621.0	.974	1.004	1.001
7465.0	.977	1.007	1.005
8465.0	.969	.996	.994
9815.0	.952	.977	.975
86300.0	1.000	1.012	1.012
111000.0	.999	1.014	1.014
120200.0	.988	1.003	1.003

Table 7.10. Monochromatic optical depths for Model 1.

λ (Å)	$\log \tau_{5000 \text{ Å}}$						
	-2.0	-1.5	-1.0	-0.5	0.0	+0.5	+1.0
3204.68	.0074	.0216	.066	.209	.75	3.22	15.2
4019.70	.0082	.0254	.079	.250	.79	2.51	7.8
4615.10	.0093	.0292	.092	.291	.92	2.91	9.1
4929.05	.0099	.0312	.099	.312	.99	3.12	9.8
5256.35	.0105	.0332	.105	.332	1.05	3.32	10.6
6109.75	.0118	.0377	.119	.378	1.19	3.80	12.4
6694.00	.0125	.0399	.127	.400	1.26	4.06	13.5
10840.10	.0117	.0375	.120	.380	1.21	4.00	13.9
10854.00	.0117	.0374	.119	.380	1.21	4.00	13.9
10865.00	.0117	.0374	.119	.379	1.21	3.99	13.9
12466.63	.0090	.0288	.093	.299	.99	3.49	13.6
12505.51	.0089	.0286	.092	.297	.98	3.48	13.6
16222.00	.0022	.0078	.028	.107	.46	2.27	11.7
16513.18	.0021	.0075	.027	.105	.46	2.30	12.0
21855.59	.0036	.0129	.047	.180	.79	3.95	21.2
21907.47	.0036	.0129	.047	.181	.79	3.97	21.3
23121.03	.0040	.0144	.052	.200	.87	4.24	21.8
23127.19	.0040	.0144	.052	.200	.87	4.24	21.8
23132.73	.0040	.0144	.052	.200	.87	4.24	21.8
38839.36	.0110	.0398	.144	.551	2.37	11.57	60.0
38862.02	.0111	.0398	.144	.552	2.37	11.58	60.1
45908.50	.0154	.0553	.200	.766	3.28	15.93	82.1
46142.57	.0155	.0559	.202	.774	3.31	16.09	82.9
85636.32	.0528	.1901	.687	2.635	11.42	58.18	320.8
104007.55	.0775	.2794	1.010	3.874	16.78	85.56	471.9

the atmospheric depths that affect the limb darkening residuals at each wavelength.

The residuals at 3204.68 and 4019.70 Å range from +.0214 to +.0719 in Model 1a. The residuals at these two wavelengths are therefore lowered by the changes in Model 1a. From Table 7.10 one finds that the residuals at 3204.68 and 4019.70 Å are primarily affected by the temperatures from from $\log \tau = -1.0$ to $\log \tau = +0.5$. The lower temperatures above optical depth unity and the higher temperatures immediately below optical depth unity in Model 1a are obviously responsible for the reduced limb darkening residuals at these two wavelengths. The residuals at 4615.10, 4929.05, and 5256.35 Å are also slightly reduced by the changes in Model 1a.

The residuals from 6109.75 to 10865.00 Å are lowered near disk center and raised near the limb in Model 1a. The radiation at these wavelengths comes from somewhat higher levels in the atmosphere than that at shorter wavelengths. The residuals at these wavelengths are therefore primarily affected by the lower temperatures above optical depth unity in the model. As one proceeds to still longer wavelengths, however, the atmosphere once again becomes relatively transparent. The limb darkening residuals from 12466.63 to 23132.73 Å are therefore also lowered by the changes in Model 1a. Unfortunately, many of the residuals at these wavelengths are already negative. Model 1a is therefore

worse than Model 1 in this region of the spectrum. The negative residuals at 38839.36, 38862.02, and 46142.57 Å are raised by the changes in Model 1a. These wavelengths are formed high in the photosphere and are affected only by the lower temperatures above optical depth unity. The residuals at 85636.32 and 104007.55 Å are left essentially unchanged.

The changes in Model 1a improve the fit in the visible, but they have a deleterious effect at wavelengths around the H^- opacity minimum. Since it is necessary to adopt a fairly low temperature gradient in the deepest layers of the atmosphere in order to keep the residuals at 16222.00 and 16513.18 Å within reasonable bounds, it is impossible to reproduce the observations in the visible. Thus neither the HSRA, Model 1, or Model 1a is completely satisfactory.

Since the bound-free and free-free absorption coefficients of H^- are somewhat uncertain, several models were developed to ascertain the effects of changes in the H^- opacity representations in the program. In one model the H^- bound-free absorption coefficient was reduced at all wavelengths by 20%. The residuals for this model were only slightly different from those without the change. Increasing the H^- bound-free absorption coefficient by 20% also had a negligible effect. In neither model was there

any indication that an even larger change would resolve the discrepancy in the deep layers of the atmosphere.

The disk-center intensity at 3204.7 \AA is very high in Model 1. An error in the H^- bound-free absorption coefficient at this wavelength would affect both the limb darkening and the absolute intensity at disk center. The limb darkening at 3204.68 \AA was therefore computed a second time with Model 1. The H^- bound-free absorption coefficient at 3204.68 \AA , however, was increased as much as necessary to drive the predicted intensity at disk center to within $\pm 0.5\%$ of the observational value. This required an 81% increase in the absorption coefficient. A similar experiment was also performed at 4019.70 \AA . Only a 16% increase in the bound-free absorption coefficient was required at this wavelength. The limb darkening residuals at both wavelengths in the experimental models are given in Table 7.6. The residuals are improved near disk center but are worse near the limb. The fact that the residuals are worse near the limb indicates that the H^- bound-free absorption coefficient is not the source of the large residuals at these wavelengths.

The HSRA has a steep temperature gradient near optical depth unity, and the residuals in the visible are smaller than those for Model 1. The H^- free-free absorption coefficient, however, would have to be increased by 150% in order to correct the residuals at 16222.00 or 16513.18 \AA .

The increase that is required at 16222.00 and 16513.18 Å is also very much larger than that required at slightly shorter and longer wavelengths. An increase of 50% in the H^- free-free absorption coefficient is more than enough to correct the residuals at 12505.51 and 21855.59 Å. A constant or simple monotonic change in the H^- free-free absorption coefficient as a function of wavelength throughout the infrared would therefore not improve the fit of the model.

7.5 Two-Component Models of the Solar Atmosphere

The solar surface is covered with thousands of small granules that brighten and fade into obscurity in a matter of minutes. These granules are the direct result of a sub-surface convection zone on the sun, and their existence shows that the assumption of a single temperature versus optical depth relation for the photosphere is inherently incorrect.

A model solar atmosphere with inhomogeneities was first proposed by Bohm (1954) to explain the center-to-limb variations of a number of lines in the solar spectrum. The Utrecht Reference Model of the Photosphere and Low Chromosphere by Heintze et al. (1964) later became the first major reference model to incorporate more than one temperature component in the atmosphere. One component of the URP represented the hot gas in the rising granules, a second component represented the cool gas that was descending

around the rising granules, and a third component represented the stationary gas that was at some intermediate temperature. The splitting of the hot and cool components was based on a model by Voight (1956) that had been proposed to explain the asymmetry of the O I triplet at 7774 \AA . Unfortunately, the individual components of the URP were not well defined by other observations, and most users of the model chose to ignore the hot and cool components altogether. Estimates of the rms intensity fluctuations in the solar atmosphere by Schwarzschild (1959), Bahng and Schwarzschild (1961), and Edmonds (1962) also tended to support the view that the temperature variations in the visible layers of the atmosphere were small and unimportant. All of the major reference models since the URP have therefore simply ignored the spatial inhomogeneities in the atmosphere.

Model 2 is a composite of two standard solar models. One component of Model 2 represents the half of the solar surface that is covered by columns of gas that are generally above the median temperature at each depth in the atmosphere; while the other component represents the half of the solar surface that is covered by columns of gas that are generally below the median temperature at each depth. The specific intensity at any point on the sun is therefore computed by simply averaging together the intensities from the hot and cool components of the model. Measures of the

solar limb darkening are then derived by normalizing the resulting intensities to the average intensity at disk center. Since the two components of Model 2 are independent, they have separate optical depth scales. Small pressure differences also exist between the hot and cool components of the model at various depths in the atmosphere.

The two components of Model 2 are shown in Figure 7.3. The physical parameters of the hot and cool components of the model are listed separately in Tables 7.11 and 7.12. Temperatures in both components above $\log \tau = -3.6$ are the same as those in Model 1. Temperatures then run slightly cooler than those in Model 1 until the components split at $\log \tau = -0.4$. The hot component then rises rapidly and reaches a temperature of 6818 K at optical depth unity; while the cool component turns over and only reaches a temperature of 6168 K at the same depth. Temperatures in the hot component rise at 4000 K per decade of optical depth from optical depth unity to $\log \tau = +0.1$. The hot component then levels off, and temperatures below $\log \tau = +0.5$ rise at 3000 K per decade of optical depth. Temperatures in the cool component of Model 2 rise at only 600 K per decade of optical depth from optical depth unity to $\log \tau = +0.3$. The temperature gradient then steepens gradually, and temperatures below $\log \tau = +1.1$ rise at 3000 K per decade of optical depth just as they do in the hot component of the

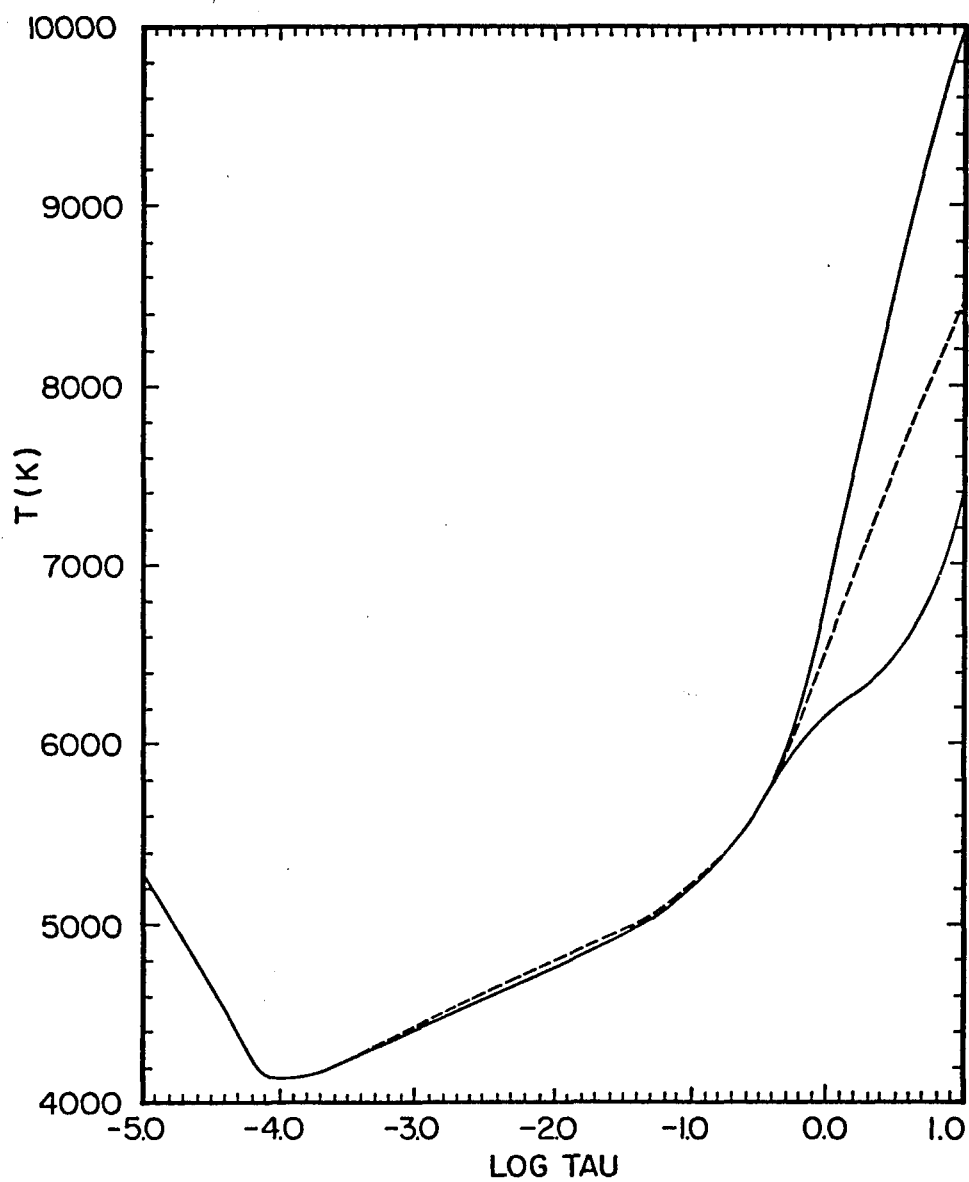


Figure 7.3. Solar models: (a) Model 2, —; (b) Model 1, ---.

Table 7.11. Physical parameters of the hot component of Model 2.

Log τ_{5000} Å	T (K)	Log P_{gas} (dyne/cm ²)	Log P_e (dyne/cm ²)	Log density (g/cm ³)	Log depth (cm)
-5.0	5300	1.669	-1.205	-9.863	7.946
-4.9	5168	1.886	-1.256	-9.635	7.915
-4.8	5036	2.075	-1.318	-9.435	7.887
-4.7	4904	2.243	-1.367	-9.254	7.860
-4.6	4772	2.395	-1.412	-9.091	7.836
-4.5	4640	2.527	-1.410	-8.947	7.815
-4.4	4512	2.638	-1.369	-8.823	7.796
-4.3	4384	2.730	-1.319	-8.719	7.781
-4.2	4256	2.808	-1.283	-8.628	7.767
-4.1	4160	2.879	-1.256	-8.547	7.755
-4.0	4136	2.946	-1.210	-8.478	7.744
-3.9	4142	3.010	-1.154	-8.414	7.733
-3.8	4156	3.073	-1.096	-8.353	7.721
-3.7	4178	3.135	-1.035	-8.293	7.710
-3.6	4208	3.195	-.971	-8.236	7.698
-3.5	4240	3.255	-.908	-8.179	7.686
-3.4	4272	3.314	-.845	-8.124	7.674
-3.3	4304	3.372	-.783	-8.068	7.661
-3.2	4336	3.430	-.722	-8.013	7.648
-3.1	4368	3.488	-.661	-7.959	7.635
-3.0	4400	3.546	-.600	-7.905	7.621
-2.9	4436	3.603	-.538	-7.851	7.607
-2.8	4472	3.660	-.477	-7.798	7.592
-2.7	4508	3.716	-.416	-7.744	7.577
-2.6	4544	3.773	-.355	-7.691	7.561
-2.5	4580	3.830	-.295	-7.638	7.544
-2.4	4616	3.886	-.235	-7.585	7.526
-2.3	4652	3.942	-.175	-7.532	7.508
-2.2	4688	3.998	-.115	-7.480	7.488
-2.1	4724	4.054	-.055	-7.427	7.468
-2.0	4760	4.110	.004	-7.374	7.446
-1.9	4796	4.166	.063	-7.322	7.424
-1.8	4832	4.222	.123	-7.269	7.399
-1.7	4868	4.278	.182	-7.217	7.374
-1.6	4904	4.333	.241	-7.164	7.346
-1.5	4942	4.389	.300	-7.112	7.316
-1.4	4982	4.444	.361	-7.060	7.284
-1.3	5026	4.499	.422	-7.009	7.250
-1.2	5076	4.554	.486	-6.958	7.211
-1.1	5134	4.609	.553	-6.908	7.169

Table 7.11.--Continued Physical parameters of the hot
component of Model 2.

Log τ_{5000} Å	T (K)	Log P_{gas} (dyne/cm ²)	Log P_e (dyne/cm ²)	Log density (g/cm ³)	Log depth (cm)
-1.0	5200	4.664	.624	-6.859	7.122
-.9	5274	4.718	.699	-6.811	7.069
-.8	5356	4.772	.779	-6.764	7.009
-.7	5446	4.824	.865	-6.719	6.939
-.6	5546	4.875	.959	-6.676	6.857
-.5	5662	4.924	1.067	-6.636	6.758
-.4	5794	4.970	1.189	-6.600	6.635
-.3	5946	5.012	1.331	-6.569	6.477
-.2	6138	5.049	1.507	-6.546	6.254
-.1	6442	5.079	1.773	-6.537	5.890
.0	6818	5.101	2.083	-6.540	0.000
.1	7218	5.117	2.388	-6.550	5.767
.2	7590	5.128	2.647	-6.560	6.019
.3	7926	5.138	2.862	-6.571	6.157
.4	8242	5.146	3.050	-6.581	6.251
.5	8548	5.153	3.218	-6.591	6.323
.6	8848	5.159	3.373	-6.602	6.380
.7	9148	5.165	3.517	-6.614	6.428
.8	9448	5.170	3.651	-6.626	6.469
.9	9748	5.175	3.777	-6.639	6.505
1.0	10048	5.179	3.894	-6.653	6.538
1.1	10348	5.183	4.003	-6.668	6.567
1.2	10648	5.187	4.104	-6.685	6.594
1.3	10948	5.191	4.198	-6.702	6.619
1.4	11248	5.194	4.284	-6.721	6.643

Table 7.12. Physical parameters of the cool component of Model 2.

Log τ_{5000} Å	T (K)	Log P_{gas} (dyne/cm ²)	Log P_e (dyne/cm ²)	Log density (g/cm ³)	Log depth (cm)
-5.0	5300	1.669	-1.205	-9.863	7.950
-4.9	5168	1.886	-1.256	-9.635	7.919
-4.8	5036	2.075	-1.318	-9.435	7.891
-4.7	4904	2.243	-1.376	-9.254	7.866
-4.6	4772	2.395	-1.412	-9.091	7.842
-4.5	4640	2.527	-1.410	-8.947	7.820
-4.4	4512	2.638	-1.369	-8.823	7.802
-4.3	4384	2.730	-1.319	-8.719	7.787
-4.2	4256	2.808	-1.283	-8.628	7.774
-4.1	4160	2.879	-1.256	-8.547	7.762
-4.0	4136	2.946	-1.210	-8.478	7.751
-3.9	4142	3.010	-1.154	-8.414	7.739
-3.8	4156	3.073	-1.096	-8.353	7.728
-3.7	4178	3.135	-1.035	-8.293	7.717
-3.6	4208	3.195	-.971	-8.236	7.705
-3.5	4240	3.255	-.908	-8.179	7.694
-3.4	4272	3.314	-.845	-8.124	7.682
-3.3	4304	3.372	-.783	-8.068	7.669
-3.2	4336	3.430	-.722	-8.013	7.657
-3.1	4368	3.488	-.661	-7.959	7.644
-3.0	4400	3.546	-.600	-7.905	7.630
-2.9	4436	3.603	-.538	-7.851	7.616
-2.8	4472	3.660	-.477	-7.798	7.601
-2.7	4508	3.716	-.416	-7.744	7.586
-2.6	4544	3.773	-.355	-7.691	7.571
-2.5	4580	3.830	-.295	-7.638	7.554
-2.4	4616	3.886	-.235	-7.587	7.537
-2.3	4652	3.942	-.175	-7.532	7.519
-2.2	4688	3.998	-.115	-7.480	7.500
-2.1	4724	4.054	-.055	-7.427	7.480
-2.0	4760	4.110	.004	-7.374	7.459
-1.9	4796	4.166	.063	-7.322	7.437
-1.8	4832	4.222	.123	-7.269	7.414
-1.7	4868	4.278	.182	-7.217	7.389
-1.6	4904	4.333	.241	-7.164	7.362
-1.5	4942	4.389	.300	-7.112	7.334
-1.4	4982	4.444	.361	-7.060	7.303
-1.3	5026	4.499	.422	-7.009	7.270
-1.2	5076	4.554	.486	-6.958	7.234
-1.1	5134	4.609	.553	-6.908	7.194

Table 7.12.--Continued Physical parameters of the cool component of Model 2.

τ_{5000}	Log λ Å	T (K)	Log P_{gas} (dyne/cm ²)	Log P_e (dyne/cm ²)	Log density (g/cm ³)	Log depth (cm)
-1.0		5200	4.664	.624	-6.859	7.149
-.9		5274	4.718	.699	-6.811	7.100
-.8		5356	4.772	.779	-6.764	7.044
-.7		5446	4.824	.865	-6.719	6.980
-.6		5546	4.875	.959	-6.676	6.905
-.5		5662	4.924	1.067	-6.636	6.818
-.4		5792	4.970	1.188	-6.600	6.714
-.3		5916	5.012	1.308	-6.567	6.584
-.2		6016	5.053	1.411	-6.534	6.406
-.1		6100	5.092	1.502	-6.501	6.104
.0		6168	5.131	1.579	-6.467	0.000
.1		6228	5.170	1.650	-6.432	6.115
.2		6288	5.209	1.721	-6.396	6.420
.3		6348	5.249	1.792	-6.360	6.600
.4		6416	5.290	1.868	-6.325	6.729
.5		6500	5.329	1.957	-6.291	6.828
.6		6612	5.368	2.066	-6.260	6.908
.7		6760	5.404	2.199	-6.233	6.972
.8		6956	5.436	2.363	-6.213	7.024
.9		7196	5.464	2.551	-6.200	7.066
1.0		7468	5.488	2.750	-6.193	7.099
1.1		7760	5.508	2.948	-6.190	7.127
1.2		8060	5.525	3.138	-6.190	7.150
1.3		8360	5.541	3.314	-6.191	7.170
1.4		8660	5.554	3.479	-6.194	7.188

model. The two components of Model 2 are split by 650 K at optical depth unity.

The physical conditions in the hot and cool components of Model 2 are identical above $\log \tau = -0.4$. There is a slight offset in the height scale above this level, however, because of differences between the two components near optical depth unity. One can compare the two components on a single height scale if the depths in each component of the model are zeroed at the temperature minimum rather than at optical depth unity. The depths and physical conditions in both components will then be the same at all points above $\log \tau = -0.4$. Geometric depths on such a scale for both components of Model 2 are given in Table 7.18 (p. 196). The entries in this table show quite clearly that the opacity in the hot component rises much faster than the opacity in the cool component as a function of depth.

The limb darkening residuals for Model 2 are given in Table 7.13. The absolute intensity ratios for Model 2 are listed in Table 7.17 (p. 189). The limb darkening residuals from 4615.10 to 104007.55 Å are almost all quite a bit smaller than the expected errors in the observational measures of the limb darkening. The absolute intensity ratios for the model are also close to one except at 3204.7 and 4019.7 Å. At short wavelengths a large fraction of the radiation comes from the hot components of the model; while at long wavelengths the contributions from the two

Table 7.13. Residuals for Model 2.

λ (Å)	Log μ						
	-.10	-.20	-.30	-.40	-.50	-.60	-.70
3204.68	+.0300	+.0464	+.0527	+.0541	+.0522	+.0480	+.0421
4019.70	+.0074	+.0100	+.0090	+.0075	+.0063	+.0055	+.0046
4615.10	+.0021	+.0003	-.0022	-.0035	-.0035	-.0031	-.0032
4929.05	+.0017	.0000	-.0029	-.0050	-.0055	-.0043	-.0021
5256.35	+.0052	+.0027	+.0014	-.0002	-.0012	-.0006	+.0021
6109.75	+.0022	+.0012	+.0003	-.0002	+.0003	+.0020	+.0046
6694.00	-.0030	-.0019	-.0018	-.0028	-.0034	-.0023	+.0003
10840.10	+.0005	+.0001	-.0002	.0000	+.0004	+.0006	+.0002
10854.00	+.0003	-.0002	-.0004	-.0003	+.0001	+.0004	.0000
10865.00	+.0002	-.0005	-.0008	-.0007	-.0004	-.0002	-.0007
12466.63	+.0014	+.0018	+.0016	+.0016	+.0018	+.0019	+.0021
12505.51	+.0017	+.0022	+.0021	+.0020	+.0020	+.0021	+.0020
16222.00	+.0012	+.0018	+.0017	+.0013	+.0005	-.0003	-.0009
16513.18	+.0012	+.0016	+.0015	+.0009	.0000	-.0010	-.0019
21855.59	+.0008	+.0009	+.0008	+.0005	+.0003	+.0004	+.0008
21907.47	+.0012	+.0015	+.0014	+.0011	+.0009	+.0008	+.0009
23121.03	+.0005	+.0005	+.0002	-.0002	-.0006	-.0007	-.0006
23127.19	+.0004	+.0003	-.0002	-.0007	-.0009	-.0010	-.0007
23132.73	+.0006	+.0004	-.0001	-.0005	-.0007	-.0006	-.0003
38839.36	-.0005	-.0011	-.0014	-.0014	-.0014	-.0013	-.0011
38862.02	-.0007	-.0015	-.0019	-.0021	-.0022	-.0023	-.0025
46142.57	-.0003	-.0007	-.0009	-.0009	-.0009	-.0008	-.0010
85636.32	-.0004	-.0007	-.0007	-.0005	.0000	+.0003	+.0008
104007.55	-.0007	-.0012	-.0013	-.0013	-.0013	-.0012	-.0013

components are nearly equal. Branching the model thus allows one to steepen the limb darkening in the visible without changing it in the infrared. The splitting in Model 2 is large enough to resolve the difficulties in fitting the observations from 4615.10 to 104007.55 Å.

Model 2 is partially successful in resolving the discrepancy between the visible and infrared limb darkening measures. Other two-component models were studied, however, in order to see if the residuals at 3204.68 and 4019.70 Å could be further improved. One of the best of these models is shown as Model 2a in Figure 7.4. The physical parameters of the hot and cool components of Model 2a are given in Tables 7.14 and 7.15. Model 2a has a minimum temperature of 4450 K at $\log \tau = -4.0$. Temperatures in both components then rise at 200 K per decade of optical depth from $\log \tau = -3.5$ to $\log \tau = -1.7$. Model 2a splits at $\log \tau = -0.6$. Temperatures in the hot component rise at 8000 K per decade of optical depth from $\log \tau = +0.1$ to $\log \tau = +0.3$. Temperatures in both components of Model 2a rise at only 400 K per decade of optical depth below $\log \tau = +0.5$.

The limb darkening residuals for Model 2a are given in Table 7.16. The absolute intensity ratios for the model are listed in Table 7.17. The limb darkening residuals at 3204.68 Å range from -0.0012 to $+0.0150$; while the residuals at 4019.70 Å range from -0.0155 to $+0.0050$. Limb darkening residuals in the infrared range from -0.0082 to $+0.0088$. The

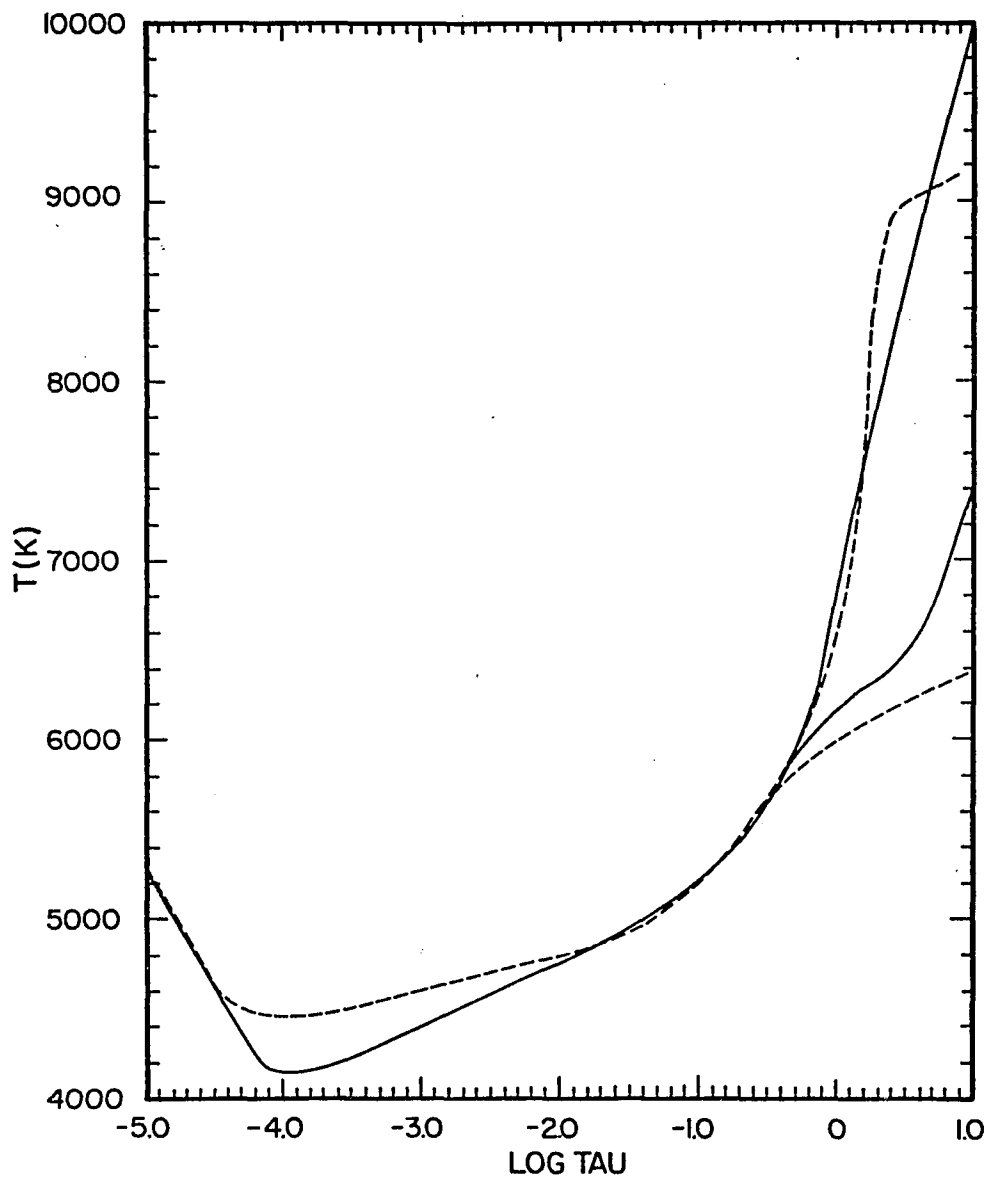


Figure 7.4. Solar models: (a) Model 2, —; (b) Model 2a, ---.

Table 7.14. Physical parameters of the hot component of Model 2a.

Log τ_{5000} Å	T (K)	Log P_{gas} (dyne/cm ²)	Log P_e (dyne/cm ²)	Log density (g/cm ³)	Log depth (cm)
-5.0	5300	1.669	-1.205	-9.863	7.953
-4.9	5168	1.886	-1.256	-9.635	7.922
-4.8	5036	2.075	-1.318	-9.435	7.894
-4.7	4904	2.243	-1.376	-9.254	7.869
-4.6	4772	2.395	-1.412	-9.091	7.845
-4.5	4640	2.527	-1.410	-8.947	7.824
-4.4	4528	2.638	-1.364	-8.825	7.806
-4.3	4482	2.731	-1.294	-8.727	7.790
-4.2	4462	2.813	-1.225	-8.643	7.776
-4.1	4452	2.888	-1.159	-8.568	7.763
-4.0	4450	2.957	-1.097	-8.498	7.750
-3.9	4452	3.023	-1.037	-8.433	7.738
-3.8	4458	3.087	-.979	-8.370	7.726
-3.7	4468	3.148	-.921	-8.309	7.714
-3.6	4482	3.209	-.863	-8.250	7.701
-3.5	4500	3.268	-.806	-8.192	7.689
-3.4	4520	3.327	-.748	-8.135	7.676
-3.3	4540	3.385	-.691	-8.079	7.663
-3.2	4560	3.442	-.635	-8.024	7.649
-3.1	4580	3.499	-.579	-7.968	7.636
-3.0	4600	3.556	-.523	-7.913	7.621
-2.9	4620	3.613	-.468	-7.859	7.606
-2.8	4640	3.669	-.413	-7.804	7.591
-2.7	4660	3.725	-.358	-7.750	7.575
-2.6	4680	3.781	-.303	-7.696	7.559
-2.5	4700	3.837	-.249	-7.642	7.542
-2.4	4720	3.892	-.195	-7.588	7.524
-2.3	4740	3.948	-.141	-7.535	7.505
-2.2	4760	4.003	-.087	-7.481	7.486
-2.1	4780	4.059	-.033	-7.428	7.465
-2.0	4800	4.114	.021	-7.374	7.443
-1.9	4820	4.169	.074	-7.321	7.421
-1.8	4840	4.224	.127	-7.267	7.396
-1.7	4860	4.280	.181	-7.214	7.371
-1.6	4886	4.335	.236	-7.161	7.343
-1.5	4920	4.390	.294	-7.109	7.314
-1.4	4962	4.445	.355	-7.058	7.282
-1.3	5012	4.500	.418	-7.007	7.247
-1.2	5070	4.555	.485	-6.957	7.209
-1.1	5136	4.610	.555	-6.908	7.167

Table 7.14.--Continued Physical parameters of the hot component of Model 2a.

τ_{5000} Å	T (K)	Log P_{gas} (dyne/cm ²)	Log P_e (dyne/cm ²)	Log density (g/cm ³)	Log depth (cm)
-1.0	5210	4.664	.628	-6.859	7.119
-.9	5292	4.718	.707	-6.812	7.066
-.8	5382	4.771	.791	-6.766	7.005
-.7	5480	4.823	.882	-6.722	6.935
-.6	5592	4.873	.986	-6.681	6.853
-.5	5720	4.920	1.104	-6.644	6.756
-.4	5864	4.964	1.238	-6.611	6.639
-.3	6024	5.004	1.388	-6.583	6.491
-.2	6200	5.039	1.552	-6.561	6.289
-.1	6396	5.069	1.730	-6.544	5.960
.0	6640	5.095	1.941	-6.534	0.000
.1	7000	5.116	2.229	-6.537	5.875
.2	7800	5.129	2.781	-6.572	6.099
.3	8600	5.134	3.236	-6.613	6.177
.4	8900	5.138	3.387	-6.626	6.227
.5	9000	5.142	3.437	-6.628	6.275
.6	9040	5.147	3.458	-6.625	6.325
.7	9080	5.153	3.480	-6.622	6.379
.8	9120	5.159	3.501	-6.618	6.435
.9	9160	5.167	3.524	-6.612	6.493
1.0	9200	5.176	3.546	-6.605	6.553
1.1	9240	5.187	3.570	-6.596	6.615
1.2	9280	5.200	3.594	-6.586	6.678
1.3	9320	5.214	3.619	-6.574	6.741
1.4	9360	5.231	3.645	-6.559	6.804

Table 7.15. Physical parameters of the cool component of Model 2a.

τ_{5000}	Log $\frac{\circ}{\text{\AA}}$	T (K)	Log P_{gas} (dyne/cm ²)	Log P_e (dyne/cm ²)	Log density (g/cm ³)	Log depth (cm)
-5.0		5300	1.669	-1.205	-9.863	7.960
-4.9		5168	1.886	-1.256	-9.635	7.930
-4.8		5036	2.075	-1.318	-9.435	7.902
-4.7		4904	2.243	-1.376	-9.254	7.877
-4.6		4772	2.395	-1.412	-9.091	7.854
-4.5		4640	2.527	-1.410	-8.947	7.833
-4.4		4528	2.638	-1.364	-8.825	7.815
-4.3		4482	2.731	-1.294	-8.727	7.800
-4.2		4462	2.813	-1.225	-8.643	7.787
-4.1		4452	2.888	-1.159	-8.568	7.774
-4.0		4450	2.957	-1.097	-8.498	7.761
-3.9		4452	3.023	-1.037	-8.433	7.749
-3.8		4458	3.087	-.979	-8.370	7.737
-3.7		4468	3.148	-.921	-8.309	7.726
-3.6		4482	3.209	-.863	-8.250	7.714
-3.5		4500	3.268	-.806	-8.192	7.701
-3.4		4520	3.327	-.748	-8.135	7.689
-3.3		4540	3.385	-.691	-8.079	7.676
-3.2		4560	3.442	-.635	-8.024	7.663
-3.1		4580	3.499	-.579	-7.968	7.650
-3.0		4600	3.556	-.523	-7.913	7.636
-2.9		4620	3.613	-.468	-7.859	7.622
-2.8		4640	3.669	-.413	-7.804	7.607
-2.7		4660	3.725	-.358	-7.750	7.592
-2.6		4680	3.781	-.303	-7.696	7.576
-2.5		4700	3.837	-.249	-7.642	7.559
-2.4		4720	3.892	-.195	-7.588	7.542
-2.3		4740	3.948	-.141	-7.535	7.524
-2.2		4760	4.003	-.087	-7.481	7.506
-2.1		4780	4.059	-.033	-7.428	7.486
-2.0		4800	4.114	.021	-7.374	7.465
-1.9		4820	4.169	.074	-7.321	7.444
-1.8		4840	4.224	.127	-7.267	7.421
-1.7		4860	4.280	.181	-7.214	7.397
-1.6		4886	4.335	.236	-7.161	7.371
-1.5		4920	4.390	.294	-7.109	7.343
-1.4		4962	4.445	.355	-7.058	7.313
-1.3		5012	4.500	.418	-7.007	7.281
-1.2		5070	4.555	.485	-6.957	7.246
-1.1		5136	4.610	.555	-6.908	7.207

Table 7.15.--Continued Physical parameters of the cool component of Model 2a.

Log τ_{5000} Å	T (K)	Log P_{gas} (dyne/cm ²)	Log P_e (dyne/cm ²)	Log density (g/cm ³)	Log depth (cm)
-1.0	5210	4.664	.628	-6.859	7.165
-.9	5292	4.718	.707	-6.812	7.117
-.8	5382	4.771	.791	-6.766	7.063
-.7	5480	4.823	.882	-6.722	7.003
-.6	5578	4.873	.977	-6.680	6.933
-.5	5668	4.922	1.069	-6.639	6.852
-.4	5750	4.969	1.157	-6.598	6.755
-.3	5824	5.014	1.241	-6.558	6.630
-.2	5890	5.059	1.319	-6.518	6.455
-.1	5948	5.104	1.391	-6.477	6.156
.0	5998	5.149	1.457	-6.436	0.000
.1	6040	5.194	1.517	-6.394	6.164
.2	6080	5.240	1.576	-6.351	6.470
.3	6120	5.286	1.635	-6.307	6.650
.4	6160	5.333	1.694	-6.263	6.779
.5	6200	5.381	1.753	-6.218	6.880
.6	6240	5.429	1.812	-6.173	6.963
.7	6280	5.477	1.871	-6.128	7.033
.8	6320	5.525	1.930	-6.082	7.094
.9	6360	5.574	1.988	-6.036	7.149
1.0	6400	5.623	2.047	-5.990	7.198
1.1	6440	5.672	2.106	-5.943	7.242
1.2	6480	5.722	2.164	-5.897	7.283
1.3	6520	5.772	2.222	-5.850	7.320
1.4	6560	5.821	2.280	-5.802	7.355

Table 7.16. Residuals for Model 2a.

λ (Å)	Log μ						
	-.10	-.20	-.30	-.40	-.50	-.60	-.70
3204.68	+.0043	+.0017	-.0012	+.0005	+.0058	+.0113	+.0150
4019.70	+.0050	-.0009	-.0101	-.0155	-.0156	-.0120	-.0090
4615.10	-.0049	-.0145	-.0217	-.0230	-.0192	-.0151	-.0107
4929.05	-.0058	-.0143	-.0203	-.0212	-.0173	-.0125	-.0064
5256.35	-.0022	-.0103	-.0132	-.0126	-.0093	-.0051	+.0009
6109.75	-.0035	-.0072	-.0072	-.0040	-.0003	+.0048	+.0093
6694.00	-.0073	-.0075	-.0056	-.0029	-.0005	+.0034	+.0074
10840.10	-.0011	-.0015	-.0001	+.0029	+.0057	+.0079	+.0086
10854.00	-.0013	-.0018	-.0004	+.0026	+.0053	+.0077	+.0084
10865.00	-.0015	-.0021	-.0007	+.0021	+.0048	+.0070	+.0077
12466.63	-.0007	-.0013	-.0007	+.0014	+.0043	+.0067	+.0088
12505.51	-.0004	-.0009	-.0002	+.0018	+.0045	+.0069	+.0086
16222.00	-.0008	-.0029	-.0054	-.0071	-.0076	-.0068	-.0048
16513.18	-.0009	-.0032	-.0057	-.0075	-.0082	-.0075	-.0058
21855.59	-.0012	-.0018	-.0013	+.0002	+.0026	+.0052	+.0079
21907.47	-.0007	-.0011	-.0006	+.0010	+.0032	+.0057	+.0080
23121.03	-.0010	-.0013	-.0006	+.0011	+.0032	+.0055	+.0075
23127.19	-.0011	-.0016	-.0010	+.0006	+.0029	+.0052	+.0075
23132.73	-.0010	-.0015	-.0008	+.0008	+.0031	+.0056	+.0079
38839.36	+.0019	+.0036	+.0049	+.0061	+.0066	+.0069	+.0068
38862.02	+.0017	+.0032	+.0045	+.0054	+.0058	+.0058	+.0055
46142.57	+.0018	+.0029	+.0036	+.0039	+.0039	+.0038	+.0033
85636.32	-.0006	-.0012	-.0013	-.0011	-.0004	+.0004	+.0017
104007.55	-.0009	-.0015	-.0015	-.0011	-.0003	+.0007	+.0020

Table 7.17. Ratios of the predicted absolute intensity at disk center to the observed absolute intensity at disk center for the two-component solar models.

λ (Å)	Model	
	Model 2	Model 2a
3204.7	1.415	1.526
4019.7	1.170	1.218
6080.0	1.014	1.015
6239.0	.992	.993
6399.0	.994	.993
6621.0	1.001	.999
7465.0	1.001	.996
8465.0	.991	.987
9815.0	.970	.965
86300.0	1.009	1.012
111000.0	1.010	1.012
120200.0	.999	1.002

changes in the infrared indicate that the limb darkening residuals at 3204.68 and 4019.70 Å cannot be significantly improved without making the residuals in other regions of the spectrum substantially worse. There also seems to be a fundamental discrepancy between the limb darkening residuals at 3204.68 and 4019.70 Å.

The absolute intensities at 3204.7 and 4019.7 Å are higher in Model 2 than they are in Model 1. Experiments with a number of two-component solar models indicated that it is virtually impossible to make any significant improvements in the limb darkening residuals without increasing the disk-center absolute intensities at these two wavelengths. The anomalous limb darkening residuals and the high absolute intensities at these two wavelengths both suggest that line blanketing may play an important role below 4500 Å. Non-LTE effects can be excluded because the radiation at both of these wavelengths comes from the deepest layers of the photosphere. The experiments with Model 1 also showed that changes in the H^- absorption coefficient would have to be very large in order to significantly affect the absolute intensities at these wavelengths. Such changes were also found to be only marginally useful in improving the limb darkening residuals. One therefore requires an alternative opacity source that has the proper depth dependence at very short wavelengths. At 3204.7 Å such an opacity source would have to reduce the solar intensity by 29.3% at disk center

and by 39.2% at $\mu = 0.20$. At 4019.7 \AA this opacity source would only have to reduce the intensity by 14.5% at disk center and by 15.7% at $\mu = 0.20$. Line blanketing is the most likely source of this opacity.

Intensity fluctuations in the solar atmosphere have been studied by a number of investigators. Stratoscope I photographs of the solar granulation at approximately 5500 \AA have been examined by Schwarzschild (1959), Bahng and Schwarzschild (1961), Edmonds (1962), Namba and Diemel (1969), and Edmonds and Hinkle (1977). Schwarzschild (1959) and Bahng and Schwarzschild (1961) found rms intensity fluctuations of 7.2% near disk center in a one-dimensional study of several photographs that were taken in 1957 and 1959. Using a different calibration technique with some of the 1957 photographs, Edmonds (1962) concluded that there were rms intensity fluctuations of 13.9% near disk center. He also found that the rms intensity fluctuations reached a maximum of 20.5% at $\theta = 53^\circ$. Namba and Diemel (1969) later deduced that there were rms intensity fluctuations of 9.3% at disk center by studying two photographs that were taken in 1959. In a two-dimensional study of two other photographs from 1959, however, Edmonds and Hinkle (1977) concluded that there were rms intensity fluctuations as large as 14.7% near disk center. Recent ground-based observations also show a large scatter. Mehltretter (1971) found rms intensity fluctuations of 9.5% near disk center at 5520 \AA ; while Levy

(1971) found rms intensity fluctuations of 17.5% at 5300 Å. Deubner and Mattig (1975) determined that there were rms intensity fluctuations of 12.8% at 6070 Å. In a two-dimensional study of the center-to-limb variation of the granulation at 5520 Å, Keil (1977) measured rms intensity fluctuations of 13.2% at disk center.

Much of the scatter in the observational measures of the rms intensity fluctuations can be blamed on systematic errors in the instrumental corrections that were applied in the various investigations. Some scatter can also be attributed to transient local variations in the granulation pattern itself. All that one can really say for sure is that rms intensity fluctuations of $15 \pm 5\%$ are normally observed at 5500 Å. Model 2 predicts that one should observe rms intensity fluctuations of 17.3% near disk center at 5500 Å. This estimate assumes that the temperatures in the solar atmosphere vary in a coherent and sinusoidal fashion as a function of time along the line of sight and that the hot and cool components of Model 2 each accurately represent the temperatures over exactly half of the solar surface. If, on the other hand, one assumes that the temperatures along the line of sight vary linearly with time, then Model 2 predicts that one should observe rms intensity fluctuations of 25.4% near disk center. One must therefore know something about the evolutionary history of the granulation in order to derive an accurate estimate of

the rms intensity fluctuations from Model 2. On the average, however, the observational estimates of the rms intensity fluctuations agree fairly well with those that can be derived from Model 2.

Edmonds (1964, 1967, 1974) and Wilson (1963, 1964a, 1964b, 1969a, 1969b) developed a number of models that were based on the observations of the rms intensity fluctuations in the solar atmosphere. Unfortunately, much of their work was based on the observations of Edmonds (1962) which indicated that there was a maximum in the intensity fluctuations at $\theta = 53^\circ$. Recent studies by Turon and Lena (1973), Pravdjuk, Karpinsky, and Andreiko (1974), Albregtsen and Hansen (1977), and Keil (1977) do not confirm the existence of this maximum. Neither is there any evidence of such a maximum in the drift scans that were taken in this research. In fact, the bulk of the observational evidence now indicates that there is merely a general decline in the rms intensity fluctuations as one goes from disk center to the limb. Model 2 also predicts that the rms intensity fluctuations should decrease toward the limb.

Margrave and Swihart (1969) developed a two-component representation of the solar granulation that was based on a pair of non-grey model atmospheres. They adopted a relatively hot model for 40% of the solar surface and a much cooler model for the remaining 60% of the solar surface. Initially, they also assumed that each component was in

hydrostatic equilibrium and that each carried a constant fraction of the total flux at all depths in the atmosphere. In order to reproduce the limb darkening measures of Pierce and Waddell (1961), however, they found that it was necessary to allow the flux in the cool component to increase with height in the atmosphere. There was no direct theoretical computation of the energy exchange between the hot and cool components of the model.

Temperatures for the two-component model of Margrave and Swihart (1969) are shown with Model 2 in Figure 7.5. Temperatures in the cool component of their model are much lower than those in the cool component of Model 2. Temperature differences between the hot and cool components of their model at equal optical depths are also larger than temperature differences at equal geometric depths. Table 7.18 shows that just the opposite is true in Model 2. The splitting in their model is also fairly large in the upper levels of the photosphere. Most of these discrepancies can be traced back to their initial decision to simulate the temperature fluctuations in the solar atmosphere with a pair of standard non-gray models. The possibility of a substantial amount of energy exchange between the hot and cool columns of gas in the atmosphere makes this procedure somewhat questionable. Nonetheless, they still found that they could construct a relatively simple two-component model that would fit the observations

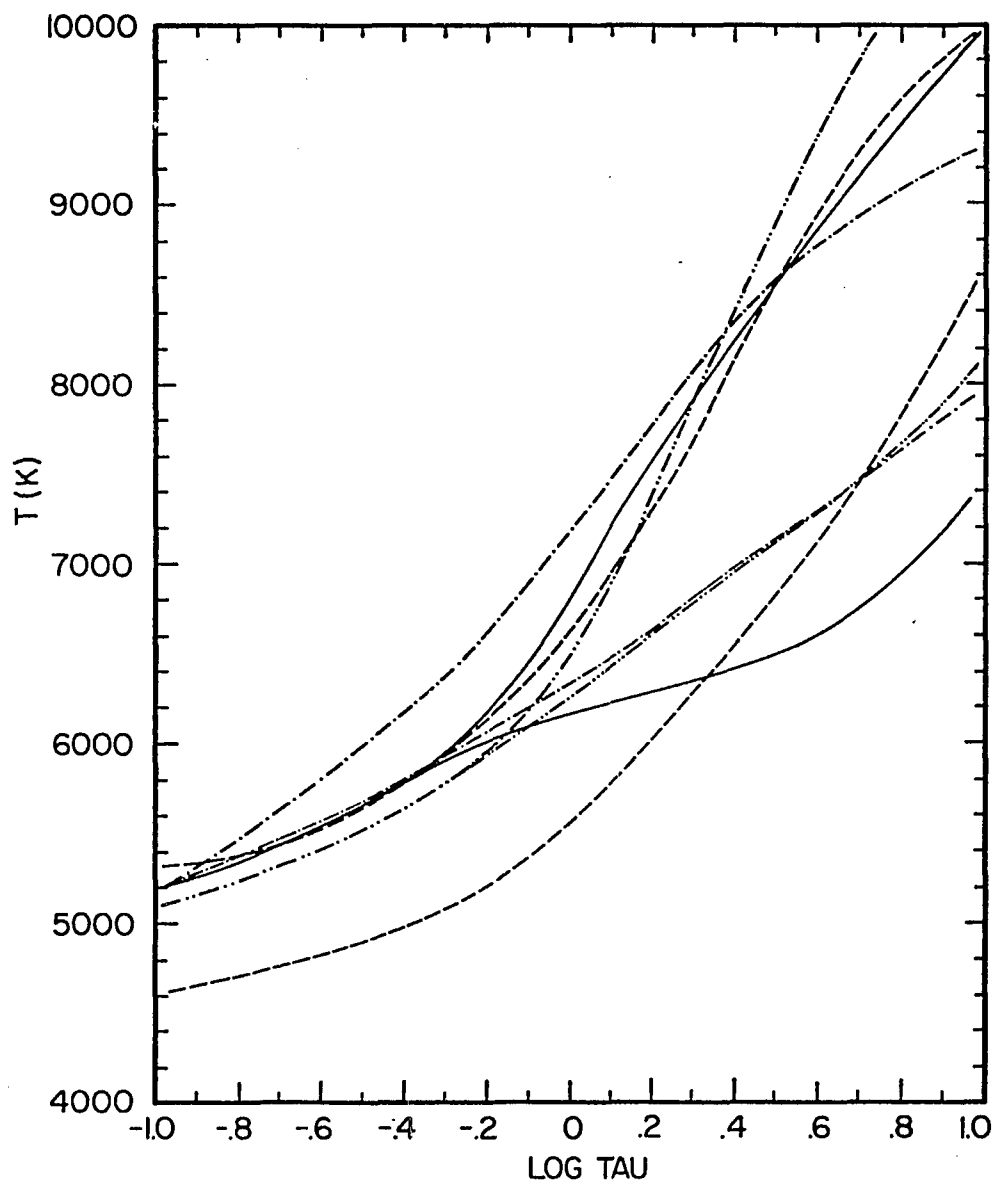


Figure 7.5. Solar models: (a) Model 2, —; (b) Margrave and Swihart (1969), ---; (c) Ulrich (1970), -.-; (d) Nordlund (1976), -.-.-.

Table 7.18. Normalized physical depths for the hot and cool components of Model 2.

Log $\tau_{5000} \text{ \AA}$	$\tau_{5000} \text{ \AA}$	Depth below $\tau = 10^{-4}$ (km)		$(\Delta z)_{\tau}$ (km)
		Hot component	Cool component	
-.4	.398	512	512	0
-.3	.501	525	525	0
-.2	.631	537	538	1
-.1	.794	547	551	4
.0	1.000	555	564	9
.1	1.256	561	577	16
.2	1.585	565	590	25
.3	1.995	569	603	34
.4	2.512	572	617	45
.5	3.162	576	631	55
.6	3.981	579	645	66
.7	5.012	581	657	76
.8	6.310	584	669	85
.9	7.943	587	680	93
1.0	10.000	589	689	100

better than any of the one-component models they had studied.

Ulrich (1970) developed a method for computing the physical conditions in a two-stream model of the solar atmosphere. Basically, he considered a steady-state atmosphere in which there were rising and falling columns of gas. Assumptions were also made about the horizontal scale and vertical velocity distribution of these columns of gas. The physical conditions in the rising and falling columns were then computed in an iterative fashion with the aid of an unperturbed semiempirical solar model. The results showed that one could expect temperature fluctuations of about the right order of magnitude in the visible layers of the atmosphere. Actual temperatures for a typical model are shown with Model 2 in Figure 7.5. The qualitative features of this model agree very well with those of Model 2.

Nordlund (1976) has recently presented a completely deductive technique for computing a two-component convective model of the solar atmosphere. One component of his model was assumed to be rising; the other falling. A diffusion-type differential equation for the convective velocity was then used with a series of energy conservation equations to compute the physical conditions in the two components. No detailed assumptions were made about the geometry, although the components were characterized by a typical linear size that was equivalent to the mixing length of the local mixing

length theory. In the standard model it was also assumed that each component represented half of the solar surface.

A composite of the solar models that were presented by Nordlund (1976) is shown with Model 2 in Figure 7.5. Each component of this model is plotted on its own optical depth scale. Because the details of Model 2 were worked out several months before the models of Ulrich (1970) and Nordlund (1976) were found in the literature, it was never constrained to fit any of their theoretical models. The basic agreement between Model 2 and the theoretical models is therefore quite remarkable and tends to confirm the two-component approach to modeling stellar atmospheres.

7.6 Conclusions

The qualitative agreement between Model 2 and the solar models of Ulrich (1970) and Nordlund (1976) suggests strongly that theoretical models of the solar atmosphere must ultimately take into account the effects of the solar granulation. The high precision of the current observations allows one to distinguish between models that differ by only a few tens of degrees in the visible layers of the atmosphere. The assumption of a single average temperature at each depth in the atmosphere obviously breaks down when one looks at the sun in such detail. One-component models will continue to be of use in stellar and solar studies that do not require the highest possible precision. A

significant improvement in accuracy, however, can be achieved by going to a two-component model.

Model 2 is the simplest and best model that could be found in this study, and it provides an excellent fit to the observations from at least 4500 to 100000 Å. Further improvements in the model will likely require a more complete investigation of non-LTE effects as well as improved theoretical estimates of the line blanketing in the ultraviolet. Absolute intensity measurements are also needed in the vicinity of the opacity minimum at 16400 Å. Since there is still a remote possibility that the absolute intensities in the visible are off by a few per cent, direct comparisons between the sun and a primary standard should be made at several wavelengths. Temperature fluctuations in the solar atmosphere should also be studied as a function of depth. High resolution observations at two or more wavelengths, in particular, should be used to study individual granules as they rise to the surface. Since there is a similarity between the cool component of Model 2 and a number of solar sunspot models, it is possible that sunspots are simply atmospheric regions in which the normal pattern of the convection has been seriously upset by magnetic fields. This possibility should also be investigated further.

Solar abundance should be recomputed with Model 2. Line profile studies of the solar temperature structure

should also be reevaluated. In many cases there may be a significant improvement in the agreement between theory and observation with the two-component model. Two-component models should also be considered for use in studying other stars with convectively unstable atmospheres.

/

REFERENCES

- Albregtsen, F., and T. L. Hansen. 1977, *Solar Phys.* 54, 31.
- Bahng, J., and M. Schwarzschild. 1961, *Astrophys. J.* 134, 337.
- Barber, C. R. 1969, *Nature* 222, 929.
- Bates, D. R. 1951, *J. Chem. Phys.* 19, 1122.
- Bates, D. R. 1952, *Monthly Notices Roy. Astron. Soc.* 112, 40.
- Bates, D. R., K. Ledsham, and A. L. Steward. 1953, *Phil. Trans. Roy. Soc. London A* 246, 215.
- Bell, K. L., and A. E. Kingston. 1967, *Proc. Phys. Soc.* 90, 895.
- Bell, K. L., A. E. Kingston, and W. A. McIlveen. 1975, *J. Phys. B: Atom. Molec. Phys.* 8, 358.
- Bohm, K. H. 1954, *Z. Astrophys.* 35, 179.
- Brandt, S. 1970, Statistical and Computational Methods in Data Analysis, North-Holland Publishing Company, Amsterdam, pp. 125-130.
- Burgess, A. 1958, *Monthly Notices Roy. Astron. Soc.* 118, 477.
- Carbon, D. F., and O. Gingerich. 1969, in O. Gingerich (ed.), Theory and Observations of Normal Stellar Atmospheres, MIT Press, Cambridge, p. 377.
- Carbon, D. F., O. Gingerich, and D. W. Latham. 1969, in S. Kumar (ed.), Low-Luminosity Stars, Gordon and Breach Science Publishers Inc., p. 435.
- Dalgarno, A. 1962, GCA Technical Report No. 62-28-A, Bedford, Mass.
- Dalgarno, A., and N. F. Lane. 1966, *Astrophys. J.* 145, 623.

- Dalgarno, A., and D. A. Williams. 1962, *Astrophys. J.* 136, 690.
- David, K.-H., and G. Elste. 1962, *Z. Astrophys.* 54, 12.
- Deubner, F. L., and N. Mattig. 1975, *Astron. Astrophys.* 45, 167.
- Doughty, N. A., and P. A. Fraser. 1966, *Monthly Notices Roy. Astron. Soc.* 132, 267.
- Doughty, N. A., P. A. Fraser, and R. P. McEachran. 1966, *Monthly Notices Roy. Astron. Soc.* 132, 255.
- Dunkelman, L., and R. Scolnik. 1959, *J. Opt. Soc. Am.* 49, 356.
- Edmonds, F. 1962, *Astrophys. J. Suppl. Ser.* 6, 357.
- Edmonds, F. 1964, *Astrophys. J.* 139, 1358.
- Edmonds, F. 1967, *Solar Phys.* 1, 5.
- Edmonds, F. 1974, *Solar Phys.* 38, 33.
- Edmonds, F., and K. H. Hinkle. 1977, *Solar Phys.* 51, 273.
- Garz, T., H. Holweger, M. Koch, and J. Richter. 1969, *Astron. Astrophys.* 2, 446.
- Geltman, S. 1962, *Astrophys. J.* 136, 935.
- Gingerich, O. 1964, in O. Gingerich (ed.), *Proceedings First Harvard-Smithsonian Conference on Stellar Atmospheres*, SAO Spec. Report No. 167, p. 17.
- Gingerich, O., R. W. Noyes, W. Kalkofen, and Y. Cuny. 1971, *Solar Phys.* 18, 347.
- Heintze, J. R. W., H. Hubenet, and C. de Jager. 1964, *Bull. Astron. Inst. Neth.* 17, 442.
- Houtgast, J. 1970, *Solar Phys.* 15, 273.
- John, T. L. 1968, *Monthly Notices Roy. Astron. Soc.* 138, 137.
- Karsas, W. J., and R. Latter. 1961, *Astrophys. J. Suppl. Ser.* 6, 16.

- Keil, S. L. 1977, Solar Phys. 53, 359.
- Kurucz, R. L. 1970, Atlas: A Computer Program for Calculating Model Stellar Atmospheres, SAO Spec. Report No. 309.
- Labs, D., and H. Neckel. 1962, Z. Astrophys. 55, 269.
- Labs, D., and H. Neckel. 1963, Z. Astrophys. 57, 283.
- Labs, D., and H. Neckel. 1967, Z. Astrophys. 65, 133.
- Labs, D., and H. Neckel. 1968, Z. Astrophys. 69, 1.
- Labs, D., and H. Neckel. 1970, Solar Phys. 15, 79.
- Lambert, D. L. 1968, Monthly Notices Roy. Astron. Soc. 138, 143.
- Lambert, D. L., and B. Warner. 1968, Monthly Notices Roy. Astron. Soc. 138, 181.
- Levy, M. 1971, Astron. Astrophys. 14, 15.
- Margrave, T. E., and T. L. Swihart. 1969, Solar Phys. 6, 12.
- Mehltretter, J. P. 1960, Z. Astrophys. 51, 32.
- Mehltretter, J. P. 1971, Solar Phys. 19, 32.
- Menzel, D. H., and C. L. Pekeris. 1935, Monthly Notices Roy. Astron. Soc. 96, 77.
- Namba, O., and W. H. Diemel. 1969, Solar Phys. 7, 167.
- Nordlund, A. 1976, Astron. Astrophys. 50, 23.
- Peach, G. 1967, Mem. Roy. Astron. Soc. 71, 29.
- Peach, G. 1970, Mem. Roy. Astron. Soc. 73, 1.
- Pierce, A. K. 1954, Astrophys. J. 120, 221.
- Pierce, A. K., and C. D. Slaughter. 1977, Solar Phys. 51, 25.
- Pierce, A. K., and J. H. Waddell. 1961, Mem. Roy. Astron. Soc. 68, 89.

- Pravdjuk, L. M., V. N. Karpinsky, and A. V. Andreiko.
1974, Solnechnye Dannyy No. 2, 70.
- Saiedy, F. 1960, Monthly Notices Roy. Astron. Soc. 121,
483.
- Saiedy, F., and R. M. Goody. 1959, Monthly Notices Roy.
Astron. Soc. 119, 213.
- Schwarzschild, M. 1959, Astrophys. J. 130, 345.
- Somerville, W. B. 1964, Astrophys. J. 139, 192.
- Stilly, J. L., and J. Callaway. 1970, Astrophys. J. 160,
245.
- Stimson, H. F. 1949, Journal of Research of the National
Bureau of Standards, 42, 209.
- Turon, J. P., and P. Lena. 1973, Solar Phys. 30, 3.
- Ulrich, R. 1970, Astrophys. Space Sci. 9, 80.
- Vernazza, J. E., E. H. Avrett, and R. Loeser. 1976,
Astrophys. J. Suppl. Ser. 30, 1.
- Voight, H. H. 1956, Z. Astrophys. 40, 157.
- Wilson, P. R. 1963, Astrophys. J. 137, 606.
- Wilson, P. R. 1964a, Astrophys. J. 139, 929.
- Wilson, P. R. 1964b, Astrophys. J. 140, 1148.
- Wilson, P. R. 1969a, Solar Phys. 6, 364.
- Wilson, P. R. 1969b, Solar Phys, 9, 303.
- Wittman, A. 1977, Astron. Astrophys. 61, 225.